CONTROLLING SPINS AND VALLEYS THROUGH BROKEN CRYSTAL SYMMETRIES IN LAYERED TRANSITION METAL DICHALCOGENIDES

A Dissertation

Presented to the Faculty of the Graduate School

of Cornell University

in Partial Fulfillment of the Requirements for the Degree of

Doctor of Philosophy

by

David MacNeill

January 2017

CONTROLLING SPINS AND VALLEYS THROUGH BROKEN CRYSTAL SYMMETRIES IN LAYERED TRANSITION METAL DICHALCOGENIDES

David MacNeill, Ph.D.

Cornell University 2017

In this dissertation, I will summarize two very different experiments involving layered transition metal dichalcogenides, along with the technical information required to understand and reproduce them.

The first experiment concerns the optical properties of a single molecular layer of $MoSe_2$. Electrons in $MoSe_2$ have a hidden internal state, called the "valley" degree of freedom, related to the existence of multiple degenerate low-energy states. In other semiconductors with valley degeneracy, e.g. silicon and germanium, the valley state of electrons is hard to probe, and most experiments reveal only valley-averaged quantities. However, the broken inversion symmetry of a $MoSe_2$ monolayer allows for a curious property – the valley state of electrons can be read-out and manipulated with circularly polarized light. In our experiments, we used this property to measure how the magnetic moment of the exciton (a bound electron-hole pair) depends on its valley state. We measured polarized-resolved luminescence spectra in a magnetic field, and looked at the energy difference between excitons in the different valleys. Our results show that magnetic field can be used to break valley degeneracy in monolayer $MoSe_2$, and also give important input (the exciton magnetic moment) for band structure models.

The second experiment concerns spin transport across, or perhaps at, the interface between the transition metal dichalcogenide WTe_2 and a ferromagnet,

permalloy. By flowing current in the plane of a WTe_2/permalloy stack, we are able to inject spins into the permalloy and generate a torque on its magnetic moment. This phenomena – known a spin-orbit torque – has been well studied in other heavy-metal/ferromagnet bilayers. The new idea of our work is to use a low-symmetry crystal as the spin-generation layer. Depositing permalloy onto WTe_2 breaks the combined rotation-translation symmetry of the WTe_2 crystal, resulting in a remarkably low symmetry stack. This allows for new torques forbidden by symmetry in conventional devices, corresponding to injection of spins with their moment out of the sample plane. Out-of-plane spin injection is ideal for the manipulation of technologically-relevant magnets with perpendicular anisotropy, so our results open new possibilities for non-volatile magnetic memory technologies.

Although these two experiments concern separate realms of physics – optics and spin transport – they are connected by the theme of broken crystal symmetries. In both cases, the interplay of reduced crystal symmetry and spin-orbit coupling leads to additional control over internal electron states. Another theme is the utility of mechanical exfoliation to prepare high-quality crystalline samples, especially of low-symmetry single-crystal films and containing refractory elements.

BIOGRAPHICAL SKETCH

David MacNeill was born Vancouver, Canada, in 1988. After high school, he studied mathematics and physics at his hometown school, the University of British Columbia, graduating with a BSc. in 2010. For graduate school he decided to focus on physics, moving to Ithaca to attend Cornell University. Despite having, "never touched a soldering iron," he joined the group of Daniel C. Ralph to do some experiments. Many soldering iron burns later, he will graduate with a doctorate in experimental physics in 2017. Afterwards, he will work as a postdoctoral researcher in the group of Pablo Jarillo-Herrero at MIT.

To my parents,

Debra Windjack and,

in memory,

Paul MacNeill.

ACKNOWLEDGEMENTS

First, my advisor, Dan Ralph. The kindness and humor you bring to the lab are inspiring. I am thankful for the freedom you gave me to pursue my own experiments, while providing guidance towards more interesting directions.

I am also very thankful to Jiwoong Park. Without your collaboration I wouldn't have gotten far. Your encouragement and interest in my work was always a big motivator.

To the members of my committee, Frank Wise and Eun-Ah Kim, many thanks for reviewing this dissertation. Frank, your encouragement and discussions (and quantum dots) helped me through the early days of graduate school.

My deepest acknowledgements go to two Kavli postdoctoral scholars, Kin Fai Mak and Marcos Guimãraes. I have learned so much from both of you. Fai, thanks for introducing me to layered transition-metal dichalcogenides. I owe the success of my first project to your deep knowledge of these materials. I hope you stay on top of the field for years to come. Marcos, you have been a great friend and mentor, in and out of lab. We came up with many big ideas together ... too bad most of them failed! I wish you great success in your next endeavors.

To Lei Wang, thank you for sharing your beautiful scientific philosophies and ideas.

To Nate Ellis, your machining advice and training were critical for building my first experiments, every step of the way.

To Eric Smith, I couldn't have built my cryostat without your vast knowledge of cryogenic engineering. Bringing design problems to your attention tends to get them solved fast ...

Special thanks to Yongxi Ou and Minh-Hai Ngyuen, for keeping the

Buhrman group ion mill and sputter system running.

To the students and alumni of the Ralph group: Colin Heikes, Alex Mellnik, Jonathan Gibbons, Eugenia Tam, Chen Wang, Ted Gudmundsen, Colin Jermain, Lin Xue, Wan Li, Neal Reynolds, Gregory Stiehl, Jennifer Grab, Peter Mintun, Alison Rugar and Zachary Anderson. Your friendly (and eccentric) attitudes make me excited to get to work. Long live the physics unicorn!

Colin, thanks for mentoring me in the group and putting up with my inexperience. Neal, I'm not convinced the group can run without you at this point. Thanks for fixing everything and defeating interlocks. And keeping us safe. Jon, we have had our disagreements ... but you always have something interesting on your mind! Greg, I appreciate your eye for important problems and deep knowledge of spintronics. I'm glad we actually starting working together after passing in the hallway for a few years. Thanks for lending a critical ear to my ideas, and helping me find a job. Jennifer, you have been an amazing friend all these years. Thanks for lifting my spirits after many failed experiments. Alison, your enthusiasm and positive attitude brighten up my life. Thanks for keeping my cynicism in check.

To my friends: Bob de Alba, Nathan Mirman, and Veronica Pillar. From driving lessons to late night philosophical discussions, you guys have always been there for me. Graduate school wouldn't be the same without you, and I hope we can stay in touch. Best of luck in your next adventures.

TABLE OF CONTENTS

LIST OF TABLES

LIST OF FIGURES

CHAPTER 1

INTRODUCTION

For decades, physicists have been fascinated by the behavior of electrons confined to two dimensions. Since electrons are ordinarily free to move in the three dimensions of empty space, various schemes are employed to restrict their motion. Some of these are shown in Fig. 1.1: there we see the use of a) electric fields to push electrons up against a surface, and b) electrons moving in a crystal structure consisting of weakly coupled planes, without chemical bonding between each layer.

In the case of Fig. 1.1b, the electrons may be considered as quasi-two-dimensional, i.e. able to move in three-dimensions, but moving much more quickly within the layers than between them. In fact, the electronic properties of such a crystal can often be understood in terms of the properties of an isolated layer, with small corrections. Such two-dimensional behavior has lead to longstanding interest (since at least the 1950s) in the properties of layered materials, such as graphite and transition-metal dichalcogenides. Prior to about 2000, attempts to actually study the physical properties of isolated layers were

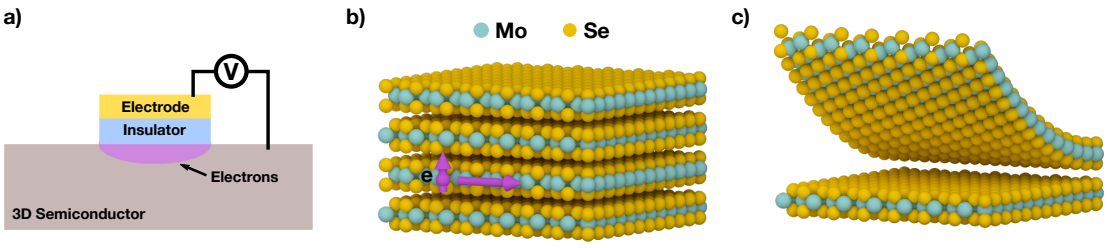

Figure 1.1: **a)** Electrons in a semiconductor are confined to two-dimensions by an electric field. **b)** Electrons are confined to move in planes by a layered crystal structure (here the transition-metal dichalcogenide $MoSe_2$). **c)** Single layers can be peeled from the crystal shown in **b)**.

inconclusive. While there were some sightings of crystals only a few molecular layers thick [1, 2], researchers stopped short of systematically measuring their electrical and optical properties. A big factor hindering progress was the lack of reliable synthesis methods. Typically thin films of layered crystals were prepared either by chemical exfoliation methods – creating films with many impurities – or later as sub-micrometer crystals in ultra-high-vacuum [3].

The situation changed in 2004 with the remarkable discoveries of Profs. Geim and Novoselev [4]. Eschewing chemical techniques, they found that single layers of graphene could be peeled from bulk graphite crystals using scotch tape. This process is called mechanical exfoliation. Soon after, they isolated other monolayer crystals [5], including three-atom-thick layers of transition-metal dichalcogenides (see Fig. 1.1c). Such isolated layers are wonderful things. Despite being atomically thin, they can be 10's of microns wide, and are therefore easily visible under a microscope, and can be moved around with e.g. tweezers, probes, or stamps. Although these are fun materials to play with, we have to ask: what are they good for?

Many researchers have different answers to this question, which, along with inexpensive tape-based preparation techniques, has lead to explosive growth of the field over the last decade. My answer, from a narrow perspective, is that layered materials allow for quick exploration of two-dimensional electrons in different crystalline environments, with crystalline quality determined primarily by the bulk crystal synthesis. Layered crystals tend to have low-symmetry structures and often contain heavy or unusual elements, making them complementary to two-dimensional materials prepared by other means. Their flexibility and substrate independence also allow for device geometries impossible

with conventional 3D crystals. Recent studies identify over 800 stable layered compounds known to science [6,7]. Furthermore, layers from different crystals can be stacked together, exponentially increasing the possibilities. Because of this diversity, many surprises likely await in the world of layered crystals.

In this dissertation, I present two research projects involving layered transition-metal dichalcogenides. The first concerns optical measurements of monolayer $MoSe_2$ in a strong magnetic field, providing insight into the electronic structure not accessible through other methods. The second study concerns heterostructures of an amorphous ferromagnet with thin films of WTe_2. There, I will discuss how the unusual crystal structure of WTe_2 leads to new methods for electrically controlling magnetism. Despite their differences, these two studies are connected by a common theme of using low-symmetry exfoliated crystals to realize new physical phenomena.

In both cases, we take a bulk crystal, and reduce its symmetries by eliminating symmetry operations which couple adjacent layers. For $MoSe_2$, this is done by removing all the layers except one! Thus, the inversion symmetry of the bulk crystal is broken, opening the way for additional control over the electron's degrees of freedom. In monolayer $MoSe_2$, it is possible to control a vector (the electron's "valley," degree of freedom, related to its momentum) through manipulation of a pseudovector (its angular momentum). Coupling of this type is forbidden in a centrosymmetric crystal, due to the different parities of vectors and pseudovectors. Since the angular momentum is much easier to control e.g. by magnetic fields, this vector-pseudovector coupling provides a new way to control the valley degree of freedom.

Similar symmetry constraints are at play in the phenomena of "spin-orbit

torques," where flowing a current (vector) in a heavy metal can generate torques (pseudovector) in an adjacent magnetic material. In most cases, the requisite inversion symmetry breaking is provided by the heavy-metal-to-magnet interface. Here we go further, breaking *rotational* symmetry. To do this, we use a crystal, WTe_2, that has no pure rotation symmetry, but only a combined rotation-translation symmetry. Depositing a magnet on top conveniently breaks the rotation-translation symmetry, and provides a readout of any spin-orbit torques. As a result, we are able to observe spin-orbit torques not possible in higher-symmetry crystals, with potential relevance for magnetic memory technologies. Thin film monocrystals of $MoSe_2$ and WTe_2 are difficult to grow (especially WTe_2) so our studies illustrate the utility of mechanical exfoliation in exploring low-symmetry crystalline materials.

1.1 Diversity of transition-metal dichalcogenides

Despite the wide variety of layered crystals, I will only discuss here a subset called the transition metal dichalcogenides (TMDs). These are crystals of the form MX_2 where M is a transition metal and X is a chalcogen. The basic properties of bulk TMDs were understood by the 1970s, as summarized in the review by J. A. Wilson and A. D. Yoffe [8]. The layered TMDs occur in two structural motifs, depending on the local structure of the transition-metal to chalcogen bonding. In the H or trigonal phase, the transition-metal sits in the center of a trigonal prism of chalcogen atoms. In the T or octahedral phase, the transition metal is surrounded by an octahedron of chalcogen atoms. These units are then tiled throughout the plane to create a layer, and the layers are stacked to create the entire crystal (Fig. 1.2).

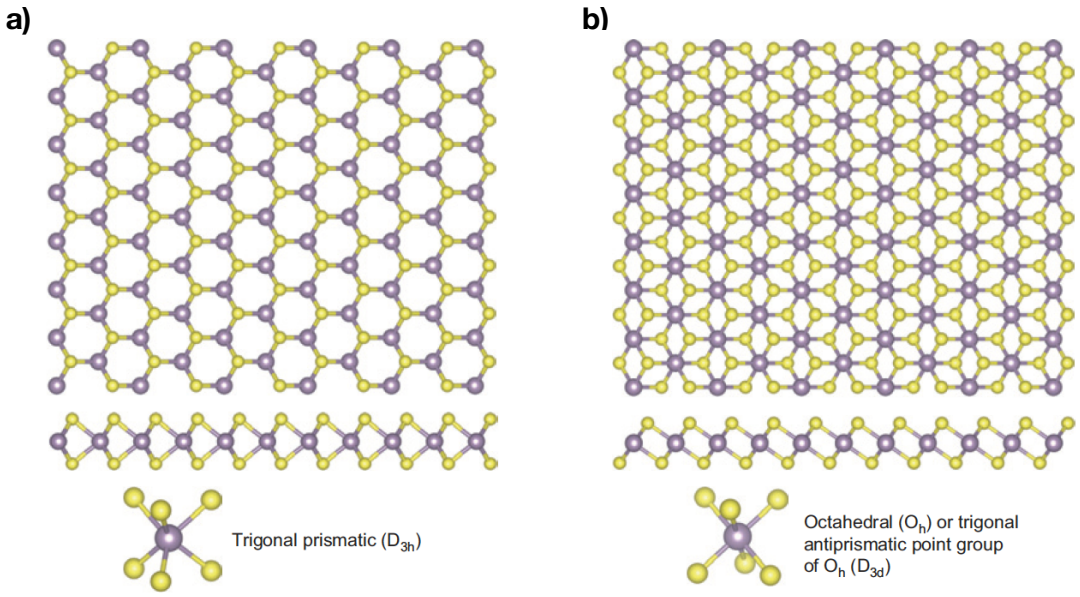

Figure 1.2: Typical crystal structures of monolayer TMDs, taken from Ref. [9]. WS_2, WSe_2, MoS_2 and $MoSe_2$ naturally form in the trigonal prismatic structure shown in panel **a)**. Bilayers are inversion symmetric and typically take the "2H" structure where the two monolayers are Bernal stacked. **b)** Octahedral structure of MX_2 TMDs. WTe_2, for example, forms in a distorted version of this structure.

By varying the transition-metal and chalcogen in the above formula, we can realize an great variety of electronic properties. Bulk TMDs can be metals, semi-metals, or semiconductors. There is also evidence that certain semimetallic TMDs realize topological band structures [10–13] . Below room temperature, many TMD compounds undergo electronic and structural transitions, with charge density waves being particularly common. An overview of these properties is presented in Table 1.1, reproduced from Ref. [8] with my own additions. Clearly, a vast amount of TMD-related information had already been collected four decades ago. However, interest in the materials surged in 2010, with the discovery that MoS_2 monolayers had optical properties very different from bulk crystals [14, 15]. Researchers soon expanded their studies to cover isoelectronic materials – WS_2, WSe_2, $MoSe_2$, $MoTe_2$ – finding them to differ in

M	$-S_2$		$-Se_2$		$-Te_2$		Notes
Ti	T	0.2	T	0-0.2	T	0	$TiSe_2$: CDW [16], gap [17]
Zr	T	1.7	T	1.1	T	0	
Hf	T	2-3	T	1.1	T	0	$HfTe_2$: semi-metal [18]
V	T	0	T	0	T^{12}	0	VSe_2: CDW [19]
Nb	H	0	H	0	T^{12}	0	All: SC, $NbSe_2$: CDW [20]
Ta	H(T)	0(0)	H(T^2)	0(0)	T^{12}	0	All: CDW, 2H-TaX_2: SC, 1T-TaX_2: RT CDW, $\rho \sim 10^{-3}$ Ω·cm [21,22]
Mo	H	1.2	H	1.1	H(T^{11})	1.2 (0)	$MoTe_2$: $T^{11} \rightarrow T^{31}$ at 250 K [23]
W	H	1.3	H	1.3	T^{31}	0	
Tc	T^2	1	T^2	0.9	–	–	
Re	T^2	1.3	T^2	1.2	–	–	
Ir	–	–	–	–	T	0	$T \rightarrow T^2$ below 270 K [24,25].
Ni	–	–	–	–	T	0	$\rho \sim 10^{-5}$ Ω·cm [8]
Pd	PdS_2	0.7-0.8	PdS_2	0.4	T	0	$PdTe_2$: SC
Pt	T	1-1.4	T	0-0.1	T	0	$PtTe_2$: $\rho \sim 10^{-5}$ Ω·cm [8]

Table 1.1: Crystal structures and energy gaps (in eV) for *bulk* TMDs at room temperature, with misc. properties in the "Notes" column. Only layered compounds that have been synthesized are included. H indicates the trigonal phase, and T indicates the octahedral phase. $T^{\#}$ indicates a distorted T phase with space group #. A value of "0" in the band-gap column indicates a metal or semi-metal. Unless otherwise specified, data were obtained from the Springer Materials database [26].

subtle but important ways from MoS_2. One of these compounds ($MoSe_2$) will be a major subject of my dissertation, and I will review some relevant properties below.

1.2 Some properties of monolayer $MoSe_2$

1.2.1 Electronic structure

Fig. 1.3a shows a monolayer $MoSe_2$ crystal with the trigonal structure. In projection, it is a honeycomb lattice with inequivalent *A* and *B* sites. One might guess that the resulting electronic structure would be similar to that of graphene with broken sub-lattice symmetry. This turns out to be qualitatively correct, as

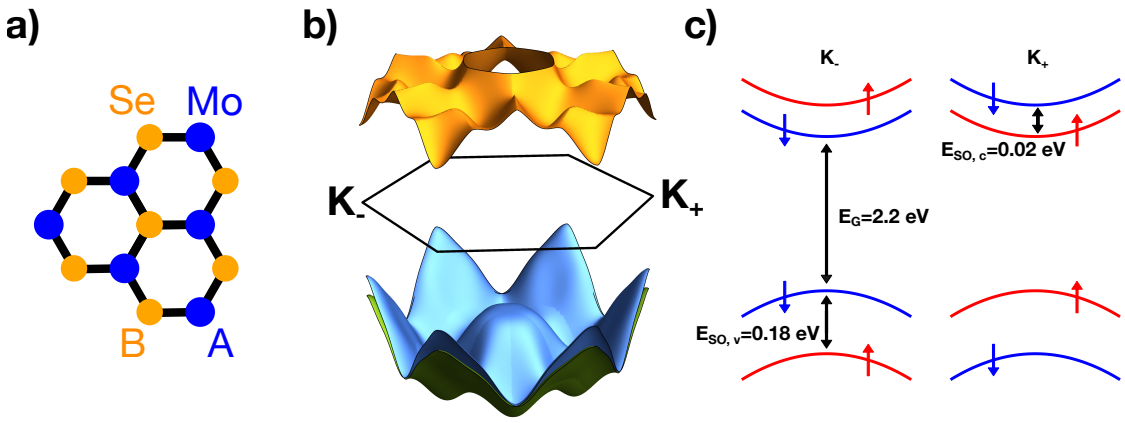

Figure 1.3: **a)** Top-down crystal structure of $MoSe_2$ **b)** Bandstructure of $MoSe_2$ calculated in a three-orbital tight-binding model (Ref. [31]), showing valleys in the corners of the hexagonal Brillouin zone. The spin-orbit splitting of the conduction band is dominated by orbitals outside the three-orbital set, and is not accurately captured by the model. **c)** Schematic bandstructure of $MoSe_2$ around the $K_\pm$ points, showing best-estimates for various energy scales (at 4.2 K). Colored arrows indicate the direction of the electron's spin angular momentum within a given band. Not to scale.

seen in Figs. 1.3b and 1.3c showing the schematic low-energy band structure of monolayer $MoSe_2$. Similar to gapped graphene, there are direct band gaps at the K_+ and $K_- = -K_+$ points of the hexagonal Brillouin Zone [27]. For graphene on hexagonal boron nitride, these gaps are around 20-50 meV [28], but for $MoSe_2$ they are about 2 eV [29]. The presence of multiple energy minima leads to an extra "valley" degree of freedom for low energy electrons corresponding to which of the local minima (K_+ or K_-) they are in. Also similar to gapped graphene, the electrons and holes are expected to have similar effective masses $|m_{c,v}| \approx 0.6m_0$, where m_0 is the free electron mass [30].

The chemical origin of these bands is very different from graphene: the conduction band arises primarily from hybridization of molybdenum d_{z^2} orbitals while the $K_\pm$ valence band arises primarily from hybridization of $d_{x^2-y^2} \pm id_{xy}$ molybdenum orbitals [27, 32]. The presence of heavy elements leads to strong

spin-orbit coupling. Because inversion symmetry is broken in the monolayer $MoSe_2$ crystal structure, the spin-orbit coupling creates strong effective magnetic fields in momentum space, polarizing spins in each valley along a preferred direction [27]. The direction of the spin-orbit fields is a consequence of symmetry: they must point out-of-plane, since this is the only direction (for a pseudovector) that is invariant under the horizontal mirror plane of $MoSe_2$. The spin orbit field leads to an energy difference of about 180 meV between opposite spins in the valence band [33]. Since $L_z = 0$ for the conduction band, the spin-orbit splitting is much smaller there. Ultimately, a small admixture of the chalcogen p-orbitals and Mo d_{yz}/d_{xz} orbitals leads to a spin splitting of about 20 meV [32]. Because the crystal does not break time reversal symmetry, there can be no net spin polarization, and the spin-orbit fields must change sign between the two valleys. The pattern of valley-dependent spin-orbit fields is shown in Fig. 1.3c.

1.2.2 Valley-dependent optical selection rules

When a $MoSe_2$ crystal is irradiated with light near the band-gap energy, electrons in the valence band can absorb a photon and enter the conduction band. However, electrons in the K_+ valley can only absorb photons with spin "up" (out-of-plane), whereas electrons in the K_- valley respond to the opposite circular polarization (as shown in Fig. 1.4). This selection rule is a consequence of the symmetries of the band-edge Bloch states, which in turn arise from the crystal symmetries [27, 34]. In particular, the Bloch states are eigenstates of the three-fold rotation symmetry of the crystal, leading to a discrete version of angular momentum conservation [35]. Under a 120° rotation, the conduction band state

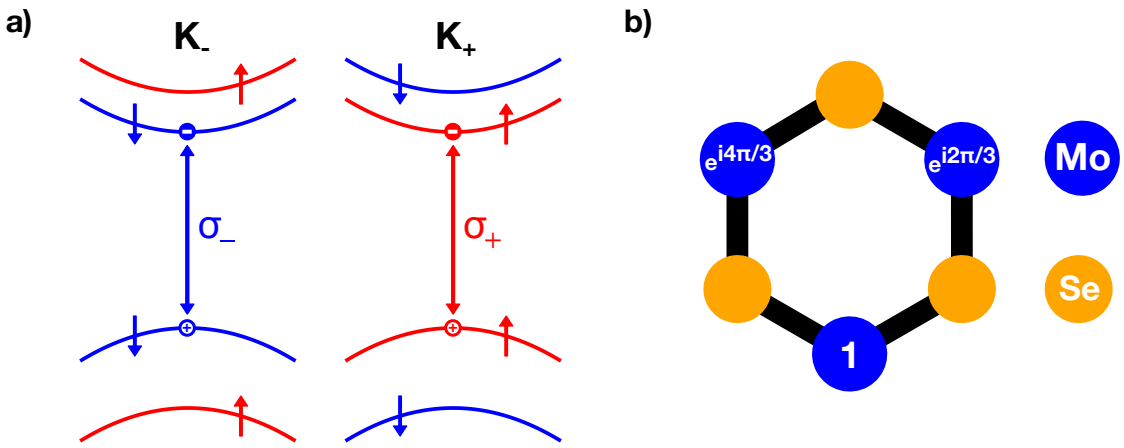

Figure 1.4: **a)** The schematic band structure of $MoSe_2$ showing allowed optical transitions (double-ended arrows). In valley $K_\pm$, valence electrons can absorb a $\sigma_\pm$ and transition to the conduction band. **b)** $e^{i\mathbf{K}_+\cdot\mathbf{r}}$ evaluated on the molybdenum sites around a $MoSe_2$ unit cell.

$|c, K_\pm\rangle$ is mapped to $e^{-i\frac{2\pi}{3}}|c, K_\pm\rangle$. On the other hand, the valence band states are completely invariant under 120° rotations ($|v, K_\pm\rangle \rightarrow |v, K_\pm\rangle$). On can therefore think of the conduction band states at the $K_\pm$ points as having angular momentum quantum number $m = \pm 1$, and the valence band states as having $m = 0$. The same result can be obtained by calculating the probability for an optical transition assuming left or right circularly polarized illumination:

$$P_{\text{left}}(\mathbf{k}) \propto \langle c, \mathbf{k}|(p_x + ip_y)|v, \mathbf{k}\rangle \tag{1.1}$$

$$P_{\text{right}}(\mathbf{k}) \propto \langle c, \mathbf{k}|(p_x - ip_y)|v, \mathbf{k}\rangle. \tag{1.2}$$

The symmetry properties of the $K_\pm$ states can be used to determine when the above matrix elements vanish.

It is somewhat surprising that the valence band Bloch states are rotationally invariant, given that they are built from $d_{x^2-y^2} \pm id_{xy}$ orbitals which are $m = \pm 2$ eigenstates. An intuitive explanation for this is shown in Fig. 1.4b, where I plot $e^{i\mathbf{K}_+\cdot\mathbf{r}}$ evaluated at the molybdenum atoms of the $MoSe_2$ unit cell. When the

unit cell is rotated by 120° about its center, the phase is rolled back by $e^{-i\frac{2\pi}{3}}$. In the valence band, an additional phase shift of $e^{-i\frac{4\pi}{3}}$ come from rotation of the d-orbitals (which have azimuthal dependence $e^{i2\phi}$), so that there is no overall phase-shift. On the other hand, in the conduction band the relevant d_{z^2} orbitals are rotationally invariant, so the only phase shift comes from the rotation of $e^{i\mathbf{K}_+\cdot\mathbf{r}}$.

It's important to note that these arguments to do not allow one to calculate the actual angular momentum carried by electrons in the conduction or valence band, only to derive the optical selection rules. For example, our magneto-optical experiments suggest the valence band electrons carry orbital angular momentum on the order of a few $\hbar$, contrary to $m = 0$. I will tackle the thorny issue of calculating this angular momentum in Section 3.7, giving its precise relationship to matrix elements in Eqs. 1.1 and 1.2.

1.2.3 Excitons and trions

When an electron is excited from the valence to conduction band, it leaves a positively charged hole in the valence band. These two particles interact through electrostatic forces, and can form a stable bound state called an exciton [36]. Exciton bound states greatly modify the optical properties of the material. For example, creation of an exciton in monolayer $MoSe_2$ requires much less energy (about 1.65 eV [37]) than the creation of a unbound electron-hole pair (about 2.2 eV [29]). Therefore, excitons lead to increased photon absorption below the electronic band gap. The energy threshold for photon absorption is called the optical band gap, and is given by the electronic band gap minus the exciton

binding energy.

In the simplest model (due to Wannier [38] and extended by Eliot [39]), the exciton binding energy is calculated using the two-body Schrodinger equation for the electron and hole (with their band masses) interacting through a potential $V_{\mathrm{e-h}}$. The electron-hole Coloumb interaction is screened by the polarizability of the $MoSe_2$, so that it deviates from a simple $1/r$ form. For two point charges in the plane of a very thin polarizable sheet, the potential is [40, 41]:

$$V_{\mathrm{e-h}}(r) = -\frac{e^2}{8\epsilon_0 r_0}\left\{H_0\left(\frac{r}{r_0}\right) - Y_0\left(\frac{r}{r_0}\right)\right\} \tag{1.3}$$

where H_0 and Y_0 are the zeroth-order Struve and Bessel functions, r is the electron-hole separation, and $r_0 = 2\pi\chi_{2\mathrm{D}}$ is a length scale related to the 2D susceptibility of the $MoSe_2$. In Ref. [40] the authors calculate $r_0 \approx 5.2$ nm from first-principles calculations. Using this value, I find an exciton binding energy of 0.49 eV with an exciton Bohr radius of $\langle r \rangle \approx 0.9$ nm. This binding energy is similar to values measured in experiment (0.55 eV, for $MoSe_2$ on bilayer graphene) and calculated from first-principles methods (0.65 eV, for free-standing $MoSe_2$) [29]. Furthermore, reflectivity measurements in Ref. [42] reveal a spectrum of exciton states matching Eq. 1.3, suggesting that the Wannier model captures the basic physics of excitons in monolayer transition metal dichalcogenides. Despite the semi-quantitative agreement, such calculations exclude important factors, such as mixing from other bands and the non-parabolic dispersion as one moves away from the K points. These are included in the first-principles Wannier model of Ref. [29], and are important in quantitatively determining both the ground state energy and level ordering of excited states.

When free carriers are added to the monolayer, there are two main complications. Excitons can bind with free electrons to form a three-body bound

state, called a trion or charged exciton. Furthermore, as the density of free electrons is increased, Pauli-blocking and screening modify the properties of both excitonic species. It is not hard to calculate the properties of an isolated trion, at least within the Wannier model. Using the potential in Eq. 1.3, the authors of Ref. [40] calculate a trion binding energy of 30 meV for monolayer $MoSe_2$, which is consistent with experimental values for lightly doped $MoSe_2$ (see Section 3.2). Empirically, as the level of doping is increased the exciton resonance (in luminescence and absorption) is found to disappear rapidly, while the trion resonance persists to well over 10^{12} carriers per cm^2. As of this writing, experimentalists and theorists have only just started to understand the excitonic structure of monolayer TMDs in the high carrier density regime, which appears to be dominated by many-body effects beyond the simple pictures discussed here [43, 44].

CHAPTER 2

CRYOGENIC CONFOCAL MICROSCOPY

In this dissertation, I will study exciton states using photoluminescence spectroscopy. In this technique, the sample is irradiated with photons above the optical gap, and the emission is monitored at lower energies. In $MoSe_2$, absorption of 1.9 eV photons can create excitons with highly excited orbital and spin states. Such excitons will relax to near the excitonic ground state within their short lifetime. All excitons eventually decay, and a small fraction dissipate their energy by re-emitting a photon. Therefore, we can measure the energies of low-lying exciton states by analyzing the spectrum of light emitted from the sample at energies slightly below the illumination energy.

It is also desirable to cool the sample to low temperatures, since thermal motion broadens the exciton states. In most two-dimensional electron systems, the exciton binding energy (a few meV) is well below the thermal energy at room temperature (26 meV) so that excitons will be unstable to thermal fluctuations! This isn't a problem in transition metal dichalcogenides, due to the high exciton binding energies; but we still want low temperatures, to help uncover the fine-structure and to observe three-body exciton states.

Low-temperature optical spectroscopy requires some method of cooling the sample while also maintaining a line-of-sight to the outside world. This can be problematic, since thermal radiation can traverse the same path and heat up the sample. The conventional solution is to accept a small amount of heating as inevitable, and to open a gap in the radiation shielding of the cryostat so that the sample can be seen through a window. We decided to experiment with a different method, which uses an optical fiber to couple light into the cryogenic

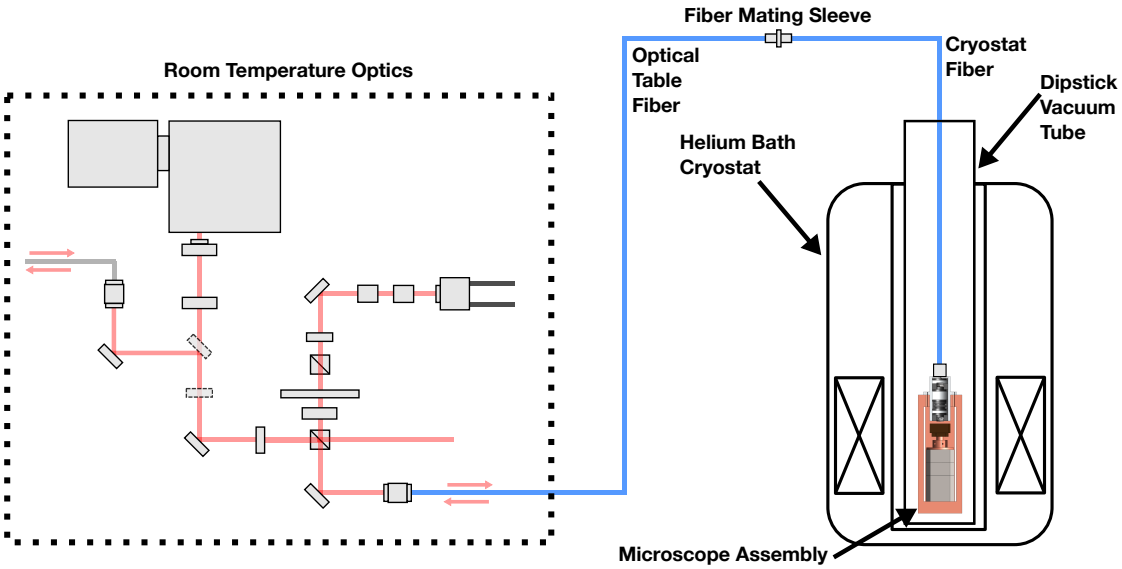

Figure 2.1: Overall layout of our fiber-coupled optical cryostat, showing the various subsystems discussed in this chapter.

space. The advantages of this method are that it minimizes thermal radiation, can be integrated with existing cryostats, and can be generalized to extreme conditions such as sub-Kelvin temperatures and high magnetic fields. It does come with two disadvantages, which are the requirement of placing focussing optics in the cryogenic space and the limitations of having long optical fibers in the optical path.

In this chapter, I will describe the design and validation of a fiber-coupled "dipstick" microscope for use with a liquid-helium-cooled superconducting magnet. This is essentially a rudimentary confocal microscope, which is built onto the end of a long vacuum tube. Light is coupled in and out of the microscope using a polarization-maintaining fiber, and the tube is lowered into the bore a helium bath cryostat for low-temperature measurements. The complete system consists of the cryostat and cryogenic microscope, and the room-temperature optics used couple laser light into the fridge and analyze the light

emitted by the sample. In the following sections, I will break down the operation and design of our microscope into subsystems, as organized in Fig. 2.1.

2.1 Optics for fiber coupling and optical spectroscopy

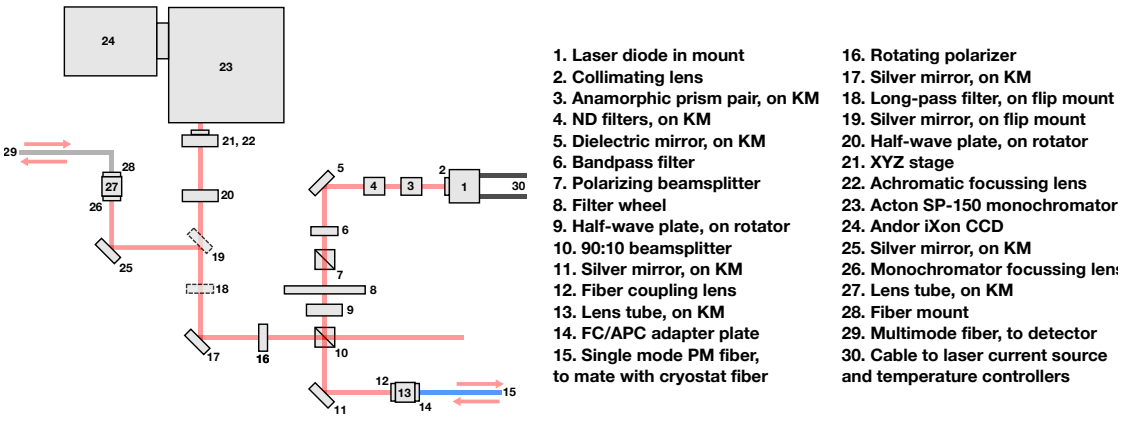

Figure 2.2: Schematic of the room-temperature optical system for a fiber-coupled cryogenic microscope. Here "KM" refers to a kinematic mirror mount. Optics with a dashed outline are placed on flip mounts for easy removal from the beam path.

Figure 2.2 illustrates the room-temperature optical system. The light source is a laser diode in thermoelectrically-cooled mount. One purpose of this optical system is to efficiently couple laser light into a single mode optical fiber, which can then be connected to the cryostat fiber (see Fig. 2.1). For efficient coupling, the incident beam must match the electric-field profile of the fiber mode, which is a gaussian spot about 4 μm wide. If the incident beam is also gaussian with width w and relative position δx, the power coupling efficiency will be about [45]:

$$4\frac{\exp\left(\frac{-2\delta x^2}{w^2+\mathrm{MFD}^2}\right)}{\left(\frac{w}{\mathrm{MFD}}+\frac{\mathrm{MFD}}{w}\right)^2} \tag{2.1}$$

where I have used MFD to indicate the $\approx 4\,\mu$m mode-field-diameter of the fiber. Thus we must focus and place the incident beam with micron-scale accuracy,

or suffer exponential losses of coupling efficiency. We have developed a simple procedure for doing this, which reaches a coupling efficiency of about 50% with a minimum of effort and expense.

Another detail of fiber coupling is the choice of fiber: the microscope fiber has an FC/APC termination, so I couple into a 2 m FC/APC fiber patchcord from Ozoptics. APC stands for, "Angled Physical Contact," meaning that the fiber end-face has been cut at an 8° angle. For light traveling in the fiber, the phase of electric field oscillations will vary across the facet (since the wavefront is not normal to it). To couple into the fiber, the incident light must match these oscillations. According to Snell's law, this condition is met when the light approaches the fiber at 4° (or at 12° to the facet). Therefore, we have to hold the fiber at a 4° angle to the focussing lens, which is done using an, "FC/APC Adapter Plate," to mount the fiber at an angle in a lens tube.

2.1.1 Coupling into a single-mode fiber

The procedure for fiber coupling is described below, with (numbers) referring to parts in Fig. 2.2. First, we collimate and shape the beam with the following steps:

1. Collimate the laser by mounting a single aspheric lens (2) in front of the diode (1). Screw the lens in until the beam maintains its shape over a distance approximately as long as the distance to the fiber.
2. An anamorphic prism pair (3) is used to magnify the beam along one direction, making it more circular. Rotate the prism pair (keeping the sides parallel to the beam) so that the elliptical spot becomes more circular.

Once the beam is approximately circular and collimated, the fiber coupling optics must be aligned:

1. Find an appropriate lens to focus the beam onto the fiber. To couple a laser beam of width w into the fiber, choose the focal length according to $f = \pi \text{MFD} w / 4\lambda$, where λ is the wavelength of the laser.
2. Take the output end of the fiber (15) and illuminate it with a fiber-coupled laser. Any laser that can be placed close to the end of the fiber will work if it is bright enough. The goal is to see light exiting from the fiber coupling lens (12).
3. Change the distance of the fiber coupling lens to the fiber by screwing it along the lens tube (13). Optimize the collimation of the output from the fiber-coupled laser.
4. Change the position, height, and orientation of the lens tube mount so that it is square to the table and the beam path, and the laser diode beam is hitting the center of the fiber coupling lens.
5. Change the orientation of mirror (11) via the micrometer screws of its kinematic mount so that the beam from the laser diode and the beam from the fiber-coupled laser intersect at a point near the fiber coupling lens.
6. Change the orientation of the fiber coupling lens/lens tube via the micrometer screws of their kinematic mount so that the beam from the laser diode and the beam from the fiber-coupled laser intersect at a point near mirror (11).
7. Repeat the above items until the two beams intersect at two points simultaneously. If you now disconnect the fiber-coupled laser and measure the output of the fiber with a fiber-coupled photodetector, there should be a

measurable signal. If not, try increasing the photodetector gain or the laser power.

8. Optimize the signal over the micrometer screws of the mirror and fiber coupling lens kinematic mounts.
9. Change the distance of the fiber coupling lens to the fiber adapter plate (14) by screwing it along the lens tube. Repeat the above two steps until the signal is optimized.
10. Repeat the above step until the signal is optimized.

By following this procedure, it should be possible to reach a coupling efficiency of over 50%. If not, it might be necessary to re-optimize the beam shaping and collimation, or change the fiber-coupling lens.

2.1.2 Introduction to polarization-maintaining fibers

Beyond measuring the energy of photons emitted from the sample, it is also useful to measure their polarization. That way, we can determine information about the internal state (e.g., orbital or spin angular momentum) of the excitations in the sample which decayed to emit the photon. In the case of $MoSe_2$, or other transition metal dichalcogenides, this method can be used to differentiate spectral features related to the opposing K points. In general, any resonance seen in photoluminescence could correspond to emission from multiple degenerate exciton species (with different internal states), but whose degeneracy may be split by applying external magnetic or electric fields. Measuring polarization resolved spectra helps to determine the character of this degeneracy breaking.

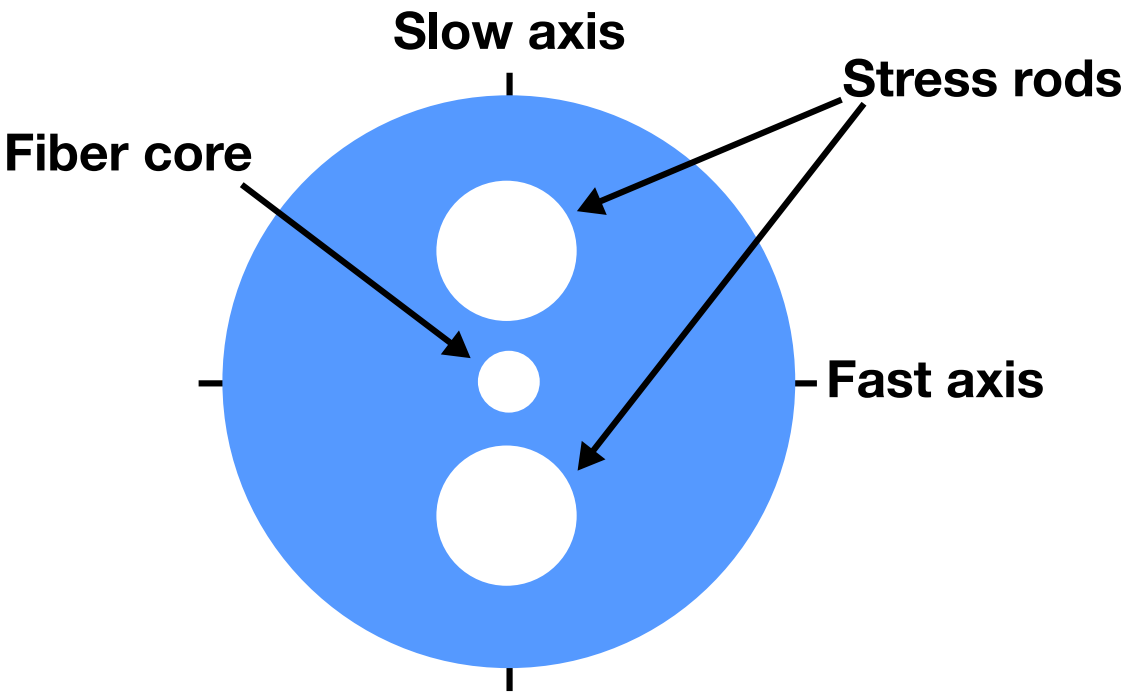

Figure 2.3: Schematic cross section of a Panda type polarization maintaining fiber.

Our fiber-coupled microscope design leads to many inconveniences when attempting polarization resolved measurements. What happens if we try to use an ordinary single-mode fiber to make polarization sensitive measurements? Nominally, the fiber core should be cylindrically symmetric, and light with any polarization should travel through the fiber at the same frequency. If this was true, the polarization state of light entering and exiting the fiber would be the same (aside from adiabatic rotations due to geometry). In reality, random stresses in the fiber lead to birefringences. This means that linearly-polarized light entering the fiber will exit with a random and time-dependent elliptical polarization. Fortunately, many optics suppliers sell something called "polarization-maintaining fiber."

What does polarization-maintaining fiber do? For one thing, it does not

maintain the polarization of light entering the fiber – at least not for arbitrary input states. Simply put, it will maintain two particular polarization states, but no others. These directions are determined by a controlled breaking of the cylindrical symmetry of the fiber core, via stress created by rods inserted into the cladding. The fiber core, cladding, and stress rods of a Panda type PM fiber are shown in Fig. 2.3. Because of this stress, the group velocity of the fiber modes depends on the polarization direction. The light travels more slowly when the polarization is along the "slow axis" indicated in Fig. 2.3. In the basis of the slow and fast axes, $\hat{s}$ and $\hat{f}$, the Jones matrix for a length L of PM fiber is:

$$\mathrm{PMF}(L) = \begin{pmatrix} \exp\left(2\pi i n_f L/\lambda\right) & 0 \\ 0 & \exp\left(2\pi i n_s L/\lambda\right) \end{pmatrix} \equiv \begin{pmatrix} 1 & 0 \\ 0 & \exp\left(2\pi i L/L_\mathrm{B}\right) \end{pmatrix} \tag{2.2}$$

where n_f and n_s are the effective refractive indices. The difference between the effective indices is usually reported in terms of the beat length L_B, which is the distance after which the phase difference between the modes is 2π. A typical beat length will be about 2 mm. Random stresses are also present in PM fibers, but as long as their phase-winding length is much longer than the beat length, the controlled stresses will suppress any mixing between the slow and fast axes.

For an arbitrary input polarization $\sin\theta\hat{s} + \cos\theta\hat{f}$, the output state will be $\mathrm{PMF}(L)\left(\sin\theta\hat{s} + \cos\theta\hat{f}\right) = e^{2\pi i L/L_\mathrm{B}} \sin\theta\hat{s} + \cos\theta\hat{f}$. Therefore, linearly polarized light coupled into the fiber is converted into elliptically polarized light. To make matters worse, the L/L_B in this equation is actually a function of temperature and bending, leading to variations in the phase difference with time. However, if we align a polarizer with one of the fiber axes, we will detect a time averaged power $\propto \sin^2\theta$ or $\cos^2\theta$ depending on whether we align to the slow or fast axis. This means that polarization maintaining fiber is adequate for our spectroscopy needs. We can configure optics in the cryostat to map two orthogonal polar-

ization states in the sample space onto the modes of the fiber. Because there is no mode mixing, we can be sure that the power in the fiber modes reflects the power emitted by the sample into a basis of our choosing. Some information is still missing, since the fiber scrambles the phase between the modes. I will discuss how to map two orthogonal modes of circularly polarized light onto the fiber modes in Section 2.2.

For magnetoluminescence measurements, we expose the PM fiber to magnetic fields of several Tesla. Will the Faraday effect of the fiber create any mode mixing? Of course! The polarization eigenmodes of the fiber in a magnetic field will be somewhere between the linearly polarized modes of the fiber at zero magnetic field, and the circularly polarized modes favored by the Faraday effect. The polarization vector $\mathbf{P}$ at a position x in the fiber is governed by the differential equation:

$$\frac{d\mathbf{P}}{dx} = \begin{pmatrix} 0 & -\nu B(x) \\ \nu B(x) & 2\pi i/L_{\mathrm{B}} \end{pmatrix} \mathbf{P} \tag{2.3}$$

where ν is the Verdet coefficient of the fiber. Equation 2.3 can be mapped to the Schrodinger equation for a spin-$\frac{1}{2}$ in a magnetic field, and allows for many interesting behaviors. Since the real magnetic field is spatially varying, the effective magnetic field varies in time. For $2\pi/L_{\mathrm{B}} \gg \nu B$, where ν is the Verdet coefficient of the fiber, we can estimate a fractional power crosstalk between the modes of order $(\nu B L_{\mathbf{B}}/2\pi)^2$. Assuming a Verdet constant $\nu \sim 20$ (Tm)$^{-1}$, this is only about 0.2% in a 6.7 T magnetic field (the maximum magnetic field we apply).

We may also want to drive the sample with polarized light, which requires aligning the laser polarization with one of the fiber modes. There are two procedures for this, one using incoherent light and one using coherent light. To obtain incoherent light, turn the laser power way down, to the point where

there is almost no visible light. The difference in the laser spectrum between the two regimes is clear: when it is lasing the laser peak will be resolution limited, whereas it will be about 10 nm wide in the low-current regime. The mixture of wavelengths washes out the phase difference $e^{2\pi i L/L_B}$, so that if we analyze the output light with a rotating polarizer we will get a signal proportional to $\cos^2\phi\cos^2\theta + \sin^2\phi\sin^2\theta$, where ϕ is the angle of the polarizer to the fiber axes. Therefore, the maximum and minimum power through the polarizer, $P_{\max}$ and $P_{\min}$, always occur when $\phi = 0$ or $= \pi/2$. This makes it easy to calculate the misalignment of the laser polarization to the fiber modes

$$|\theta| = \arctan\sqrt{\frac{P_{\min}}{P_{\max}}}, \tag{2.4}$$

so that the polarization can be aligned by measuring and minimizing $P_{\min}/P_{\max}$. The simple procedure for doing this is:

1. Find a half wave plate with an appropriate bandwidth for your laser.
2. Mount it in a rotator and place that in the beam path after a polarizer.
3. Collimate the output of the fiber and couple it into a photodetector. Place a polarizer on a rotation mount between them.
4. Rotate the polarizer to maximize the output power.
5. Rotate the waveplate to maximize the output power.
6. Repeat the above two steps until the power is a maximum. Theoretically only one iteration should be necessary since the detected power as function of polarizer angle is always a maximum along one of the fiber axes for incoherent light, independent of the launch angle.

Using this procedure, the $P_{\min}/P_{\max}$ ratio should reach at least 0.01 (-20 dB). After aligning the polarization with incoherent light, the laser can be turned

back up and operated normally. The procedure for aligning with coherent light is more complicated, because the output light will be elliptically polarized, so that the output power as a function of polarizer angle will not have it's minimum or maximum along either fiber axis. To give an example, if the misalignment θ is small, the maximum power is obtained for $\phi = \theta\cos(2\pi L/L_B)$ and $P_{min}/P_{max} = \sin^2(2\pi L/L_B)$. To align the polarization with coherent light, we must use these interference effects to our advantage, with the following protocol:

1. Somehow align the laser polarization close to one of the fiber axes.
2. Rotate the polarization analyzer until the power is a maximum, then rotate it by 45°. This effectively maximizes the interference between the two fiber modes.
3. Use a heat gun to heat up a coiled section of the fiber. Be careful not to make it too hot!
4. Measure the output power on an oscilloscope with a long time constant. You should see the signal begin to oscillate as the fiber cools down from the heating.
5. Rotate the wave-plate to minimize these oscillations.
6. Repeat the above three steps until the oscillations are minimized.

Using this method, it should be possible to get P_{min}/P_{max} much less than 0.01, approaching 30 dB. However, it is more time consuming than the incoherent light method.

2.1.3 Optics for luminescence spectroscopy

Aside from coupling light into the fiber, the room temperature optics also serve to couple light out of the fiber and into the detectors. The two paths are connected by a 90:10 non-polarizing beamsplitter. It is oriented so that 10% of the laser diode output is routed towards the fiber coupling, and 90% of the light exciting the fiber is routed towards the detection optics. The detection optics can be reconfigured without disturbing the fiber coupling optics, and are usually straightforward to align. Simply use a mirror to direct the light towards the detector of choice, or towards a multi-mode fiber which can be used to route the light to a fiber-coupled detector. Here I will describe the alignment of a grating monochromator for luminescence spectroscopy:

1. Couple laser light into the output end of the fiber (15), so that a laser beam is exiting the fiber coupling lens, and being routed to the detection optics through the 90% split of the beamsplitter (10).
2. Move the grating monochromator (23) so that the laser beam is approximately hitting the entrance slit, and enters square to sides of the monochromator. This will require the beam to be approximately normal to the table also, which can be achieved by tuning the mirror after the 90:10 beamsplitter (17).
3. Place a lens (22) on an XYZ stage (21) that will focus the laser onto the spectrometer entrance slit. Choose the lens size so that the angle $w/2f$ will be less than but similar to the spectrometer NA. For the Ralph group's Acton SP-150 spectrometer, NA=0.125. By removing the monochromator lid, you can make sure the beam expands nicely to fill the grating.

4. Measure the power passing through the spectrometer with the entrance slit wide open.
5. Optimize the transmitted power by changing the the distance of the lens to the entrance slit and the centering of the lens on the slit.
6. Close the entrance slit until the transmitted power is low but measurable.
7. Repeat the above two steps until the transmitted power cannot be increased with the slit a few microns wide. Then open up the slit until most of the power is transmitted.
8. Place the detection CCD (24) into the exit focal plane of the spectrometer, and monitor the image.
9. Move and orient the CCD (either with a translation stage or by hand) to optimize the focus.

The setup is now roughly acceptable for spectroscopy. The thinner the spot in the direction perpendicular to the entrance slit, the better the resolution. Feel free to optimize other degrees of freedom – the slit size, lens position, and the mirror (17) – to improve the image. An example of the fully optimized spot shape is shown in Fig. 2.4a, indicating a roughly 3 pixel FWHM. The spectrometer can be calibrated by coupling an argon lamp into the fiber output end, and using the known spectral peaks of the lamp to create a linear interpolation. Figure 2.4b shows the spectrum of our Ocean Optics AR-1 lamp, with the nominal peak identifications.

To take luminescence spectra, it is necessary to filter out the reflection of the excitation beam, since it is much brighter than the luminescence. Thankfully, Semrock provides sharp and powerful long-pass filters that will completely

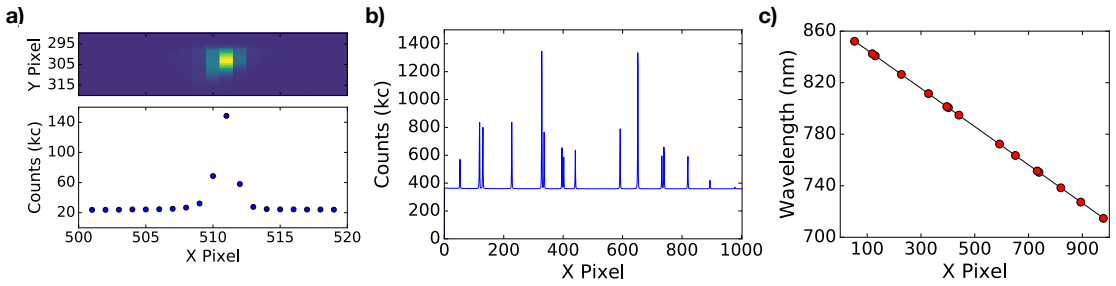

Figure 2.4: **a)** The upper panel shows an image of the laser spot on the spectrometer CCD, with the spectrometer optics aligned. Lower panel: data from the upper panel binned along the Y direction (the direction of the entrance slit). **b)** Spectrum of an Ocean Optics AR-1 argon lamp. **c)** Wavelengths of known resonances of the lamp, versus pixel locations of corresponding peaks in **b)**. The black line is a linear fit that can be used to calibrate the spectrometer.

block the laser light while transmitting > 90% of the longer-wavelength luminescence (the transmission of the filters can often change by more than 60 dB over a 10 nm window of wavelengths). Another tricky point is that the laser diode will weakly emit light over a much broader spectrum than its central peak. The solution is to add a bandpass filter whose pass band does not overlap with the long-pass filter, thereby preventing any contamination of the luminescence signal by laser light.

While taking polarization dependent spectra, it is important to note that the grating efficiency of the monochromator depends on the polarization of the incident light. To take unbiased polarization dependent spectra, I place a polarizer in front of the signal beam, after the beamsplitter. Then, I use a half-wave plate (part 20 in Fig. 2.2) to rotate the incident light onto the most efficient axis of the spectrometer (this means that the waveplate must be rotated by 45° when switching between the two orthogonal polarization directions). Another approach is to orient the waveplate so both polarization modes of the fiber see equal transmission through the spectrometer.

Finally, a word about the operation of single photon avalanche photodiodes (SPAD). We have two SPADs from Micro Photon Devices in our lab, that can be useful for detecting weak luminescence signals: both detectors are thermoelectrically cooled, and have dark counts below 500 counts/second. The counts are read by hooking up the "TTL out" line to a counter (for example on a DAQ). The diameter of the detector active area is 100 μm so that the signal beam should be focussed down onto the detector. I like to couple the signal into a multimode fiber, and then mount the fiber and focussing optics on an XY stage, with the detector on a Z stage. To reach the dark level of 500 counts/second the detector will need to sit in a black-out box that is well sealed against light leaks by black cloth and tape. The detectors can be exposed to ambient lighting when they are not plugged in, but should not be exposed to more than 10^7 photons/second for prolonged periods when they are operating.

2.2 Design of a fiber-coupled confocal microscope

Using a fiber to couple light into the cryostat has the disadvantage of requiring a cryogenic optical system. For some experiments, the optical system can be very simple. For example, photocurrent spectroscopy could be done using the unfocussed output of the fiber. Another possibility is to place the sample directly on the end of the fiber, enabling luminescence, photocurrent, and reflection spectroscopy. Otherwise, if it is necessary to collect the light emitted from the sample, some method must be devised for focussing the laser. Our solution is the compact fiber-coupled microscope shown in Fig. 2.5, which was inspired by similar designs reported in Refs. [46,47].

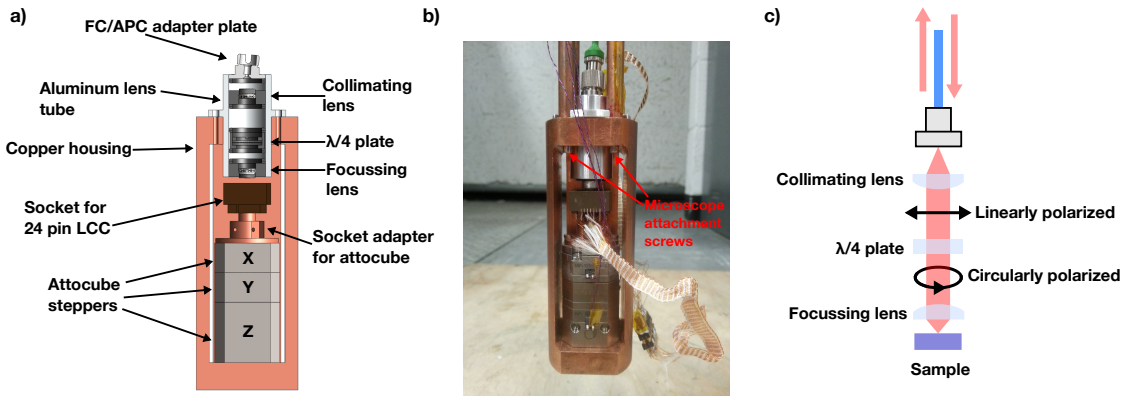

Figure 2.5: **a)** Schematic of compact confocal microscope design, indicating key components. The aluminum lens tube and copper housing are shown in cross-section, so that the optics are visible. **b)** Photograph of assembled microscope, indicating attachment points to the rest of the cryostat.

To create a focussed laser spot, we use off-the-shelf optical components screwed into a custom machined aluminum lens tube. The tube is machined with an 0.535"-40 thread (Thorlabs' SM05 thread) which continues the entire length, and also has flanges for attachment to the microscope assembly. The fiber is coupled into an FC/APC fiber adapter with an SM05 thread. The angled face of the APC fiber prevents Fabry-Perot resonances from multiple reflections between the sample and fiber end-face. The aluminum tube holds two aspheric lenses: a Thorlabs C430TME-B for collimating the fiber output and a Thorlabs C140TMD-B for focussing the collimated beam on the sample. The lenses were chosen because of the compatibility of their various apertures: the collimating lens NA (0.15) is slightly larger than the fiber NA (0.12), and the resulting collimated beam diameter (about 1.2 mm) falls just short of filling the focussing lens (1.6 mm aperture). Furthermore, the small size of these lenses limits chromatic aberrations and Faraday rotations. Of the two lenses, only the position of the fiber collimation lens is critical: this should be screwed along the lens tube until the resulting beam appears collimated. The focussing lens can then be screwed

into the end of the lens tube, with a retaining ring inserted behind it to lock it in place, as shown in Fig. 2.5a. The location of the focussed spot does not move relative to the microscope assembly, so that the sample must be moved into focus.

To do this, we use a set of three attocube stepper nanopositioners. Each has a scan range of 5 mm and moves in discrete steps of 10-300 nm, depending on temperature and applied voltage. The samples are mounted in 28 pin ceramic chip carriers, which can be fit into a socket mounted to the attocubes. The total assembly can be thought of as a scanning confocal microscope, where the single mode fiber acts as both a point light source and detection pinhole [45–47]. As shown in Fig. 2.5c, light exiting the fiber will be focussed down onto the sample, and then reflected back towards the focussing lens. The back-coupling into the fiber is highest when the sample sits in the focal plane of the lens, so that the reflected beam will approximately retrace the path of the incident beam. To focus the microscope on the sample plane, we monitor back-reflected power and optimize it by actuating the z-axis stepper. To find regions of interest on the chip, it is helpful to have large electrical connections (such as wirebonds) which can be followed in from the edges.

Finally, there is a quarter wave plate positioned between the two aspheric lenses, so that it interacts with a collimated beam. For this, I ended up using zero-order quartz waveplates from Special Optics, which can be ordered at any central wavelength and in a convenient 0.5" diameter housing. It is important to use zero-order quartz waveplates (not compound MgF_2/quartz plates), since these are the only readily-available waveplates which are stable over a range of wavelengths *and* down to liquid helium temperatures. The slow axis of the

waveplate is oriented at 45° degrees to the axes of the fiber, so that it transforms circularly polarized light into light linearly polarized along one of the orthogonal fiber modes. In this configuration, if the sample emits light $E_+\hat{\sigma}_+ + E_-\hat{\sigma}_-$, where $\hat{\sigma}_+$ and $\hat{\sigma}_-$ are the Jones vectors for the two circular polarizations, then we can independently measure $|E_+|^2$ and $|E_-|^2$ by measuring the power in the two orthogonal modes of the fiber.

In my photoluminescence spectroscopy experiments, I optimize two quantities before each cooldown: the fraction of light coupled back into the fiber, and the circular polarization of light emitted from the aluminum lens tube. The method I use to carry out the optimization is:

1. If the microscope assembly is attached to the dipstick, remove it. This is done by removing the 2-56 screws indicated in Fig. 2.5b
2. Mount the microscope assembly on a small optical breadboard underneath the cryostat, with the cryostat fiber connected to the microscope fiber mount.
3. Place a small silvered mirror mounted in a ceramic chip carrier into the sample holder, and focus the microscope on it.
4. Remove the aluminum lens tube from the microscope assembly, and remove the focussing lens from the lens tube.
5. Mount the lens tube on the bread-board using the custom machined aluminum adapter (it is a plate with a hole in it and threaded holes mating to the flange of the lens tube.
6. Shine light from the room temperature optics into the fiber so that a somewhat collimated beam is exiting the lens tube. The room temperature op-

tics should be optimized so that linearly polarized light is being coupled into one of the fiber polarization modes.

7. Use a photodetector and polarizer to measure the polarization of the light exiting the lens tube.
8. Rotate the quarter-wave plate in the lens tube to minimize the polarization of the light exiting the lens tube (thereby maximizing its circular polarization). Screw the waveplate down with a retaining ring, being careful not to let it rotate too much during the screwing down.
9. Using a quarter-wave plate, polarizer, and photodetector, measure the degree of *circular polarization* of the laser light exiting the lens tube. Record this number.
10. Put the focussing lens back in, and mount the lens tube back in the microscope assembly.
11. Focus the microscope by maximizing the reflected signal. Now check what fraction of the input power is being reflected out of the microscope.
12. If this fraction is less than 10%, or optimized back-coupling is required, unscrew the fiber and rotate the fiber mount to slightly change the distance between the collimating lens and the fiber end face. Then screw the fiber back in.
13. Repeat the above two steps until the desired back-coupling efficiency is reached.
14. Repeat steps 3-9.

It should be possible to achieve 95% circular polarization without trouble, but the back-coupling efficiency is unreliable. The last step should always be

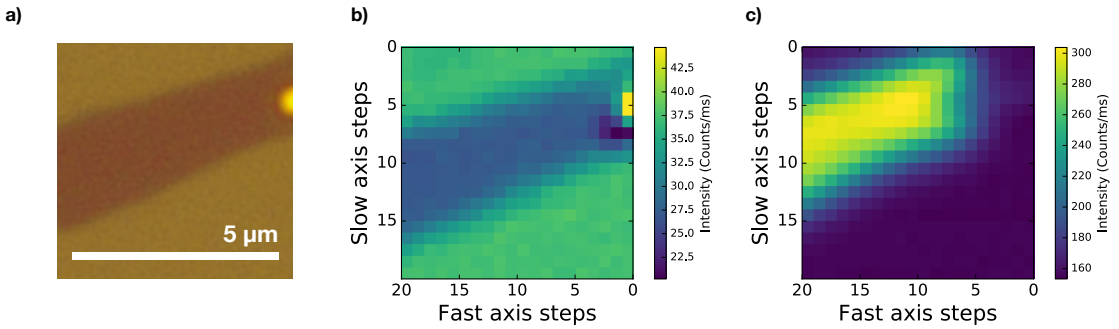

Figure 2.6: **a)** Image of a $MoSe_2$ monolayer taken with a commercial microscope. **b)** Reflection image of the same sample taken in our microscope at 4.2 K. **c)** Photoluminescence image of the same sample taken in our microscope at 4.2 K. The excitation was blocked with a Semrock bandpass filter centered at 769 nm, and the luminescence counts were measured with a single photon avalanche photodiode.

step 8, since this is the only way to know the circular polarization efficiency and the back-coupling efficiently. Also note that the connection between the microscope fiber and the optical table fiber can be problematic. Wiggle the connection at some point to maximize the overall reflected signal.

After the microscope optics are optimized, it is time to find the sample. This is done by monitoring the back-reflected signal, and following landmark features in from the edges of the chip. When a wirebond is blocking the beam, no light will be reflected, making wirebonds a recognizable and useful feature for finding the sample. The steppers can also be raster scanned to take simple images. Fig. 2.6 compares an optical micrograph with reflection and photoluminescence images of a $MoSe_2$ monolayer taken by rastering the steppers. The nanopositioner step size is different moving forward and backward, so that the fast-axis scan region will drift as the slow axis is stepped. Even a 1-pixel per raster forwards-backwards asymmetry will cause the actual scan window to be tilted at 45°! Thankfully, the steppers can be trained to take a square image by

repeating the same scan multiple times. This is described in detail by attocube engineers in Ref. [48].

2.3 Design of a dipstick cryostat

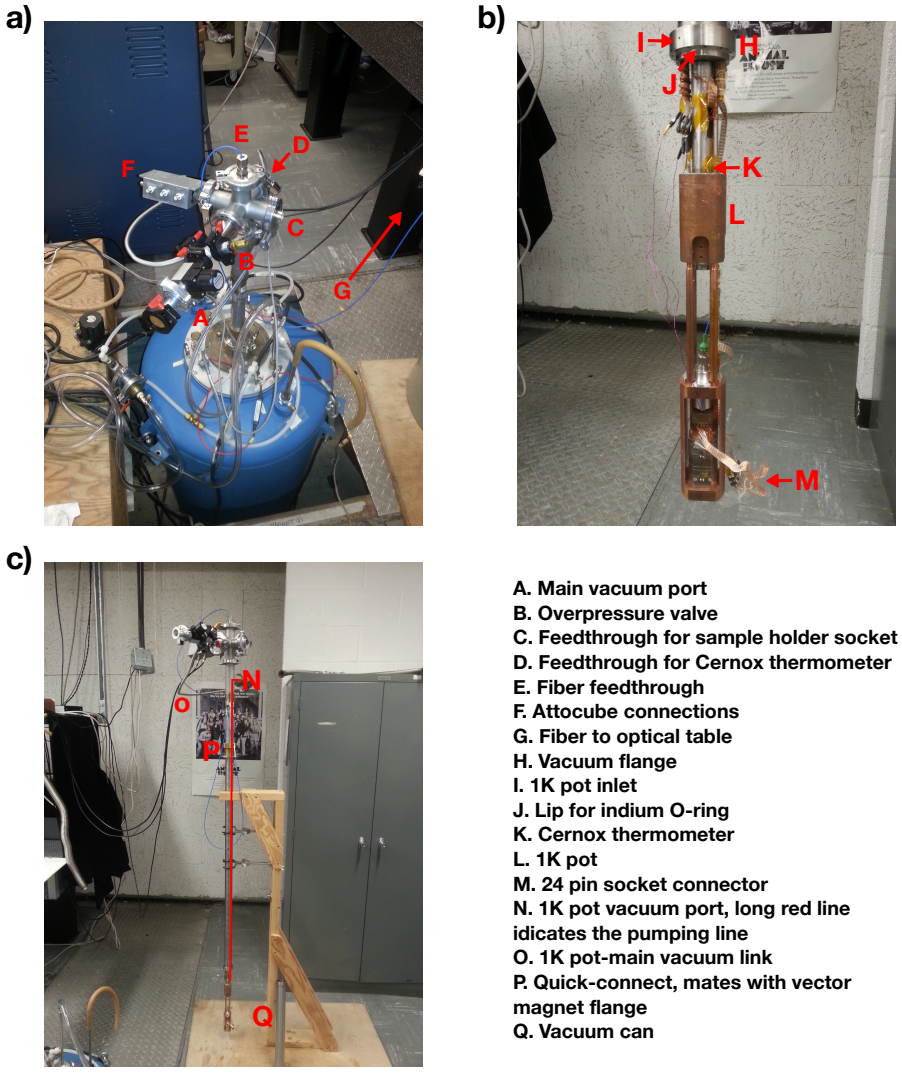

Figure 2.7: **a)** Photograph of the dipstick cryostat ready for operation, inserted into the bore of the vector magnet. The vacuum and electrical feedthroughs are labelled. **b)** Photograph of the cold-finger of the cryostat, below the vacuum flange. **c)** Full view of the dipstick.

Several images of the fully assembled cryostat are shown in Fig. 2.7. Starting from the top, Fig. 2.7a shows the six way vacuum cross. Each arm of the six way cross is connected to a feedthrough for different optical, electrical, and vacuum lines running into the cryostat. Port E is connected to a Ozoptics fiber vacuum feedthrough, which is a teflon swagelok fitting tightened around a polarization maintaining fiber. The Ozoptics feedthroughs are shipped connected to a 0.25" pipe thread. To make a KF feedthrough, I epoxied this into a KF flange with a hole in it, using Stycast 2850. Port A is connected to the vacuum space of the cryostat. There are actually two vacuum spaces: the main vacuum space and the 1K pot vacuum space. In principle, the fridge is equipped with a 1K pot and 1K pot pumping line (Port N), but I have not left the 1K Pot in an operational state, and instead connect the 1K Pot vacuum to the main vacuum space and pump on both simultaneously. Port C holds a 26 pin mil-spec connector, which provides electrical connections to the microscope socket (see Fig. 2.8 for the pinout). Port D holds a 19 pin mil-spec connector, which provides electrical connections for a Cernox thermometer mounted on the 1K pot. This port can be connected to a lakeshore LTC-21 temperature controller by a custom-made cable, which should be kept with the cryostat. The calibration data for the thermometer should be kept with the American Magnetics manual for the system. Port F is connected to a BNC breakout box for the attocubes. The "X" and "Y" BNC receptacles are connected to the horizontal steppers, while the "Z" port is connected to the vertical stepper. These ports should always be connected to the attocube controller when the attocubes are connected to the cryostat lines, and should be grounded through the controller when not in use.

The final port is connected to a roughly 5' long stainless steel tube, which comprises the main vacuum space of the cryostat and carries the wires, optical

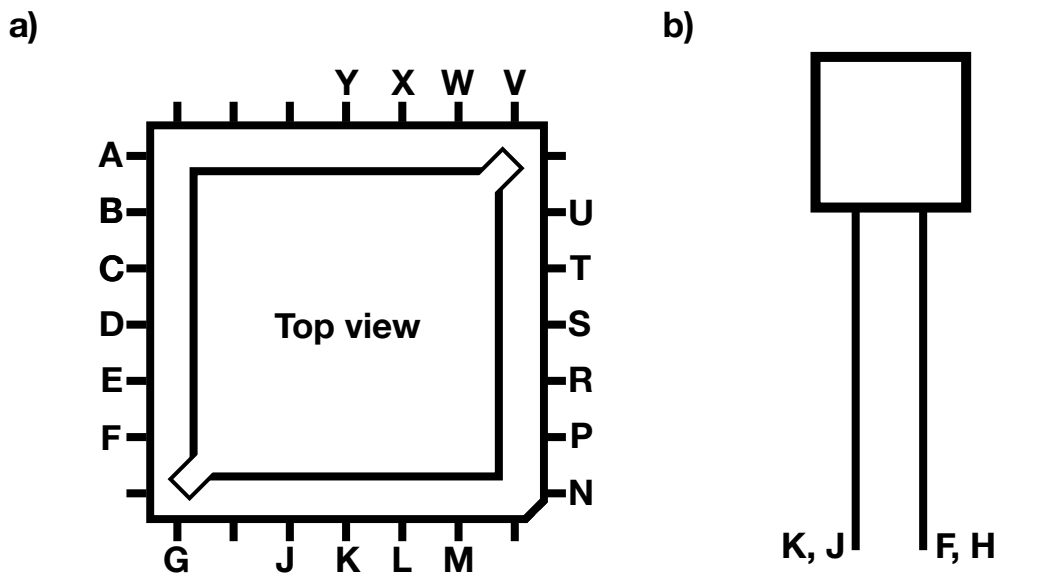

Figure 2.8: **a)** Pinout for the sample holder socket (numbers refer to pins on port C of Fig. 2.7) **b)** Pinout for the Cernox temperature sensor (numbers refer to pins on the 19 pin mil spec connector, which is D port of Fig. 2.7).

fiber, and 1K pot pumping line, down to the lower vacuum flange. There is also a series of aluminum baffles hung from the optical fiber flange by a stainless steel rod. The components inside the vacuum tube are very difficult to modify without destructively disassembling some part of the cryostat; it's possible to fix bad solder joints on the feedthroughs by gently opening up the corresponding flanges, but that's about it. In retrospect, this was a tremendous design error. If anyone reading this is contemplating a similar system, I highly recommend having the wiring, optical fibers etc. wrapped around a single sturdy rod hanging from the six way cross, and then covering this all with a very long vacuum tube which makes a KF seal with the bottom port of the six way cross. This avoids the use of cold vacuum seals and also makes it easy to repair any problems with the wiring, plumbing, or optical fiber.

The "cold finger" of the cryostat is shown in Fig. 2.7b. The 1K pot is con-

nected to the lower vacuum flange by a stainless steel rod, and the microscope assembly is connected to the 1K pot by four copper rods. The microscope assembly itself is designed to be modular, and can be removed from the cryostat by removing the 2-56 screws indicated by the red arrows. The electrical connections come out of the stainless steel tube above the 1K pot and are wrapped around thermalization posts, while the optical fiber travels straight through the center of the 1K pot (the 1K pot is toroidal) and down to connect to the fiber mount of the microscope. The helium inlet for the 1K pot can be seen on the vacuum flange, but I have left the output of this hole inside the can sealed up with a small wire and solder. This seal is prone to leaking, and is the first place to check if there is an apparent leak. To put the 1K pot into use, the small wire should be removed from the seal and a capillary tube should be added connecting the hole to the 1K pot. Also visible in this figure are the low-resistance twisted pairs used to connect to the attocubes. Each pair mates to another twisted pair near the vacuum flange, which then runs up the vacuum tube. It is important to match the signal pin of the attocubes (the red socket on the attocubes) to the ground pins of the fridge lines (marked on the low-temperature end with white dots). Failure to do this risks damage to the attocubes.

During operation of the cryostat, everything below the lower vacuum flange is covered by a stainless steel vacuum tube with a matching flange. The seal is made with an indium O-ring. The procedure for making this O-ring is described in the next section, along with other protocols for operating the cryostat.

2.4 Operation of a cryogenic confocal microscope

Once the all the optics are optimized and the sample is in the microscope focus, the cryostat is ready for cooldown. The first step is to use Kapton (or teflon) tape and dental floss to secure all the wires so that they fit in the footprint of the microscope assembly. This ensures that the vacuum can will fit on without scratching any wires. To seal make the indium vacuum seal, I use the following protocol:

1. Put on gloves!
2. Find 1/16" indium wire. The Ralph group has a large supply, and it can also be created by pushing liquid indium (it melts at 157°C) through a die with the hydraulic press in the machine shop.
3. Clean a length of the indium wire with isopropanol, and then coat it with a very thin layer of vacuum grease.
4. There is a another instance of the stainless steel lower vacuum flange that is not connected to anything. Wrap indium wire around the lip on this part, and cut off a piece of wire slightly longer than the circumference of the lip.
5. Take this piece and wrap it around the lip on the stainless steel flange of the actual cryostat. The vacuum grease should let it stay on against the force of gravity.
6. Run your fingers along the wire several times while pressing down. It should get longer and skinnier, and pushed into the corner of the lip.
7. Cut the wire with a razor blade, so that it is just slightly longer than the circumference of the lip.

8. Overlap the extra lengths of the wire and press them together with your fingers or toothpicks, making sure the wire stays flush against the lip everywhere.
9. Slide the vacuum can onto the lip, place 12 new 2-56 screws through the holes on the vacuum flange, and finger tighten the screws.
10. Use hex keys to simultaneously tighten the screws on the opposite sides of the flange, and move around in a circle.
11. Now you can pull vacuum by pumping on the vacuum port of the six way cross.
12. Wait for a few hours while occasionally tightening down all the screws. The indium will be squished by the vacuum, so it should be possible to tighten it a bit more while pumping down.

Using this method, I have never failed to make a high-quality seal that survives to low temperatures! The dipstick takes awhile to pump down, but should be able to reach well below 10^{-6} Torr when cold. Once the system is under vacuum, it can be moved into the vector magnet. The quick-connect flange on the dipstick mates to the ISO flange on the neck of the vector magnet. There should be lines drawn on the dipstick which indicate where to put the top of the quick connect assembly so that the sample is near the magnetic field center. The sample will also be near (but below) magnetic field center if the vacuum can touches the bottom of the vector magnet. The operation and cooling procedures for the vector magnet are well described in Kiran Thadani's dissertation. My only note is that it is easiest to cool the system down if the liquid nitrogen pre-cool is done with the dipstick in the vector magnet, so that the dipstick will also be cooled

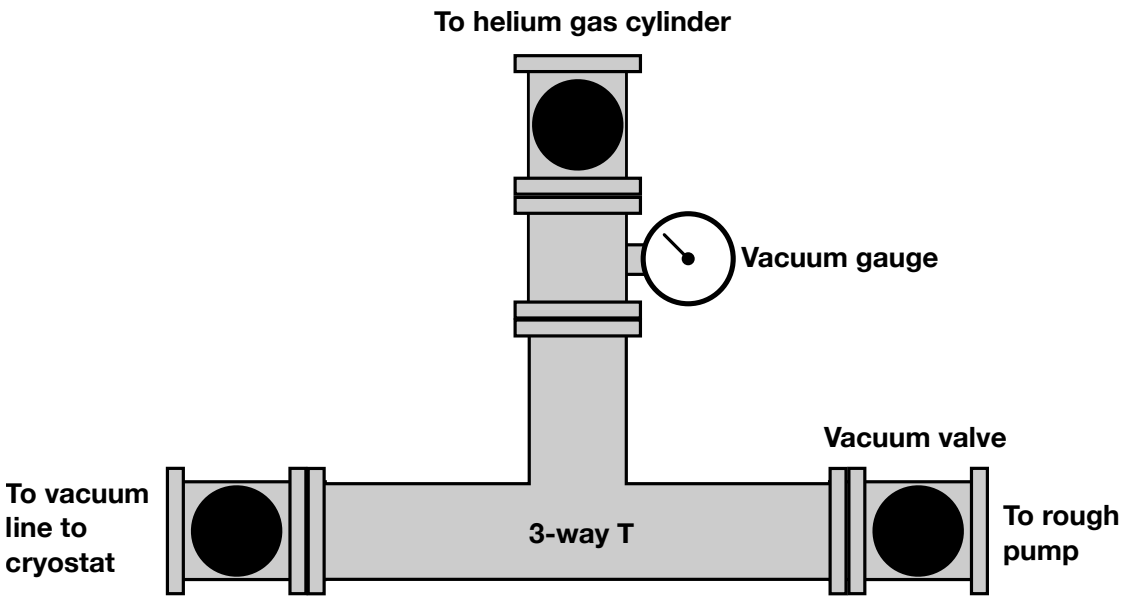

Figure 2.9: Schematic of the vacuum system used to controllably add small quantities of helium gas to the cryostat vacuum tube.

to liquid nitrogen temperatures. Otherwise, the dipstick can be pre-cooled separately using a small dewar, and then transferred into the liquid helium filled vector magnet while still cold.

The main thermal connection of the microscope and 1K pot to the helium bath is the thin stainless steel tube attaching the 1K pot to the vacuum flange. The thermal conductivity of this tube is low, so it will take a long time to cool the microscope down to liquid helium temperatures (the higher the vacuum is, the longer it will take). This is intentional, since cooling too rapidly could crack the optics. I usually leave it to cool down overnight after transferring helium into the bath. Thermal contraction will cause the microscope to go out of focus as it cools, so it's important to periodically refocus the microscope to avoid losing the sample. To fully thermalize the microscope at 4.2 K (and to ensure that the sample remains cold during measurements), I add a small amount of helium gas to the dipstick vacuum. The plumbing for doing this is shown in Fig. 2.9.

The process for bleeding helium gas into the dipstick is:

1. Hook up the plumbing shown in Fig. 2.9 and connect a helium cylinder to the gas line.
2. With the valve to the cryostat and the needle valve on the regulator closed, rough out the vacuum tee and the gas line with a dry roughing pump. Keep the valve to the bellows open at this stage.
3. Close the needle valve to the gas line and the valves to the bellows (labelled "To vacuum line to cryostat") and the roughing pump.
4. Open up the needle valve on the regulator, filling the gas line with helium.
5. Slowly open up the needle valve on the gas line, and let the pressure rise to about 50 Torr.
6. Close every valve.
7. Open the valve into the bellows and then the valve into the cryostat. The helium gas will get cryopumped in.
8. Repeat the process until the temperature is falling at the desired rate.

Once the system is stable at 4.2 K, the low-temperature operation of the microscope is identical to it's room temperature operation. The main difference is that the attocubes will require a higher drive voltage to step (around 40-50 V) and their minimum step size will be smaller. Another issue occurs when a strong magnetic field is applied. I find that, as the magnetic field is increased above a few Tesla, the microscope will completely defocus and the focussed spot will move 10's to 100's of microns across the sample surface. Great familiarity with the operation of the microscope is required to refocus after such a shift.

The most magnetic component of the microscope seems to be the metal of the fiber connector based on tests at room temperature. I have conducted some experiments with changing the overall height of the microscope in the vector magnet while taking magnetoluminescence measurements. Based on these tests, it seems that there is a sweet spot where the microscope does not defocus even in a 6.7 T field, and the magnetic field applied to the sample is near its maximum value. My preliminary results suggest this spot is obtained by raising the dipstick about 10 mm above the position marked on the vacuum tube, but further testing is required.

If one was so inclined as to improve the setup, I would recommend ditching the fiber connector altogether. This could also improve the back coupling efficiency. A micromanipulator stage could be used to position a bare fiber while monitoring the back-coupling efficiency. Then epoxy could be used to glue the fiber into place. This would also simplify the process of pulling the fiber through the vacuum tube, since the bulky fiber connector made this very difficult.

In the next section, I will describe our experiments measuring magnetoluminescence spectra on a bulk CdTe single-crystal. This section will serve the dual purposes of validating the microscope operation and introducing a few more practical details of how we measure magnetoluminescence spectra.

2.5 Magnetoluminescence of CdTe

In this section I will report measurements of photoluminescence spectra from bulk CdTe at 4.2 K and in magnetic fields up to 6.7 T, giving detailed examples of the experimental procedures. Before the measurements, we optimized the

microscope optics as described in Section 2.2. With the aluminum lens tube out of the microscope assembly, a quarter-wave plate, polarizer, and a 780 nm laser diode were arranged to shine incoherent circularly polarized light into the focussing lens of the lens tube, coupling light into the cryostat fiber. We measured the resulting power in the two fiber polarization modes at the room temperature end of the fiber, finding that 93% of the power was concentrated in a single mode. This measurement also allowed conclusive determination of the angle of the fiber axes with respect to the room-temperature polarization analysis optics. The 7% cross-talk between the polarization channels is higher that what should be possible give the specifications of the polarization-maintaining fiber and quarter-wave plates; it could arise from misalignment of the waveplates, retardance error, or mixing between fiber modes in strained regions. As long as the sample emits σ_+ and σ_- light with roughly equal intensity, this degree of cross-talk does not prevent reliable measurements of polarization-dependent magnetoluminescence spectra.

Next, we silver-painted a *p*-type CdTe crystal (from MTI corporation) into a ceramic chip carrier, loaded it into the microscope, and put the vacuum can on. Following the procedures of the preceeding sections, we moved the dipstick into the vector magnet and began the process of cooling down the cryostat. As the magnet was cooling, we coupled light from a 780 nm diode into the optical table fiber, and used that to align the spectrometer optics (the resulting laser spectrum is shown in Fig. 2.4a). We actually waited until after the magnetoluminescence measurements to calibrate the spectrometer, but I will describe the calibration here. We coupled the AR-1 argon lamp into the table fiber, obtaining the spectrum in Fig. 2.4b. Figure 2.4c plots the identifiable peak positions versus pixel number, along with an excellent linear fit. The slope is -0.1486 nm per

pixel. In the data presented below, I use this fit to translate pixel numbers into wavelengths, and then use $E = 2\pi\hbar c/\lambda$ to calculate the photon energy. It is also possible to take the slope from the argon lamp calibration, but use a known reference point, such as a filter cut-off, to provide the absolute scale. This is useful to avoid redoing the calibration if the spectrometer is slightly shifted.

To excite luminescence, we coupled 380 nW of light from a 656 nm laser diode into the cryostat fiber. The polarization of the excitation light can be varied by rotating a half-wave plate placed in front of the 90:10 beamsplitter (recall Fig. 2.2). For these experiments, we rotated the linear polarization of the laser diode to lie at 45° to the fiber axes, so that the sample is illuminated by an equal mixture of left and right circularly polarized light. The excitation is coherent, but the phase introduced between the fiber modes by the fiber birefringence is unknown; therefore the excitation light is linearly polarized (in the sample space) but with an unknown direction! If a circularly polarized excitation were used, it could lead to circularly polarized luminescence, even at zero magnetic field. This is sometimes called optical orientation or polarization-preservation, and can obscure circular polarizations arising from magneto-optical effects.

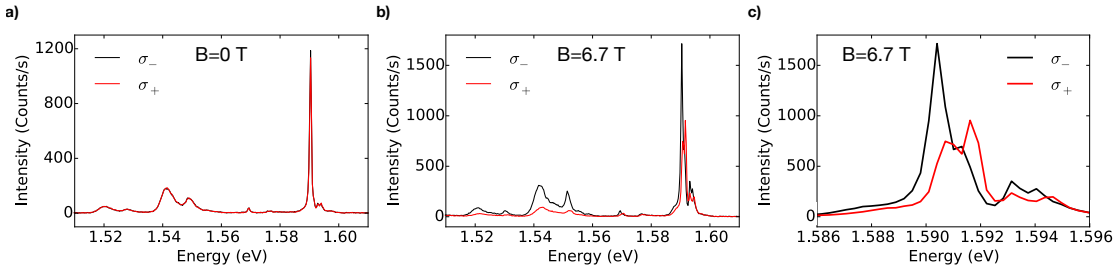

Figure 2.10: **a)** Polarization-dependent photoluminescence spectra for our CdTe single crystal at 0 T. $\sigma_\pm$ polarization refers to the circular polarization with angular momentum $\pm\hbar$ along the field direction. **b)** Polarization-dependent photoluminescence spectra for our CdTe single crystal at 6.7 T. **c)** Zoomed in view of the data in **b)**

Figure 2.10 shows polarization-dependent photoluminescence spectra for our CdTe single crystal at 0 T and 6.7 T. For the data shown here, we ramped the out-of-plane magnetic field to 6.7 T, and then decreased it in 1 Tesla increments (except for the 6.7 T to 6.0 T increment), taking data at every step. The explicit measurement procedure was:

1. Let the magnetic field stabilize at the set point.
2. Focus the microscope with the excitation laser, using a SPAD to monitor the back-reflection signal.
3. Use a flip mount to place a Semrock 715 nm long-pass filter (FF01-715/LP-25) in the beam path.
4. Step z-axis attocube about 30 steps away from the focussing lens at 50 V drive. This is done since the luminescence and excitation have different focal points due to chromatic aberration. Often the luminescence intensity can be significantly increased and the back-reflected excitation decreased by changing the microscope focus.
5. Use a flip mount to remove the mirror that sends light to the SPAD from the optical path, allowing light to enter the monochromator.
6. Rotate the detection polarizer to a predetermined position aligned to one of the fiber modes. Rotate the detection waveplate to a predetermined position where this fiber mode is rotated to lie along the most sensitive axis of the monochromator.
7. Open the CCD shutter, and record a spectrum. For our CdTe magneto luminescence measurements we used a 60 s exposure time. We also used hardware binning to average along the direction perpendicular to the dispersion direction. This is not necessary, but reduces the file size.

8. Repeat the above two steps, but with the predetermined polarizer and waveplate orientations appropriate for measurements of the orthogonal polarization channel.
9. Close the shutter, and begin ramping the magnetic field to a new value.

This procedure is optimized for measuring the polarization-dependence of the emission. That is why the different polarization channels are sequentially measured at each magnetic field value, instead of fixing the detection polarization and sweeping field (and then repeating this for the orthogonal detection polarization). If the later procedure were taken, there could be no direct comparison between the two polarization channels since the microscope focal point drifts irreversibly with magnetic field, and the spectral peaks slightly shift in position over the sample. For TMD luminescence measurements, there is a critical addition to this protocol: after the spectra are measured for the two polarizations, we move away from the sample, defocus the microscope, and repeat the process. The purpose of this is to obtain the spectrum of Raman photons generated by inelastic scattering of the excitation laser in the optical fiber (see Section 3.6.2 for more details). The fiber Raman background is visible in Fig. 2.10, but the CdTe luminescence is strong enough to obviate any background subtraction. However, we did subtract the dark counts, by rescaling and subtracting the spectrum from a nearby dark region of the CCD.

What can we learn from our measurements? Figure 2.10a shows polarization dependent measurements taken with zero applied magnetic field. There we see a number of peaks, each with nearly polarization independent intensity and position. This indicates that our measurement setup has roughly equal collection efficiency for the two circularly polarized detection channels. We can guess the

origin of these peaks based on previous studies [49,50]. For p-type CdTe, we expect that the intense, narrow, peak arises from recombination of acceptor bound excitons. The other peaks could arise from other (e.g. donor) bound excitons. Some of the peaks (e.g. the small one at 1.569 eV) seem to be redshifted from another peak by about 21 meV. This is the energy of an optical phonon of CdTe, indicating that these peaks may be phonon replicas created when excitons emit a phonon and photon upon recombination. We can also use luminescence spectra in an applied magnetic field to calibrate the angular momentum of circularly polarized photons collected in our two detection channels.

Figure 2.10b shows luminescence spectra for CdTe taken in a 6.7 T applied magnetic field. There, we see that peaks in one polarization have been redshifted and become more intense, while peaks in the other polarization have blueshifted and become less intense. A narrow view of the acceptor bound exciton peak is shown in Fig. 2.10c. In addition to the polarization dependent peak shifts, there are also peak splittings within each detection channel (barely visible due to the ≈ 0.3 meV resolution of our spectrometer). This fourfold pattern of peak splitting is similar to that measured in Refs. [49,50]. The fourfold splitting can be derived by assuming that electrons radiatively decay from a spin-1/2 conduction state to a spin-3/2 valence state. The lowest energy peak arises from recombination of $s_z = 1/2$ electrons with $s_z = 3/2$ holes, where the $\hat{z}$ direction is chosen parallel to the applied magnetic field. We can therefore identify the polarization of this peak as "σ_-," which we define as the circular polarization where the photon angular momentum is antiparallel to the applied magnetic field. This determines the labels given in Fig. 2.10. The splittings can be parametrized in terms of effective g-factors, where $\mu_B g_{e(h)} \mathbf{J} \cdot \mathbf{H}$ is the Zeeman energy of conduction and valence band Bloch states. We find $g_e \approx -1.6$ and

$g_h \approx 0.5$, in good agreement with Refs. [49, 50].

Overall, our measurements of CdTe magnetoluminescence provide confidence in the ability of our microscope to measure i) the overall circular polarization of luminescence and ii) circular-polarization-dependent peak shifts. These measurements also provide a simple method of calibrating the sign of peak shifts i.e. allowing us to determine the mapping between circular polarizations emitted by the sample, and linear polarizations detected at the spectrometer. This mapping can be verified by direct analysis of the optical system. Immediately after taking the CdTe magnetoluminescence data, we measured the direction of the magnetic field for a given power supply current. We found that what the vector magnet power supply calls "positive" current – what we label here as positive field – points towards the floor. We had also previously analyzed the handedness of light emitted from aluminum lens tube with a single fiber polarization mode excited. The results were consistent with the calibration from CdTe magnetoluminescence, after carefully determining the slow-axis of the quarter-wave plate used to analyze the circularly polarized light. From my experience, one should not trust the vendor's labelling of the waveplate fast and slow axes, and instead determine them through some other means (more on this in Section 3.6.5).

One final note: I use the convention that $\sigma_\pm$ polarized light has angular momentum $\pm\hbar$ along the magnetic field, for *positive* magnetic field. This is contrary to the convention that considers $\sigma_\pm$ polarized light to always have angular momentum $\pm\hbar$ along the applied magnetic field. In the case of TMDs, my convention means that $\sigma_\pm$ polarized light will always excite excitons in the $K_\pm$ valley.

CHAPTER 3

BREAKING OF VALLEY DEGENERACY BY MAGNETIC FIELDS IN MONOLAYER MOLYBDENUM DISELENIDE

The following chapter is based on work published in Physical Review Letters (Ref. [51]), and appears here with modifications, corrections, and additional discussions. The biggest change is an expanded discussion of attempts to calculate the exciton's magnetic moment, contained in Section 3.7.

3.1 Introduction

Monolayer $MoSe_2$ and other monolayer transition metal dichalcogenides (TMDs) are a materials system with unique potential for controlling their valley degree of freedom [27, 35, 52–57]. Similar to graphene, the conduction and valence band show extrema (valleys) at the vertices of a hexagonal Brillouin zone; unlike graphene, $MoSe_2$ exhibits a nonzero optical gap of 1.66 eV [37, 58]. This has allowed exploration of optoelectronic properties arising from the valley-dependent chirality of massive Dirac fermions predicted in the context of inversion symmetry broken graphene [34, 59]. As discussed in Section 1.2.2, this chirality leads to optical selection rules coupling the exciton valley degree of freedom to photon handedness [35, 52–56]. Using polarization-resolved spectroscopy researchers have demonstrated valley-selective photoluminescence with near 100% fidelity [52, 56]. Furthermore, the ability to pump valley-polarized carriers with circularly polarized light has been demonstrated through the valley Hall effect [57]. The chiral electronic states are also predicted to posses valley-contrasting orbital magnetic moments coupling valley pseudospin to magnetic field [30, 34, 59–63], which opens up the possibility for mag-

netic control over the valley degree of freedom [30, 64].

In this chapter, I will discuss our experiments demonstrating the breaking of valley degeneracy by magnetic fields in monolayer TMD $MoSe_2$. We detect valley degeneracy breaking by measuring polarization-resolved luminescence spectra for back-gated $MoSe_2$ devices at 4.2 K and in magnetic fields up to 6.7 T. By studying the luminescence peak energies as a function of magnetic field, we find a linear splitting of $-0.22\frac{\text{meV}}{\text{T}}$ between peaks corresponding to light emission with different senses of circular polarization, σ_+ and σ_-. We interpret this as a Zeeman splitting due to valley-dependent magnetic moments. We also investigate the magnetic-field dependence of luminescence handedness, finding that the emission becomes circularly polarized in a magnetic field even with unpolarized excitation, and that the degree of this polarization can be increased to about 50% by gating the sample. This suggests that electric fields can facilitate the generation of valley-population imbalance in samples where valley degeneracy has been broken by magnetic field. Our results demonstrate a recently-proposed [64] strategy for generating valley populations, and could lead to new approaches for controlling the valley degree of freedom in monolayer TMDs.

3.2 Device geometry and measurement apparatus

Our device geometry and measurement apparatus are shown in Fig. 3.1a and 3.1b. All measurements were taken using a scanning confocal microscope integrated with a 7 T superconducting magnet dewar, with light coupled in and out of the system via a polarization-maintaining optical fiber (similar designs were reported in Refs. [46, 47]). The light is focused into a roughly 1 μm di-

ameter spot using a pair of aspheric lenses, and the sample is scanned using piezo-driven nanopositioners (from attocube). The sample, positioners, and optical components are placed in a vacuum cryostat which is then evacuated and lowered into a helium bath containing a superconducting magnet; helium exchange gas is added to ensure thermalization of the sample at 4.2 K. Except for data shown in Section 3.6.6, the excitation power was between 10 and 60 μW.

To enable polarization-resolved spectroscopy, a zero-order quartz $\lambda/4$ plate is placed between the aspheric lenses, oriented at 45° to the fiber axes; this couples σ_+ and σ_- emission into orthogonal polarization modes of the fiber. The light exiting the fiber is directed though a rotatable polarizer, which selects one fiber mode for spectral analysis by a spectrometer with a thermoelectrically-cooled CCD. We can also create a circularly polarized excitation by coupling linearly polarized light into one of the two fiber polarization modes, or create equal intensity excitation in σ_+ and σ_- polarization by coupling in light polarized at 45° to the fiber axes. We excite luminescence with light from a 1.89 eV laser diode, which is 230 meV blueshifted from the A exciton transition, and as a result, we see little dependence of the emission polarization on excitation polarization (see Section 3.6.1). The conclusions discussed below are independent of excitation polarization.

To fabricate our samples, we exfoliate bulk $MoSe_2$ crystals (grown by direct vapor transport) onto 300 nm silicon oxide on silicon, then use electron-beam lithography to define a single 0.5 nm Ti and 75 nm Au contact, allowing use of the silicon substrate as a back gate. All data shown in the Sections 3.2–3.4 were taken from devices $D1$ and $D2$ pictured in Fig. 3.1c. Figure 3.1d shows the $B = 0$ luminescence spectra of $D2$ at -30 V, 0 V, 10 V, and 50 V. The peaks at 1.66 eV

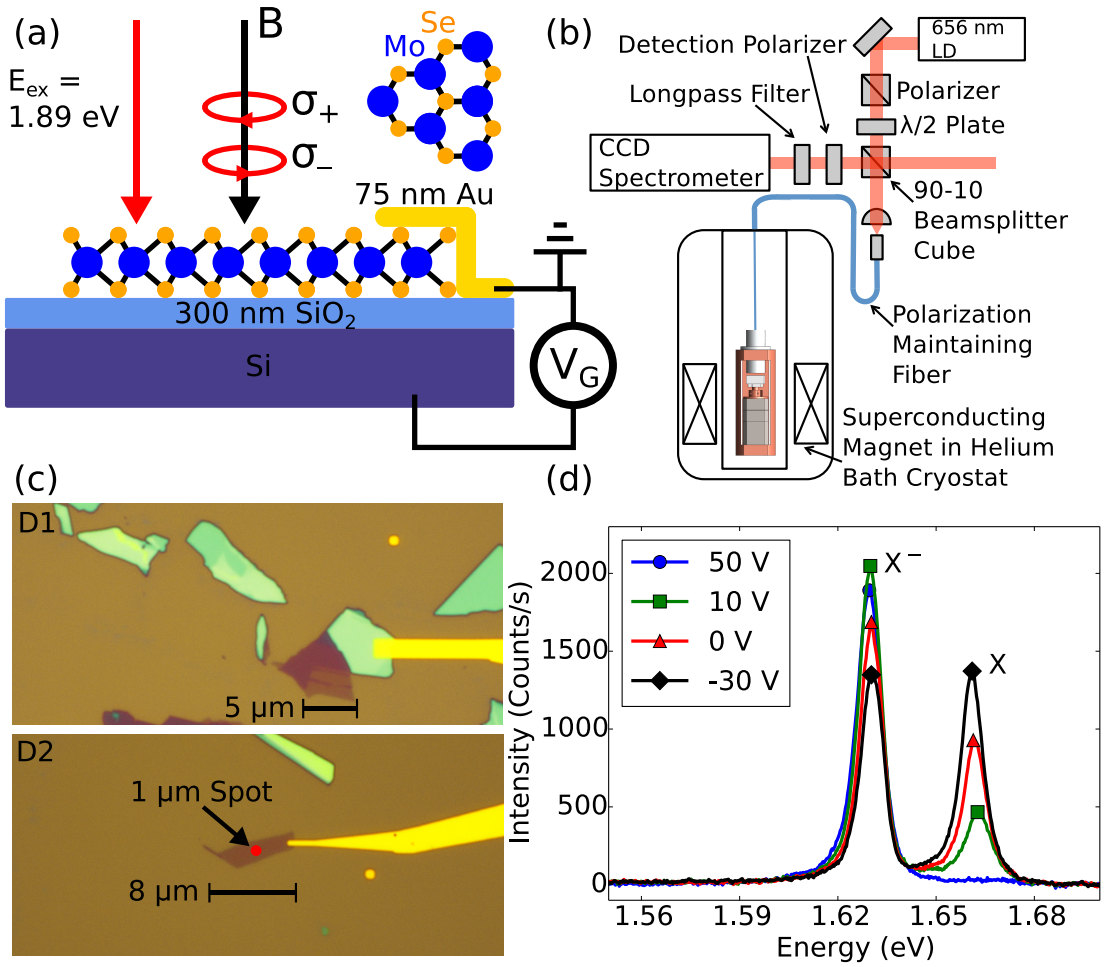

Figure 3.1: **(a)** Experimental geometry showing back-gated monolayer $MoSe_2$ devices in out-of-plane magnetic fields. Luminescence is excited with light from a 1.89 eV laser diode and collected separately for σ_+ and σ_- polarization in the Faraday geometry. **(b)** Schematic of the fiber-coupled optical cryostat used in the experiment. **(c)** Optical micrographs of devices $D1$ and $D2$. **(d)** Luminescence spectra of $D2$ taken at 0 T and 4.2 K with -30 V, 0 V, 10 V, and 50 V back-gate voltage.

and 1.63 eV correspond to the neutral and charged *A* exciton respectively, with a charged exciton (trion) binding energy of 30 meV [37]. As the back-gate voltage is increased, the exciton luminescence decreases and the trion luminescence increases, showing that our samples are intrinsically *n*-type and that the 1.63 eV peak corresponds to negatively-charged trion luminescence.

3.3 Magnetoluminescence spectroscopy of nearly intrinsic monolayer $MoSe_2$

Figure 3.2a compares polarization-resolved spectra taken for device *D*1 in out-of-plane magnetic fields of 0 T, 6.7 T and -6.7 T and with the back gate grounded. For these data, we excite photoluminescence using equal intensity excitation in σ_+ and σ_- polarization. At zero field, we find no significant dependence of the peak energies or intensities on emission handedness. In comparison, the spectra taken at 6.7 T show splitting between the σ_+ and σ_- emission peaks of about -1.5 meV for both the exciton and trion. The luminescence is also σ_+ polarized: the trion peak has $P_{\text{trion}} = \frac{I_+ - I_-}{I_+ + I_-} = 14\%$, where $I_\pm$ is the peak intensity of the trion in $\sigma_\pm$ detection. For the exciton we measure $P_{\text{exciton}} = 9\%$. The luminescence polarization changes sign with reversal of the magnetic field but not with excitation polarization, showing that it arises from magnetically induced changes in the exciton and trion populations. Figure 3.2b depicts the schematic band-structure of a $MoSe_2$ monolayer, illustrating the direct band gaps at the K_+ and K_- points, with arrows indicating the allowed *A* exciton transitions for $\sigma_\pm$ light. Since the emission handedness is coupled to the exciton valley degree of freedom, the peak splitting and polarization we observe indicate valley degeneracy

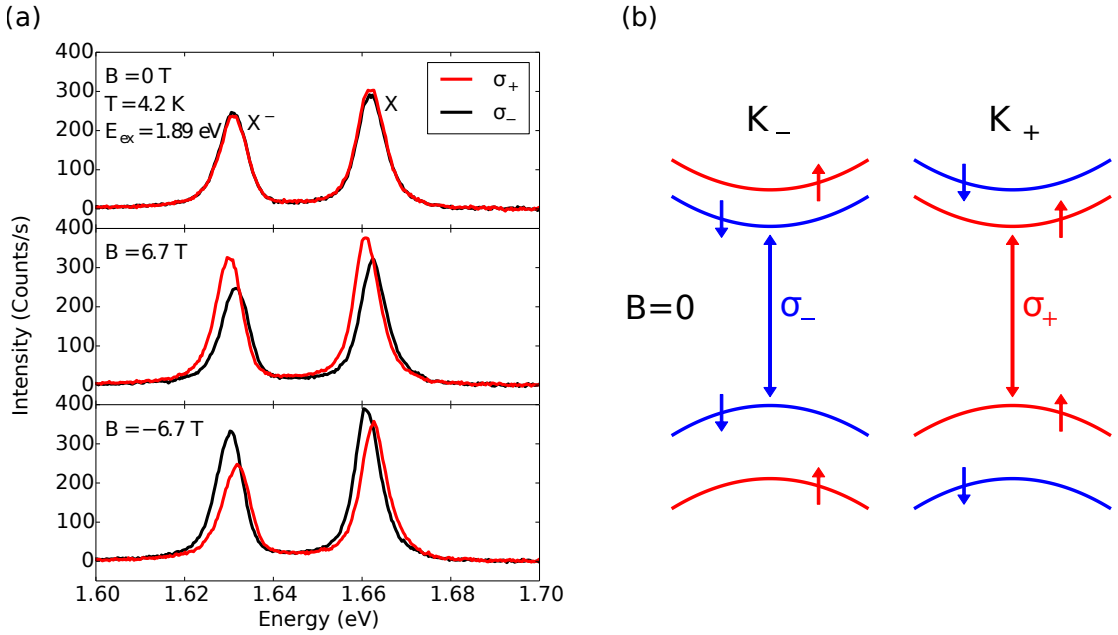

Figure 3.2: **(a)** Polarization-resolved luminescence spectra from monolayer $MoSe_2$ ($D1$) at 4.2 K for σ_+ and σ_- detection, as excited using unpolarized light at 1.89 eV. From top to bottom the panels show spectra taken with 0 T, 6.7 T and -6.7 T out-of-plane magnetic field. Both the polarization and splitting change sign upon reversing the field as shown in the lower panel. **(b)** Schematic band-structure of $MoSe_2$ near the K_+ and K_- points in zero magnetic field, showing the optical selection rules for the A exciton transition studied in this experiment. Within each valley, spin degeneracy is broken at $B = 0$ due to spin-orbit coupling, [30–32, 37, 58]. The arrows denote spin angular momentum up and down for the occupied states.

breaking.

Figure 3.3a shows the valley splitting of the exciton and trion peaks, defined as the difference between peak luminescence energy found with σ_+ and σ_- detection, versus the magnetic field. For each data point the peak positions were extracted via fits to a phenomenological asymmetric Voigt line shape (see Section 3.6.2). The error bars come primarily from the CCD pixel size (about 0.15 nm per pixel). For both the exciton and trion peaks the valley splitting shows a linear magnetic-field dependence with a slope of $-0.22 \pm 0.01 \frac{\text{meV}}{\text{T}}$. Similar re-

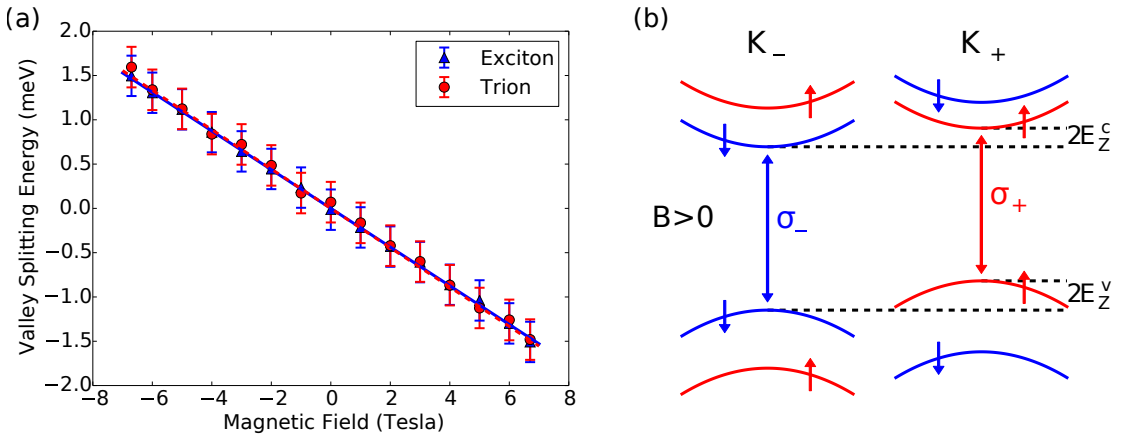

Figure 3.3: **(a)** Difference of peak energies found for σ_+ and σ_- detection plotted versus magnetic field for $D1$. Both the exciton (blue triangles) and trion (red circles) show splitting of $-0.22\pm0.01\,\frac{\text{meV}}{\text{T}}$ found via a linear fit. The fits are plotted as blue solid and red dashed lines for the exciton and trion respectively. **(b)** The schematic bandstructure of $MoSe_2$ in magnetic field showing the Zeeman energy $E_Z^{c(v)}$ for the conduction (valence) band. The exciton Zeeman splitting is $2\left(E_Z^c - E_Z^v\right)$.

sults were found on three separate samples; data from other samples are given in Section 3.6.3.

Valley splitting in magnetic field arises from the intrinsic chirality of Bloch electrons at the K_+ and K_- points. States at the two valley edges are Kramers doublets related by time-reversal symmetry, so that their degeneracy can be broken by breaking time-reversal symmetry. More concretely, Bloch electrons in a given band carry spin and orbital magnetic moments which change sign between valleys [30, 34, 59, 65]. Figure 3.3b schematically shows the energy shifts arising from Zeeman coupling between these moments and the magnetic field; there, we define $2E_Z^{c(v)}$ as the magnetic-field-induced energy difference between the K_+ and K_- valley at the conduction (valence) band edge. Magnetoluminescence spectroscopy probes only the exciton Zeeman energy, which is the difference between conduction and valence band Zeeman energies. In this difference,

the contributions from spin magnetic moments are expected to cancel, leaving only the contributions from orbital magnetic moments.

The measured sign and magnitude of the valley splitting can be understood within a tight-binding picture [66, 67]. In the K_τ valley (letting $\tau = \pm 1$ be the valley quantum number), the valence band arises from hybridization of $d_{x^2-y^2} + \tau i d_{xy}$ orbitals with angular momentum $l_z = 2\tau\hbar$ while the conduction band arises from hybridization of d_{z^2} orbitals with $l_z = 0$ [27, 32, 33, 35]. In the tight-binding limit we, therefore, expect a contribution to the exciton Zeeman energy of $2\left(E^c_{\mathrm{Z,a}} - E^v_{\mathrm{Z,a}}\right) = -4\mu_\mathrm{B}B$ from atomic-scale magnetic moments. The phase winding of Bloch states on the intercellular scale can also add to the orbital magnetic moment [59, 65–68]. For example, in the two-band tight-binding model (the massive Dirac fermion model) the intercellular magnetic moment is equal for the conduction and valence bands with value $-\tau\mu_\mathrm{B}\frac{m_e}{m_\mathrm{eff}}$, where m_e is the free-electron mass, and m_eff is the electron-hole symmetric carrier effective mass [34,59]. Including the spin magnetic moments this gives a total Zeeman splitting of $2E^c_Z = 2\mu_\mathrm{B} + 2\mu_\mathrm{B}\frac{m_e}{m_\mathrm{eff}}$ for the conduction band and $2E^v_Z = 2\mu_\mathrm{B}B + 4\mu_\mathrm{B}B + 2\mu_\mathrm{B}B\frac{m_e}{m_\mathrm{eff}}$ for the valence band, and as a result $2\left(E^c_Z - E^v_Z\right) = -4\mu_\mathrm{B}B$ (i.e. there is no net intercellular contribution). In more general hopping models, the conduction and valence bands can have different intercellular moments giving a net contribution to the exciton magnetic moment [31, 62, 66, 67].

To compare our measurements with theory, we define the exciton valley g-factor $g^\mathrm{vl}_\mathrm{ex}$ as:

$$g^\mathrm{vl}_\mathrm{ex} = \frac{E_+ - E_-}{\mu_\mathrm{B}B} = \frac{2(E^c_Z - E^v_Z)}{\mu_\mathrm{B}B} \tag{3.1}$$

where $E_\pm$ is the measured exciton peak energy in $\sigma_\pm$ detection. Our exciton valley splitting measurements correspond to $g^\mathrm{vl}_\mathrm{ex} = -3.8 \pm 0.2$, consistent with

the value of $g_{ex}^{vl} = -4$ expected from the d-orbital contribution to the exciton magnetic moment. Any deviation of g_{ex}^{vl} from -4 theoretically corresponds to the intercellular contribution to the g-factor. Our results therefore suggest that the intercellular contribution to g_{ex}^{vl} is small in the case of $MoSe_2$. We also expect the trion to have approximately the same splitting as the exciton, evinced by considering the trion as an exciton bound to an additional electron. While the additional electron contributes to the trion magnetic moment, it contributes equally to the final state moment after recombination leaving the transition energy unaffected (as discussed in more detail in Section 3.6.4). This is consistent with the experimental results of Fig. 3.3a for zero applied gate voltage.

We also attempted to calculate the valley g-factor using the multiband $\mathbf{k} \cdot \mathbf{p}$ theory of Refs. [30], since this theory should include the intercellular and atomic contributions in a unified way [68]. The need to discuss these terms separately is an artifact of the lattice models discussed above. The calculation is detailed in Section 3.7 and gives a value for g_{ex}^{vl} similar in magnitude to our experimental results, but with the opposite sign (see Section 3.6.5 for our experimental determination of the sign). Therefore further theoretical work is required to understand the exciton valley splitting within the context of $\mathbf{k} \cdot \mathbf{p}$ theory calculations.

3.4 Magnetoluminescence spectroscopy of monolayer $MoSe_2$ at high carrier densities

We find that the trion valley splitting and the resulting luminescence polarization both show a surprising dependence on an applied back-gate voltage. Polarization-resolved spectra taken with -20 V and 51 V applied to the substrate

are shown in Fig. 4a for device $D2$. Our samples show significant hysteresis assumed to arise from photoionization of trap states [69], and the data in this panel are taken from a downward sweep. Figure 4b shows the trion splitting versus magnetic field for two different gate voltages on a downward sweep, finding $-0.29 \pm 0.02 \frac{\text{meV}}{\text{T}}$ at 40 V and $-0.23 \pm 0.02 \frac{\text{meV}}{\text{T}}$ at 0 V. This gate-voltage dependence of the trion splitting could arise from carrier-density dependence of the band Zeeman energies [59, 62], or other effects resulting from changes in the trion or final state wavefunctions upon increasing the Fermi level [70]. The gate dependence of trion valley splitting has implications for future magneto-optical studies of TMDs, as the intrinsic doping level may vary between samples causing a dispersion of measurement results.

The degree of trion polarization as a function of gate voltage is shown in Fig. 4c. In this dataset, we find a trion polarization that increases from 18% near zero back-gate voltage to over 50% near 40 V. The luminescence polarization in the n-type regime is related to the populations of different trion species via $P_{\text{trion}} = \frac{n_+ - n_-}{n_+ + n_-}$, where $n_\pm$ is the density of negatively-charged trions with their hole in valley $K_\pm$ (i. e. those which emit $\sigma_\pm$ polarized light upon recombination, which we refer to as $K_\pm$ valley trions). The sign of P_{trion} is found to be independent of the excitation polarization and instead follows the sign of the magnetic field, and we, therefore, interpret the magnetic field dependence of the trion polarization as arising from partial relaxation of trions into their lowest energy spin-valley configuration (qualitatively consistent with the dependence of trion polarizaiton on excitation power, see Section 3.6.6). This relaxation is expected to be incomplete as the intervalley scattering time is longer than the recombination time [52]. In Section 3.6.4, we calculate the trion polarization within a simple rate-equation model and show that the observed P_{trion} implies a ratio of

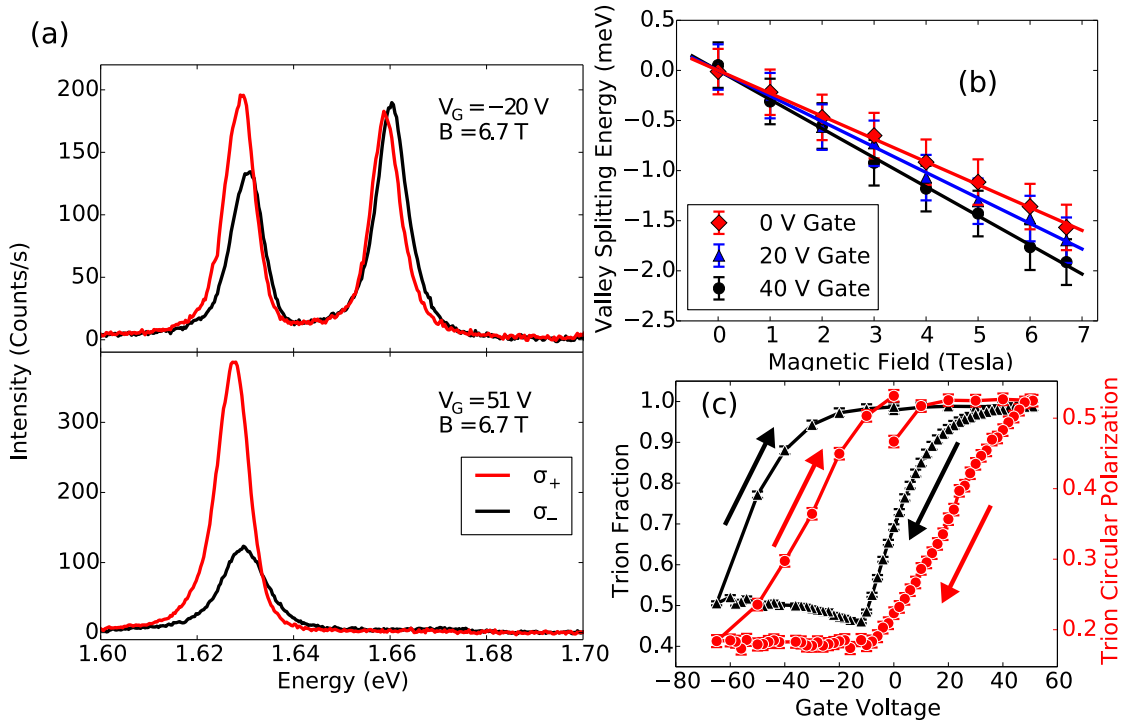

Figure 3.4: **(a)** Polarization-resolved luminescence spectra from $D2$ at 4.2K and 6.7 T for σ_+ and σ_- detection, excited with σ_- light at 1.89 eV. From top to bottom the panels show spectra taken with -20 V and 51 V gate voltage applied to the substrate. **(b)** Trion valley splitting versus magnetic field for selected gate voltages, showing an decrease in slope with gate voltage. **(c)** Circular polarization of the trion peak $\frac{I_+ - I_-}{I_+ + I_-}$ versus gate voltage at 6.7 T (red circles), showing an increase to over 50% as gate voltage is increased. For comparison, we also plot the trion fraction $\frac{I_{\text{trion}}}{I_{\text{trion}} + I_{\text{exciton}}}$ (black triangles).

the recombination time to the intervalley scattering time of ~ 0.2 at low carrier density. This is about an order of magnitude larger than the value found in time-resolved measurements for WSe_2 at zero magnetic field [71]; however, the time-resolved measurements used resonant excitation which is expected to lead to reduced intervalley scattering compared to the off-resonant excitation we use. Trions can scatter between valleys via spin-flip intervalley scattering of their hole, and if this is the dominant scattering mechanism our results imply that the hole intervalley scattering rate increases monotonically with carrier

density. This is consistent with the Bir-Aronov-Pikus mechanism for intervalley scattering of holes via their exchange interaction with the conduction electrons [52, 72]. The data in Fig. 3.4c were taken with σ_- excitation, but similar results were found using unpolarized excitation (see Section 3.6.3).

3.5 Conclusion

In summary, we have presented measurements of polarization-resolved luminescence spectra for $MoSe_2$ at 4.2 K in magnetic fields up to 6.7 T, demonstrating valley degeneracy breaking. We have measured a splitting of $-0.22 \pm 0.01 \frac{\text{meV}}{\text{T}}$ between exciton peaks in σ_+- and σ_--polarized emission spectra. This value is consistent with a simple tight-binding picture of the $MoSe_2$ bandstructure. We have also observed gate dependence of the trion valley splitting and polarization. Even with off-resonant unpolarized excitation we were able to achieve a trion circular polarization of about 50% by gating the sample in 6.7 T magnetic field. Application of magnetic and electric fields can therefore provide an effective strategy for manipulating the valley degree of freedom in monolayer TMDs.

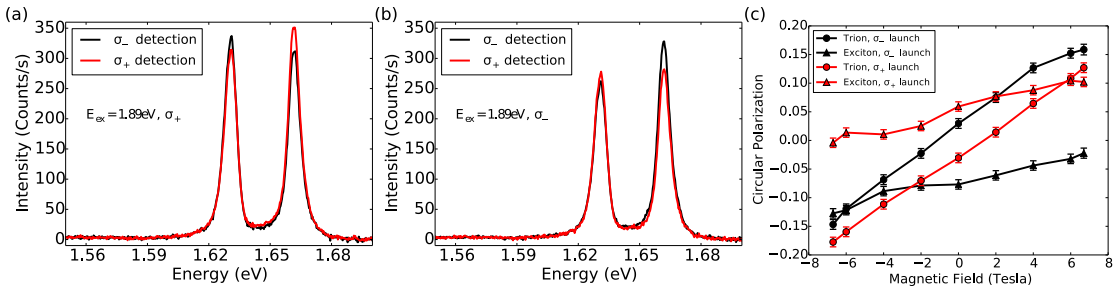

Figure 3.5: **(a)** Polarization-resolved spectra from $D1$ taken at zero magnetic field and with σ_+ excitation, showing σ_+ polarization of exciton luminescence. **(b)** Polarization-resolved spectra from $D1$ taken at zero magnetic field and with σ_- excitation. **(c)** Luminescence polarization versus magnetic field with σ_+ (red) and σ_- (black) excitation for excitons (triangles) and trions (circles).

3.6 Supplemental information

3.6.1 Dependence of luminescence handedness on excitation handedness

Figures 3.5a and 3.5b show polarization-resolved luminescence spectra for device $D1$ at $T = 4.2$ K and $B = 0$ T taken with σ_+ and σ_- polarized excitation respectively. We observe some preservation of the incident polarization even with our 1.89 eV excitation. We find $P_{\text{exciton}} = \frac{I_+ - I_-}{I_+ + I_-} = 6\%$ for σ_+ excitation and $P_{\text{exciton}} = -8\%$ for σ_- excitation indicating 7% average co-polarization of exciton luminescence with the excitation laser. On the other hand, we see counter polarization of 3% for the trion luminescence. We also studied the dependence of the field-induced polarization on excitation handedness: as shown in Fig. 3.5c switching the excitation polarization seemingly adds a constant offset. The small polarization preservation we observe is consistent with studies of polarization preservation in MoS_2 using off-resonant excitation [52, 54].

3.6.2 Background subtraction and fitting

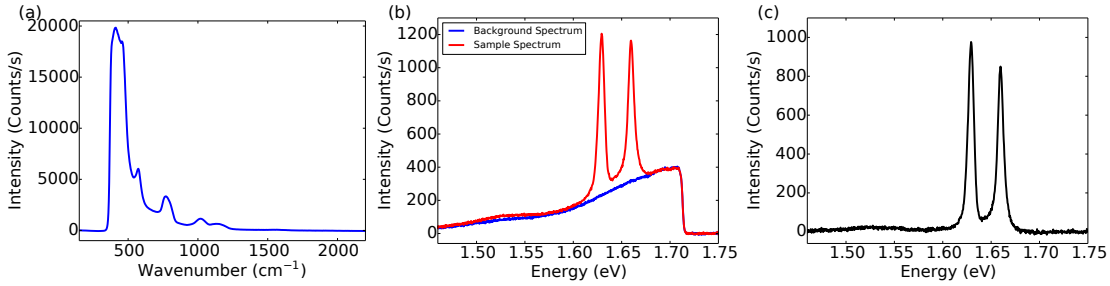

Figure 3.6: **(a)** Fiber background spectrum excited with 705 nm laser diode, showing fused silica Raman peaks. **(b)** Comparison of spectra taken with 656 nm excitation laser on the sample (red) and on a nearby region of bare substrate (blue). **(c)** The result of subtracting the two curves in **(b)**.

Raman scattering of the excitation laser in the fiber presents a significant background in our experiment, as has been reported elsewhere [46,73]. A spectrum of fiber Raman excited with 705 nm light is plotted in Fig. 3.6a, showing fused silica Raman peaks [73]. Since we excite with 656 nm light we encounter only the tail of this signal during measurements of $MoSe_2$ luminescence. To account for this background, we take additional spectra with the excitation laser spot on silicon; the background spectrum is then subtracted from the signal after carrying out a dark-count subtraction on both spectra. This is shown in Figs. 3.6b and 3.6c. In practice, we rescale the background to match the signal spectrum away from the luminescence peaks, to account for laser-power fluctuations and to allow a single background spectrum to be used multiple times. In Figs. 3.6b and 3.6c we have used the data without rescaling to prove that fiber Raman entirely accounts for the background.

In the Sections 3.3 and 3.4 we report values for the peak polarization and energy as a function of magnetic field and gating. As described there, we use fits to an asymmetric Voigt profile to extract the peak properties. The Voigt

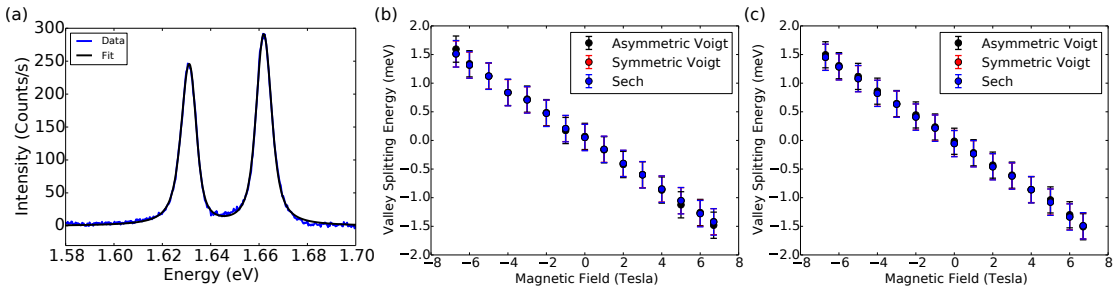

Figure 3.7: **(a)** Comparison of sample luminescence spectrum (blue) and fit used to locate peak energy (black). The spectrum is fit to the sum of two asymmetric Voigt profiles, with $\chi^2 \approx 3$. **(b)** Trion valley splitting as extracted with fits to asymmetric Voigt (black), symmetric Voigt (red), and hyperbolic secant (blue). **(c)** Exciton valley splitting as extracted with fits to asymmetric Voigt (black), symmetric Voigt (red), and hyperbolic secant (blue). Valley splittings from asymmetric Voigt fits are presented in Fig. 3.3 of the main text.

function is defined as:

$$\frac{1}{\sigma\sqrt{2\pi}}\,\mathrm{Re}\left\{\exp\left[-\left(\frac{\delta\omega+i\gamma}{\sqrt{2}\sigma}\right)^2\right]\mathrm{erfc}\left[-i\left(\frac{\delta\omega+i\gamma}{\sqrt{2}\sigma}\right)\right]\right\}, \tag{3.2}$$

where $\delta\omega$ is the detuning and γ and σ are fit parameters characterizing the peak width. As written, the function describes the convolution of a Lorentzian with width γ and a Gaussian with width σ; to make the line shape asymmetric we allow γ to take different values for positive and negative detuning. A typical spectrum with fit is plotted in Fig. 3.7a; in this case the χ^2 was about 3. We also tried fitting to other functions, such as a hyperbolic secant and a symmetric Voigt profile. There was no difference in the valley splitting within our error bars. A comparison of splitting energies between symmetric Voigt, hyperbolic secant and asymmetric Voigt is shown in Figs. 3.7b and 3.7c.

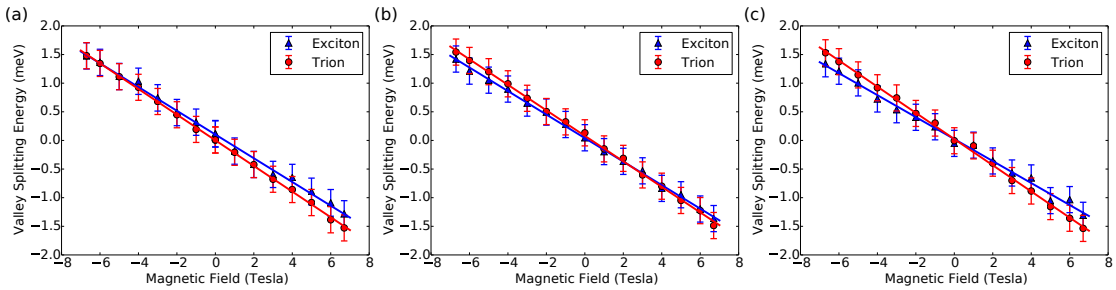

Figure 3.8: **(a)** Valley splitting data for $D1$, as defined in the main text. **(b)** Valley splitting data taken near the center of $D3$. **(c)** Valley splitting data taken near one edge of $D3$.

3.6.3 Comparison of data from multiple devices

We measured the valley splitting versus magnetic field with the back-gate grounded for three different devices. All data were taken at 4.2 K and with 1.89 eV excitation. Valley splitting data not shown in Sections 3.3 or 3.4 are given in Fig. 3.8; $D1$ and $D2$ are defined in Section 3.2 and the additional device is called $D3$. For $D3$, we took data at two different positions on the flake. We have also provided Table 3.4 showing the slopes extracted from linear fits to this data. The standard deviation across datasets was 0.004 $\frac{\text{meV}}{\text{T}}$ for the trion splitting and 0.01 $\frac{\text{meV}}{\text{T}}$ for the exciton splitting. For one of the locations on $D3$, there was a significant discrepancy between the exciton and trion splitting.

Sample	Exciton Splitting ($\frac{\text{meV}}{\text{T}}$)	Trion Splitting ($\frac{\text{meV}}{\text{T}}$)
$D1$	-0.22	-0.22
$D2$	-0.21	-0.22
$D3$ location 1	-0.21	-0.22
$D3$ location 2	-0.19	-0.23

Table 3.1: Valley splitting for multiple devices in $\frac{\text{meV}}{\text{T}}$, defined as the difference of luminescence peak energies between σ_+ and σ_- polarized light. The error for all values is $\pm 0.01 \frac{\text{meV}}{\text{T}}$.

We also measured the gate dependence of valley splitting and polarization

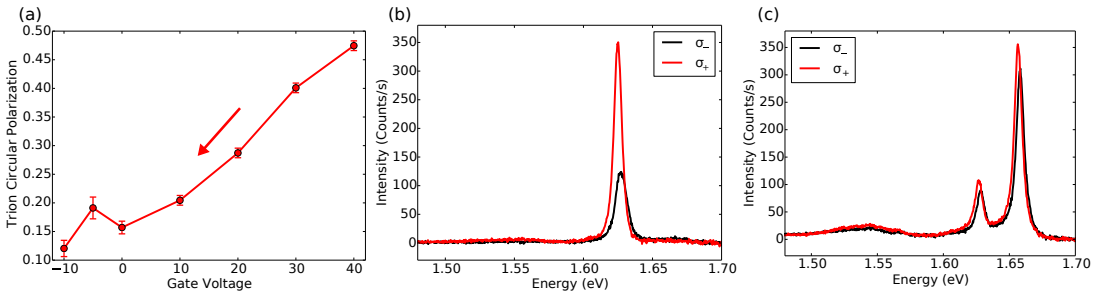

Figure 3.9: **(a)** Trion peak polarization versus gate voltage at $B = 6.7$ T for $D4$ taken on a downward sweep and using 11 μW excitation with equal intensity in σ_+ and σ_- light. **(b)** Polarization-resolved luminescence spectrum of $D4$ taken at 6.7 T magnetic field and 40 V back-gate voltage. **(c)** Polarization-resolved luminescence spectrum of $D4$ taken at 6.7 T magnetic field and -20 V back-gate voltage. The trion polarization is significantly reduced compared to the 40 V spectrum.

on two devices: $D2$ and another device not previously defined, $D4$. The gate dependence of luminescence from $D4$ is shown in Fig. 3.9. As shown in Fig. 3.9a, for $D4$ the trion polarization increases from about 10% to over 45% as the electron density is increased. For the data in Fig. 3.9 we used excitation light with equal intensity in σ_+ and σ_- polarization, and about 11 μW excitation power.

3.6.4 Further discussion of the trion luminescence

Figure 3.10 shows the three possible negatively-charged trion spin-valley configurations which emit σ_+ polarization light on recombination (upper panels) and the corresponding final states after recombination (lower panels). These are the trion species defined as K_+ valley trions. There are also three more trion configurations not shown in Fig. 3.10 (the K_- valley trions) which are related to the configurations shown by time-reversal symmetry, and which emit σ_- light on recombination. In total there are six trion configurations expected to have

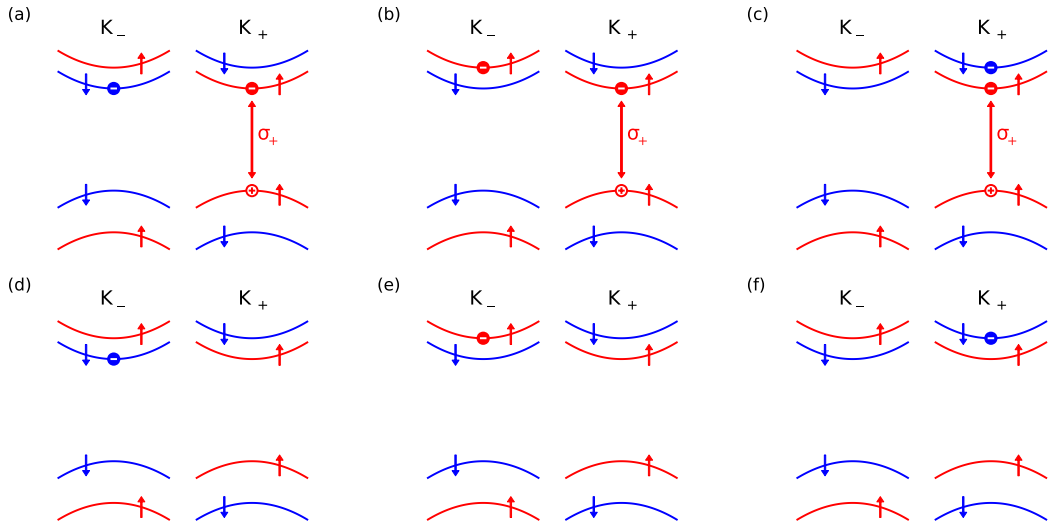

Figure 3.10: Here we show the three possible trion spin-valley configurations which emit σ_+ polarized light on recombination (panels **(a)-(c)**) and the corresponding final states after recombination (panels **(d)-(f)**). In these schematic drawings, the full circles represent the two electrons in the trion, and the open circle represents the hole. We have arranged the panels so that the final state is below the initial state. The configurations shown here are the complete set of trion configurations emitting σ_+ light, but there are three more which emit σ_- light and are related to these via time-reversal symmetry. For the gate-voltage regime considered in our experiment, we expect that photoluminescence primarily arises from recombination of the trion species in panel **(a)** and its time-reversed partner.

approximately the same binding energy, although the electron-hole exchange interaction is predicted to increase the energy of trions with parallel electron spins by about 6 meV [74]. Any trion configurations in which the two electrons have the same quantum numbers (spin and valley) have not been included in this accounting since they are not expected to be bound due to Pauli blocking. For $MoSe_2$ at low carrier density, only the lowest conduction bands will be occupied at 4.2 K since the conduction band spin-splitting is predicted to be about 20 meV [30–32]. As a result, the trion species in panel **(a)** is expected to be dominant at low carrier density. Fig. 3.4 shows that the conduction band edge for our

samples is around −12 V on a downsweep and therefore we gate into the conduction band by at most $\frac{C\Delta V}{eA}/\frac{m_c}{\pi\hbar^2} \approx 20$ meV at our highest gate voltages (using $C \approx 1.2 \times 10^{-8}$ F/cm^{-1} as the back-gate capacitance per unit area). The presence of interface traps means this is an overestimate and we expect that the observed luminescence signal primarily arises from recombination of the panel **(a)** trion (and the time reversed version emitting σ_- light) at all gate voltages studied in this work.

In a magnetic field, the Zeeman energy of the trion can be approximated as the sum of the Zeeman energies of its constituent electrons and hole (the hole Zeeman energy being minus that of the relevant valence band). For example, the photon emitted when the panel **(a)** trion recombines has energy: $E_{\text{initial}} - E_{\text{final}} = \epsilon_c + E_Z^c - \epsilon_v - E_Z^v + \epsilon_c - E_Z^c - E_B - \left(\epsilon_c - E_Z^c\right) = \epsilon_c - \epsilon_v - E_B + E_Z^c - E_Z^v = \hbar\omega + E_Z^c - E_Z^v$, where E_B is the sum of the exciton and trion binding energies, and $\hbar\omega$ is the trion emission energy for zero magnetic field. The trion valley splitting is then $2(E_Z^c - E_Z^v)$ and equal to the exciton valley splitting. Similar calculations give the same results for panels **(b)** and **(c)**.

To estimate the gate dependence of the trion polarization we use a simple rate-equation model. In this model we assume that, for $B > 0$, the conversion rate of K_+ valley trions into K_- valley trions is suppressed by a Boltzmann factor of $e^{-2\beta E_Z^v}$ compared to the time-reversed process [75], where $\beta = \frac{1}{k_B T}$ with T the effective temperature of the trion population. The argument of the Boltzmann factor is determined by the energy barrier for switching from the trion species in panel **(a)**, with its hole in K_+ valley, to its time reversed parter with a hole in K_- valley. We will also assume that, due to our off-resonant excitation, the formation rate, Q, of K_+ and K_- trions is roughly equal. The resulting rate equation

is:

$$\begin{cases} \frac{dn_+}{dt} = Q - n_+/\tau_{\mathrm{R}} + n_-/\tau_{\mathrm{vl}} - n_+ e^{-2\beta E_Z^v}/\tau_{\mathrm{vl}} \\ \frac{dn_-}{dt} = Q - n_-/\tau_{\mathrm{R}} - n_-/\tau_{\mathrm{vl}} + n_- e^{-2\beta E_Z^v}/\tau_{\mathrm{vl}} \end{cases} \tag{3.3}$$

where $n_\pm$ is the trion population in the $K_\pm$ valley, $1/\tau_{\mathrm{R}}$ is the trion recombination rate, and $1/\tau_{\mathrm{vl}}$ is the rate for K_- to K_+ intervalley scattering of the trion. In this simple model we have also ignored the possibility that the recombination rate may depend on the valley. The steady state solution is:

$$P_{\mathrm{trion}} = \frac{n_+ - n_-}{n_+ + n_-} = \frac{\frac{\tau_{\mathrm{R}}}{\tau_{\mathrm{vl}}}\left(1 - e^{-2\beta E_Z^v}\right)}{1 + \frac{\tau_{\mathrm{R}}}{\tau_{\mathrm{vl}}}\left(1 + e^{-2\beta E_Z^v}\right)} \approx \frac{\frac{\tau_{\mathrm{R}}}{\tau_{\mathrm{vl}}}}{1 + \frac{\tau_{\mathrm{R}}}{\tau_{\mathrm{vl}}}} \tag{3.4}$$

where the second equality is obtained by ignoring the Boltzmann factor $e^{-2\beta E_Z^v} \approx 0.0004$ at 4.2 K and 6.7 T. At low gate voltages we find $P_{\mathrm{trion}} \approx 0.18$ for the data in Fig. 3.4c or $\frac{\tau_{\mathrm{R}}}{\tau_{\mathrm{vl}}} \approx 0.2$. This is about an order of magnitude larger than the value of $\frac{\tau_{\mathrm{R}}}{\tau_{\mathrm{vl}}} \approx 0.03$ found by Ref. [71]; however, their value was obtained in significantly different experimental conditions since they studied WSe_2 samples using resonant excitation and at zero magnetic field. In Fig. 3.11a, we plot the intervalley scattering rate normalized to the recombination rate $\frac{\tau_{\mathrm{R}}}{\tau_{\mathrm{vl}}} \approx |P_{\mathrm{trion}}|/\left(1 - |P_{\mathrm{trion}}|\right)$ versus gate voltage. The data shows a linear increase in intervalley scattering with carrier density, consistent with the Bir-Aronov-Pikus mechanism for intervalley hole scattering by the background conduction electrons [52,72]. As discussed in Section 3.6.6, we also observe a decrease in the trion polarization with increasing excitation power. This is qualitatively consistent with the rate-equation model assuming that the effective temperature of the trion population increases with excitation power.

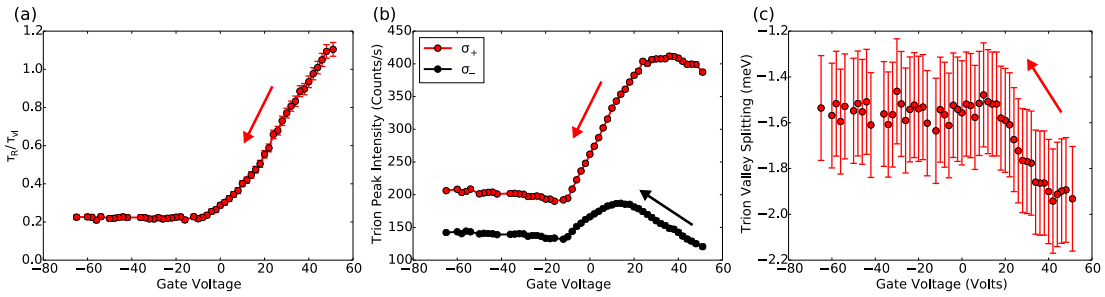

Figure 3.11: **(a)** Gate voltage dependence of $\frac{\tau_R}{\tau_{vl}}$ as defined in the text. This is the same dataset as used for Fig. 3.4c of the main text: it was taken for sample $D2$ at 4.2 K and 6.7 T magnetic field, using an excitation power of about 12.5 μW and σ_- excitation. The arrow represents the direction of the gate-voltage sweep. **(b)** Peak intensities of trion luminescence in σ_+ (red) and σ_- (black) detection versus gate voltage at 4.2 K and 6.7 T, taken for sample $D2$. **(c)** Trion valley splitting versus gate voltage at 4.2 K and 6.7 T, taken for sample $D2$.

3.6.5 Experimental determination of the sign of the valley splitting

In Eq. 3.1, we define the valley splitting as the difference of peak luminescence energies between σ_+ and σ_- polarized emission. Furthermore, $\sigma_\pm$ polarization is defined as the circular polarization which carries $\pm\hbar$ angular momentum per photon along the field direction for $B > 0$. Equivalently, σ_+ (σ_-) polarized light can be defined as light with an electric field vector rotating in a right (left) handed manner in time around the positive B axis. The convention for $B > 0$ is defined in Fig. 3.1. To determine the sign of the splitting, we used two methods.

First, we determined the rotational settings of the detection polarizer corresponding to different circular polarizations of emission. To do this, we launched circularly-polarized laser light into the cryostat objective lens from the sample space, and found the settings of the detection polarizer which maximized the resulting signal. The circularly-polarized light was generated by sending lin-

early polarized light through a $\lambda/4$ plate with the light polarized at 45° to the waveplate axes. Given knowledge of the waveplate axes and their orientation relative to the light polarization, the handedness of circularly-polarized light produced in this fashion can be determined. We also checked the assignment of the waveplate fast and slow axes by shining circularly-polarized light of a known handedness through the waveplate and analyzing the resulting linear polarization. For this test, the circularly-polarized light was generated using two N-BK7 prisms in a Fresnel rhomb geometry, so that the resulting handedness could be determined from the Fresnel equations. We determined the field direction using a calibrated Hall probe. The considerations above determine the rotational settings of the detection polarizer corresponding to detection of σ_+ and σ_- emission.

We also compared the valley splitting for $MoSe_2$ to magnetoluminescence measurements for a (110) cut, undoped, *p*-type CdTe substrate (from MTI Corporation). For *p*-type CdTe, the acceptor-bound exciton luminescence shows a four-fold splitting under magnetic field applied in the Faraday geometry. The optical selection rules lead to circular polarization of these peaks, so that two are σ_+ polarized and two are σ_- polarized. With the detection polarization determined as discussed above, we find peak splitting and selection rules for CdTe in agreement with those found by Refs. [49, 50, 76]. In particular, given that the lowest energy acceptor-bound exciton luminescence peak for CdTe is σ_- polarized (for $B > 0$), we know that the lowest energy $MoSe_2$ peak indeed originates from σ_+ polarized luminescence (for $B > 0$).

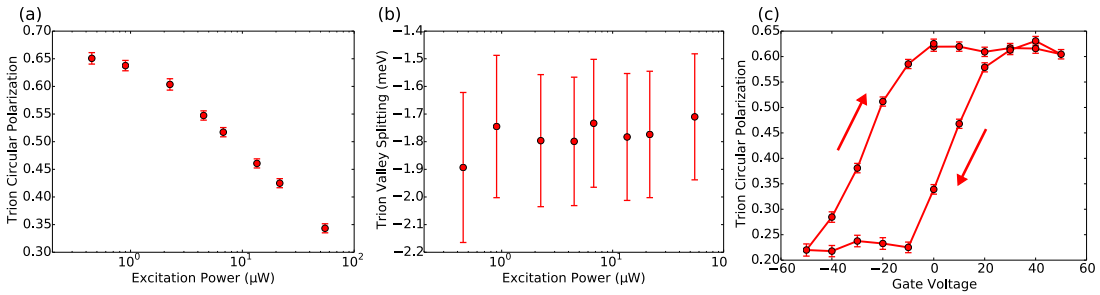

Figure 3.12: **a)** Trion peak circular polarization versus power in the n-type regime, for B = 6.7 T, and excited with σ_- polarized light. **b)** Trion valley splitting versus power in the n-type regime and for B = 6.7 T. **c)** Trion peak circular polarization versus gate voltage, taken at 6.7 T and using about 1.1 μW excitation power.

3.6.6 Power dependence of trion polarization

As shown in Fig. 3.12a, the trion luminescence polarization increases to about 65% circularly-polarized as the power is reduced for B = 6.7 T, T = 4.2 K, and in the regime of high electron density. On the other hand, we see no power dependence of the trion peak splitting (see Fig. 3.12b). Within our rate equation model, the power dependence of trion polarization arises from changes in the lattice temperature, or the effective temperature of the trion population which may not be equilibrium with the lattice. A thermometer mounted on the chip holder shows < 50 mK sample heating under more than 200 μW excitation, suggesting that the lattice heating is small. Figure 3.12c shows the gate dependence of trion polarization at 6.7 T and 4.2 K, with an excitation power of about 1.1 μW; the fractional increase in the trion polarization with gate voltage is similar to data shown in Section 3.4 (taken with about 11 μW excitation).

3.7 Calculating the exciton's magnetic moment

Calculating the orbital magnetic moment of Bloch electrons is an old, and surprisingly subtle problem [68,77,78]. The mathematical difficulties are twofold, i) the angular momentum operator $\mathbf{L} = \mathbf{r} \times \mathbf{p}$ is ill-defined (non-Hermitian) for an infinite crystal, and ii) the effect of magnetic field on the extended wavefunctions (Landau quantization) creates linear energy shifts that cannot be calculated perturbatively. The overall effect is an energy shift more complicated than $-\frac{e}{2m}\langle \mathbf{L} \cdot \mathbf{B} \rangle$. Note also the two concepts of magnet moment here: the latent magnetic moment when no magnetic field is applied, and the total magnetic moment including the diamagnetic reaction to the applied field, which is $\mathbf{m} = -\frac{dE}{d\mathbf{B}}$. The first type of moment turns out to be relevant for excitons, but we'll get to that.

Despite the mathematical weirdnesses, the problem can be solved exactly: the solution is a generalization of the $\mathbf{k} \cdot \mathbf{p}$ perturbation theory used to calculate band effective masses. A great explanation is found in Ref. [68]. There we can find an effective Hamiltonian for Bloch electrons in a magnetic field, which I have specialized for the K_τ valley of $MoSe_2$, ignoring spin-orbit coupling:

$$H_{\tau,b} = \epsilon_b + \frac{1}{2m_b}\left(\hbar\mathbf{k} + e\mathbf{A}(\mathbf{r})\right)^2 + 2\mu_B B s_z - \tau\mu_b B, \tag{3.5}$$

where b is the band index, ϵ_b is the band-edge energy, and $\mathbf{k}$ is the crystal momentum measured from the K_τ-point. I have also assumed the magnetic field $\mathbf{B}$ points in the $\hat{z}$ direction, and $\mathbf{A}$ is the corresponding vector potential. The eigenstates of this Hamiltonian give envelope functions modulating the underlying Bloch states. I can't explain this better than Ref. [68], so check it out. Aside from the free-electron Zeeman energy $2\mu_B B s_z$, there is also a linear-in-field energy

splitting from $-\tau\mu_b B$. This is what I previously called the "latent" magnetic moment, and will henceforth call the band magnetic moment. The kinetic energy part of $H_{\tau,b}$ will also give linear energy shifts in a magnetic field, $E_n = \frac{\hbar eB}{m_b}(n+1/2)$, due to Landau quantization. But that effect depends on the envelope wavefunction and will be different for the exciton. I'll discuss this at the end of the section, but basically so long as the Landau level spacing is much smaller than the exciton binding energy, the exciton wavefunction is not too perturbed by the applied magnetic field and the increase of the kinetic energy is quadratic in B. I will also assume the spread of the exciton wavefunction in $\mathbf{k}$-space is small enough to ignore higher order corrections to Eq. 3.5. This requires that the exciton binding energy is much less than total band width and interband spacings. Under these assumptions, the magnetic moment of excitons at the K_+ point will be the difference between the conduction band and valence band magnetic moments, $\mu_c - \mu_v$. The magnetic moment changes sign between valleys, so that the valley g-factor defined in Eq. 3.1 is $-2\frac{\mu_c-\mu_v}{\mu_\mathbf{B}}$

The derivation of Eq. 3.5 leads to a formula for μ_b [30, 34, 68, 77–79]:

$$\mu_b = -\frac{\mu_\mathrm{B}}{2m_e}\sum_{a\neq b}\frac{|P_+^{ba}|^2 - |P_-^{ba}|^2}{\epsilon_b - \epsilon_a} \tag{3.6}$$

where m_e is the free electron mass, μ_B is the Bohr magneton, and $P_\pm^{ba} = \langle b|\, p_x \pm ip_y\, |a\rangle$ is proportional to the optical matrix element for $\sigma_\pm$ light between Bloch states $|a\rangle$ and $|b\rangle$. This is the relationship between the optical matrix elements and angular momentum I promised way back in Section 1.2.2. The formula above gives the z component of the magnetic moment, assuming $\{x, y, z\}$ form a right-handed coordinate system. As discussed in early papers on Bloch electrons in magnetic fields [68, 77], this formula includes both contributions from current circulation within a unit cell (the atomic contribution to the magnetic moment) and current circulation on the scale of multiple unit cells (the inter-

cellular contribution to the magnetic moment). Despite all the hand-wringing about ill-defined operators, you can get the same result if you blindly calculate $-\frac{e}{2m}\langle \mathbf{L} \rangle$ and ignore the infinities that pop up in intermediate steps [80]. This corresponds to creating a lattice periodic version of $\mathbf{L}$ [68].

Anyways, to calculate the exciton magnetic moment, we only need to figure out $P_{\pm}^{ba}$. These are closely related to the $\mathbf{k} \cdot \mathbf{p}$ theory matrix elements, which are the matrix elements of $H_{\mathbf{k}\cdot\mathbf{p}} = \frac{\hbar}{2m_e}(k_+ p_- + k_- p_+)$ between the Bloch states. The idea of Ref. [30] is determine $P_{\pm}^{ba}$ by fitting $\mathbf{k} \cdot \mathbf{p}$ theory calculations to the DFT band structure. In Table V of Ref. [30], the authors give the $\mathbf{k} \cdot \mathbf{p}$ matrix elements within their theory. The resulting valley Zeeman energies are:

$$E_Z^c/\mu_B = \frac{2m_e B|\gamma_3/\hbar|^2}{\epsilon_c - \epsilon_v} - \frac{2m_e B|\gamma_5/\hbar|^2}{\epsilon_c - \epsilon_{v-3}} - \frac{2m_e B|\gamma_6/\hbar|^2}{\epsilon_c - \epsilon_{c+2}} \tag{3.7}$$

in the conduction band and

$$E_Z^v/\mu_B = -\frac{2m_e B|\gamma_3/\hbar|^2}{\epsilon_v - \epsilon_c} + \frac{2m_e B|\gamma_2/\hbar|^2}{\epsilon_v - \epsilon_{v-3}} + \frac{2m_e B|\gamma_4/\hbar|^2}{\epsilon_v - \epsilon_{c+2}} \tag{3.8}$$

in the valence band, where ϵ_{c+2} is the energy of the second band above the conduction band and ϵ_{v-3} is the energy of the third band below the valence band. Here the parameters γ_i are proportional to the non-zero $P_{\pm}^{ba}$ elements. In our case, the precise values of these parameters are not important, as we will focus on the relationship between the effective masses and valley splitting that can be derived using the $\mathbf{k} \cdot \mathbf{p}$ approach. The $\mathbf{k} \cdot \mathbf{p}$ theory effective masses can be written in terms of the γ_i similar to the Zeeman splitting (see Eq. B6 of Ref. [30]). Some simple algebra then gives:

$$g_{\text{ex}}^{\text{vl}} = \frac{2(E_Z^c - E_Z^v)}{\mu_B} = 4 - 2\left(\frac{m_e}{m_c} - \frac{m_e}{|m_v|}\right) \tag{3.9}$$

where $m_{c(v)}$ is the effective mass of the conduction (valence) band. As long as the effective masses for conduction and valence band are approximately equal, the

valley splitting calculated this way will be close to $g_{\text{ex}}^{\text{vl}} = 4$ and have the opposite sign to our measurements. For example, taking $m_c = 0.49m_e$ and $|m_v| = 0.59m_e$ (these values are from [81]) gives $g_{\text{ex}}^{\text{vl}} = 3.3$.

Where did this calculation go wrong? Perhaps the large exciton binding energy (0.4 – 0.6 eV) modifies the exciton moment beyond the difference of the band moments, due to the large spread of the exciton wavefunction in **k**-space. I think recent experiments rule this possibility out. In Ref. [82], the authors report beautiful polarization resolved reflectivity measurements for monolayer WSe_2 at carrier densities up to 10^{13} cm^{-1} and in magnetic fields up to 9 T. At these carrier densities, the discrete exciton and trion resonances are gone, leaving a series of low-energy resonances from inter-Landau-level transitions. The electron-hole interaction is mostly screened, yet they find $-2\frac{\mu_c - \mu_v}{\mu_{\mathbf{B}}} = -4.1 \pm 0.3$. They can also measure the Landau level spectrum of the conduction band, allowing unambiguous identification of the K_+ (their K' or l polarization) and K_- (their K or r polarization) points from the valley dependence of this spectrum. This gives strong evidence that the we have correctly determined the sign of the exciton valley splitting in our work. Other groups have carried out systematic comparisons of optical spectra between MoS_2 and WS_2 [83], and $MoSe_2$ and WSe_2 [80]. The results is always a exciton splitting of $g_{\text{ex}}^{\text{vl}} \approx -4$. Remarkable.

Ref. [80] also explored the discrepancy between $\mathbf{k} \cdot \mathbf{p}$ theory and experiment. They suggest the problem could be "remote bands" not included in the $\mathbf{k} \cdot \mathbf{p}$ calculations. A recent e-print [84] expands on this suggestion. Their method is to take a tight-binding Hamiltonian including 11 atomic orbitals, and then expand it around the $\mathbf{K}_\pm$ points (to quadratic order in **k**). They take tight binding parameters from other papers, which in turn got them from fits to DFT calculations.

The resulting Hamiltonian looks a lot like a $\mathbf{k}\cdot\mathbf{p}$ Hamiltonian, so you can read off the $\mathbf{k}\cdot\mathbf{p}$ matrix elements. Unlike the $\mathbf{k}\cdot\mathbf{p}$ theory of Ref. [30] there are *remote band* contributions to the effective mass. Helpfully, such contributions only change the mass and not the band magnetic moment, so you kind of get another degree of freedom to match the experimental inputs. Depending on the tight-binding parameter set, they calculate $g_{\mathrm{ex}}^{\mathrm{vl}}$ in the range -3.82 to 0.65 for MoS_2. The extreme value $g_{\mathrm{ex}}^{\mathrm{vl}} = -3.82$ actually agrees with our results. Hopefully, the experimentally determined g-factors can help produce simple and accurate effective models of TMD electronic states.

In our original paper, we used an ad hoc method to calculate the exciton magnetic moment starting from a hopping Hamiltonian. Other concurrent papers did the same [66,67]. Hopping models neglect the atomic-scale structure of the wave function, and therefore we introduced the d-orbital magnetic moment by hand. This gives a contribution to the band Zeeman energies of $E_{\mathrm{Z,a}}^{c} = 0$ and $E_{\mathrm{Z,a}}^{v} = 2\mu_{\mathrm{B}}$. Aside from this contribution, there is the magnetic moment due to phase winding of the Bloch states on the intercellular scale. This quantity can be calculated by using the Bloch electron magnetic moment formula, Eq. 3.6, on the hopping model. Ref. [27] originally proposed a hopping model based on hybridization of d-orbitals at different Mo lattice sites:

$$H = \begin{pmatrix} \epsilon_c & \tau\gamma_3 q_{-\tau} \\ \tau\gamma_3^* q_{\tau} & \epsilon_v \end{pmatrix} \tag{3.10}$$

written in the basis of band-edge Bloch functions $\{|c\rangle, |v\rangle\}$. The resulting value for the intercellular Zeeman energy is $E_{\mathrm{Z,ic}}^{c(v)} = \mu_{\mathrm{B}} \frac{2m_e B|\gamma_3/\hbar|^2}{\epsilon_c - \epsilon_v}$. Here we have used $\langle c|p_+|v\rangle = 2m_e\gamma_3/\hbar$. We note that $\frac{\hbar^2}{2m_c} = \frac{|\gamma_3|^2}{\epsilon_c - \epsilon_v}$ for this model so that the Zeeman energy is simply $\mu_{\mathrm{B}} B \frac{m_e}{m_c}$. In a given valley this contribution shifts the energy levels in the conduction and valence bands in the same way, and therefore does

not contribute to the exciton valley splitting. The total exciton valley splitting for this model is then $2(E^c_Z - E^v_Z) = 2(E^c_{Z,a} - E^v_{Z,a}) + 2(E^c_{Z,ic} - E^v_{Z,ic}) = -4\mu_B$. This approach has the merit of explaining the robust value $g^{vl}_{ex} \approx -4$.

Finally, I will derive the effective Hamiltonian for excitons in a magnetic field, justifying my assertion that the exciton magnetic moment is $\mu_c - \mu_v$. The exciton Hamiltonian is found by subtracting the conduction and valence band dispersions and adding the electron-hole Coulomb interaction V:

$$\begin{aligned} H_{ex} &= H_c\left(-i\hbar\nabla_e, \mathbf{r}_e\right) - H_v\left(i\hbar\nabla_h, \mathbf{r}_h\right) + V\left(|\mathbf{r}_e - \mathbf{r}_h|\right) \\ &= \frac{\hbar^2}{2m_c}\left(-i\hbar\nabla_e + e\mathbf{A}(\mathbf{r_e})\right)^2 - \frac{\hbar^2}{2m_v}\left(-i\hbar\nabla_h - e\mathbf{A}(\mathbf{r_h})\right)^2 + V\left(|\mathbf{r}_e - \mathbf{r}_h|\right) - (\mu_c - \mu_v)B\tau. \end{aligned} \tag{3.11}$$

Following Refs. [36, 85], we carry out a gauge transformation to find a one-body Hamiltonian:

$$H^\tau_{ex} = \frac{\hbar^2}{2\mu}\mathbf{k}^2 + \frac{\hbar eB}{2}\left(\frac{1}{m_c} - \frac{1}{|m_v|}\right)l_z + \frac{e^2B^2}{8\mu}\mathbf{r}^2 + V\left(|\mathbf{r}|\right) - (\mu_c - \mu_v)B\tau \tag{3.12}$$

where $\mathbf{r} = \mathbf{r}_e - \mathbf{r}_h$ is the electron-hole separation, $\mathbf{k}$ is the associated canonical momentum, $\mu = m_c|m_v|/(m_c + |m_v|)$, and $l_z = \hat{z}\cdot(\mathbf{r}\times\mathbf{k})$. For bright excitons we assume $l_z = 0$, i.e. that they are s-type [40, 70, 86]. When the electron-hole interaction dominates, $\frac{e^2B^2}{8\mu}\mathbf{r}^2$ can be treated as a perturbation. Therefore the only term which can give rise to a linear magnetic field dependence of the exciton energy is the last term in Eq. 3.12.

We also estimate the energy shift due to the quadratic term $\frac{e^2B^2}{8\mu}\mathbf{r}^2$ in the exciton Hamiltonian. In the regime where the magnetic length ($l_B = \sqrt{\frac{\hbar}{eB}}$) is larger than the exciton Bohr radius, this term leads to a quadratic shift of the exciton transition energy as demonstrated in experiments on quantum wells [85,87–89]. Theoretically, this could manifest in our experiments as a quadratic term in the valley-averaged transition energy, but due to the small exciton Bohr radius for

TMDs (1-3 nm [40,70]) the correction should be small. We can estimate the diamagnetic shift using perturbation theory with the Wannier model above: the result is a quadratic increase of order $\frac{1}{8}\hbar(\omega_c + \omega_v)\left(\frac{a_B}{l_B}\right)^2 \approx 7\,\mu$eV at 6.7 T, where $\omega_{c(v)}$ is the electron (hole) cyclotron frequency, and a_B is the exciton Bohr radius. This energy shift is below our measurement sensitivity.

CHAPTER 4

CONTROL OF SPIN-ORBIT TORQUES THROUGH CRYSTAL SYMMETRY IN TUNGSTEN DITELLURIDE/PERMALLOY BILAYERS

The following chapter is based on work published in Nature Physics (Ref. [90]), and appears here with modifications and additional data. Changes include the addition of data from new devices (see Table 4.1) and expanded discussions of the symmetry constraints for current applied at arbitrary angles to the WTe_2 crystal axes (see Fig. 4.5 and Section 4.8.5).

4.1 Introduction

Current-induced torques generated by materials with strong spin-orbit (S-O) interactions are a promising approach for energy-efficient manipulation of non-volatile magnetic memory and logic technologies [91]. However, S-O torques observed to date are limited by their symmetry so that they cannot efficiently switch the nanoscale magnets with perpendicular magnetic anisotropy (PMA) that are required for high-density applications [92]. S-O torques generated either in conventional heavy metal/ferromagnet thin-film bilayers [93–103], or in topological insulator/ferromagnet bilayers [104, 105], are restricted by symmetry to have a particular form: an "antidamping-like" component oriented in the sample plane that is even upon reversal of the magnetization direction [106], $\hat{m}$, plus an "effective field" component that is odd in $\hat{m}$. The fact that the antidamping torque lies in-plane means that the most efficient mechanism of S-O-torque-driven magnetic reversal for small devices (antidamping switching) [107, 108], is available only for magnetic samples with in-plane magnetic anisotropy [98, 99], and not PMA samples (see also Section 4.8.1). S-O torques

can also arise from broken crystalline inversion symmetry, even within single layers of ferromagnets [109–112] or antiferromagnets [113], but the antidamping torques that have been measured to date are still limited to lie in the sample plane [111, 112, 114]. Here we demonstrate that the allowed symmetries of S-O torques in spin source/ferromagnet bilayer samples can be changed by using a spin source material with reduced crystalline symmetry. We generate an out-of-plane antidamping S-O torque when current is applied along a low-symmetry axis of the bilayer. This previously-unobserved form of S-O torque is quenched when current is applied along a high symmetry axis.

As our low-symmetry spin source material, we use the semi-metal WTe_2, a layered orthorhombic transition metal dichalcogenide (TMD) with strong S-O coupling [115, 116, 116–118]. TMD materials are attractive for use as sources of S-O torque because they can be prepared as monocrystalline thin films with atomically-flat surfaces down to the single-layer level. They provide a broad palette of crystal symmetries, S-O coupling strengths, and electrical conductivities [8, 119]. Other research groups have demonstrated recently the generation of S-O torques in devices made with the TMD MoS_2 [120], and the Onsager reciprocal process (voltage generation from spin pumping) in MoS_2/Al/Co heterostructures [121]. Compared to MoS_2, the crystal structure of WTe_2 has lower symmetry, with the space group $Pmn2_1$ for bulk WTe_2 crystals [122]. In a WTe_2/ferromagnet bilayer sample, the screw-axis and glide plane symmetries of this space group are broken at the interface, so that WTe_2/ferromagnet bilayers have only one symmetry, a mirror symmetry relative to the *bc* plane depicted in Fig. 4.1a. There is no mirror symmetry in the *ac* plane, and therefore no 180° rotational symmetry about the *c*-axis (perpendicular to the sample plane).

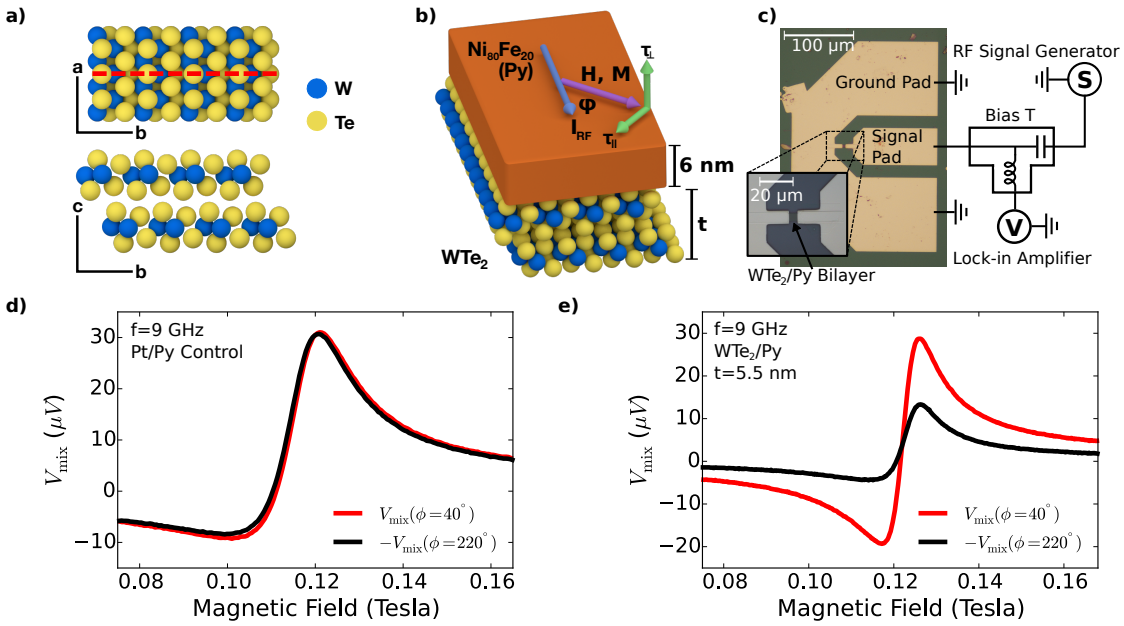

Figure 4.1: **a)** Crystal structure near the surface of WTe_2. The surface possesses mirror symmetry with respect to the bc plane (dashed line), but not with respect to the ac plane, and therefore it is also not symmetric relative to a 180° rotation about the c-axis. **b)** Schematic of the bilayer WTe_2/Permalloy sample geometry. **c)** Optical images of the sample geometry including contact pads, with the circuit used for spin-torque FMR measurements. **d)** ST-FMR resonances for Pt(6 nm)/Py(6 nm) control samples, with the magnetization oriented at 40° and 220° relative to the current direction. The applied microwave power is 0 dBm. **e)** ST-FMR resonances for a WTe_2(5.5 nm)/Py(6 nm) sample with current applied along the *a*-axis, with the magnetization oriented at 40° and 220° relative to the current direction. The applied microwave power is 5 dBm.

4.2 Making the devices

Our device fabrication starts with high quality artificially-grown crystals of WTe_2 (from HQ Graphene) which we exfoliate onto a high-resistivity silicon wafer with 1 μm of thermal oxide. The exfoliation is performed in flowing dry nitrogen in the load-lock chamber of our sputtering system, so that the exfoliated samples can be transferred into the sputter system with minimal exposure to air. We have also carried out measurements on samples exfoliated in vacuum

with similar results. The exfoliation results in the deposition of single-crystal flakes of WTe_2 up to 40 μm in lateral extent and with a distribution of thicknesses. To minimize damage to the WTe_2 flakes, we use grazing-angle magnetron sputtering to deposit 6 nm of permalloy (Py=$Ni_{81}Fe_{19}$) onto the WTe_2. The Py deposition rates are kept below 0.2 Å/s and are performed in an ambient Ar background pressure of 4 mtorr while the substrate rotates at 3 rotations per minute. We then deposit a protective aluminum oxide cap in situ onto the WTe_2/Py bilayer by sputter deposition of 1 nm aluminum which is subsequently oxidized in a dry N_2/O_2 mixture. The Py magnetic moment is in-plane for all devices studied.

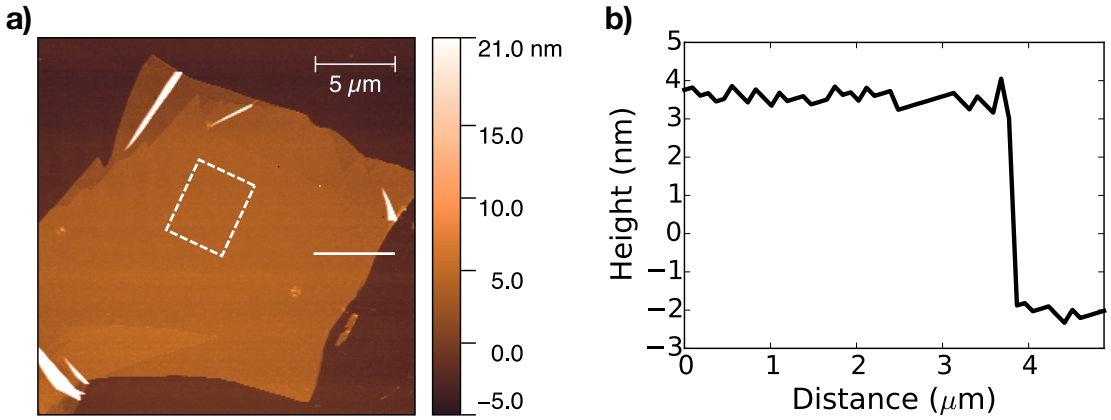

Figure 4.2: **a)** An atomic force microscopy image of the WTe_2 flake used for fabrication of Device 15 after deposition of the Permalloy layer and aluminum oxide cap but before any lithographic processing. The active region used for the device (dashed white box) has a RMS surface roughness ¡ 300 pm.**b)** A linecut [white line in **a)**] from the edge of the WTe_2 flake, showing an average thickness of 5.5 nm.

After deposition of the ferromagnet and aluminum oxide cap, we use optical contrast and atomic force microscopy (AFM) to select WTe_2 flakes for further study. Flakes are chosen to ensure an active region with homogenous thickness (i.e. no monolayer steps or tape residue) and minimal roughness (typically < 300

pm RMS). An AFM image of a typical WTe_2/Py bilayer prior to patterning is shown in Fig. 4.2.

The WTe_2/Py bilayers are patterned into bars of width 3-4 μm. The bars are defined via Ar ion milling, using either a hard mask (silicon or aluminum oxide) or an e-beam exposed PMMA/HSQ bilayer. After etching, another step of e-beam lithography is used to make electrical contact to the bars with Ti/Pt contact pads, which have a ground-signal-ground geometry compatible with microwave probes (Fig. 4.1c). The active region between the contacts is 3-6 μm long. For hard-mask devices, an additional reactive-ion etching (RIE) or wet etch step is used prior to the Ti/Pt deposition to remove the mask in the contact region.

The Py resistivity in our devices is (100±20) Ωcm. The WTe_2 bulk resistivity value is (380±10)Ωcm with the current flowing along the *a*-axis and is likely higher in thinner flakes [118]. The resistivity of WTe_2 is anisotropic, and we find the resistivity with current flowing along the *a*-axis to be 1.4-2 times larger than the resistivity for current flowing along the *b*-axis.

The crystal axes of WTe_2 are determined by polarized Raman measurements using a Renishaw inVia confocal Raman microscope with a linearly polarized 488 nm wavelength excitation and a co-linear polarizer placed in front of the spectrometer entrance slit. The WTe_2 sample is positioned such that the light is incident normal to the sample surface and the excitation electric field is in the sample plane. Previous calculations and measurements have shown that the 165.7 cm^{-1} (P6) and 211.3 cm^{-1} (P7) Raman peaks of WTe_2 are sensitive to the alignment of the electric field and the crystal axes [123]. We measure the intensity of the P6 and P7 Raman peaks as a function of angle by rotating the

sample from 0° to 180° in steps of 10° or 20° (keeping the electric field in the sample plane). The angle for which the ratio of peak intensities, P6/P7, is maximized identifies the *a*-axis, allowing determination of the angle between the *a*-axis and current direction, ϕ_{a-I}. We have measured a total of 15 devices with bars oriented at a variety of alignments to the WTe_2 crystal axes and with WTe_2 thicknesses ranging from 1.8 nm to 15.0 nm.

4.3 Measuring current-induced torques

To measure the S-O torques produced by our WTe_2/Py bilayers, we use the technique of spin-torque ferromagnetic resonance (ST-FMR) [96, 111], performed at room temperature. In ST-FMR, an in-plane alternating current is applied through the bilayer at a frequency characteristic of ferromagnetic resonance (here, 5-12 GHz). The torques generated by the current excite the magnetic moment away from equilibrium and cause it to precess, creating a time-dependent change in the resistance of the bilayer due to the anisotropic magnetoresistance (AMR) in the ferromagnet. This change in resistance mixes with the alternating current to create a DC voltage across the bar, V_{mix}. The circuit used to measure V_{mix} is depicted in Fig. 4.1c. By sweeping an applied in-plane magnetic field we tune the ferromagnetic resonance through the applied frequency, giving rise to a resonance feature in V_{mix} (Figs. 4.1d). The in-plane ($\tau_{\parallel}$) and out-of-plane ($\tau_{\perp}$) torque amplitudes defined in Fig. 4.1b contribute to the symmetric and antisymmetric parts of the lineshape, respectively. This allows determination of the torque components by fitting V_{mix} as a function of applied magnetic field to a sum of symmetric and antisymmetric Lorentzians (see Section 4.8.2). The amplitudes of the Lorentzians are related to the two components of torque by:

$$V_S = -\frac{I_{RF}}{2}\frac{dR}{d\phi}\frac{1}{\alpha_G\gamma\left(2B_0 + \mu_0 M_{eff}\right)}\tau_{\parallel} \tag{4.1}$$

$$V_A = -\frac{I_{RF}}{2}\frac{dR}{d\phi}\frac{\sqrt{1 + \mu_0 M_{eff}/B_0}}{\alpha_G\gamma\left(2B_0 + \mu_0 M_{eff}\right)}\tau_{\perp}, \tag{4.2}$$

where R is the device resistance, ϕ is the angular orientation of the magnetization relative to the direction of applied current in the sample, $dR/d\phi$ is due to the AMR in the Py, $\mu_0 M_{eff}$ is the out-of-plane demagnetization field, B_0 is the resonance field, I_{RF} is the microwave current in the bilayer, α_G is the Gilbert damping coefficient and γ is the gyromagnetic ratio. In our devices, $\mu_0 M_{eff}$ = 0.7 Tesla and α_G = 0.011 as determined by the ST-FMR resonance frequency and linewidth, respectively, and $R(\phi)$ is measured directly by rotating the magnetic field using a projected-field apparatus.

4.4 Current-induced torques in WTe_2/Py bilayers

During a ST-FMR measurement, the applied magnetic field fixes the average angle of the magnetization at a given value, ϕ. The strengths of the current-induced torques for different angles of the magnetization are related to the symmetries of the device. For example, in a Pt/Py structure, the two-fold rotational symmetry requires that the S-O torque change sign when the magnetization is rotated in-plane by 180°, correspondingly changing the sign of V_{mix} but maintaining the same magnitude. This is illustrated in Fig. 4.1d where we plot ST-FMR traces for a Pt(6 nm)/Py(6 nm) bilayer at ϕ = 40° and 220°, showing nearly identical lineshapes after multiplying the ϕ = 220° trace by -1.

Figure 4.1e shows the results of the same experiment carried out on a WTe_2/Py bilayer with the current applied along the low-symmetry crystal axis of WTe_2, parallel to the *a*-axis (device 1). In this case, we find that $V_{\mathrm{mix}}\,(40^\circ)$ and $-V_{\mathrm{mix}}\,(220^\circ)$ differ significantly in both amplitude and shape, indicating that the current-induced torques in the two cases differ in both magnitude and direction. This observation is incompatible with two-fold rotational symmetry, indicating that the current-induced torques are affected by the reduced symmetry of the WTe_2 surface.

To analyze this result in more detail, we consider the full angular dependence of the ST-FMR signal as an external magnetic field is used to rotate the direction of the magnetization within the sample plane. In a simple heavy metal/ferromagnet bilayer with no broken lateral symmetries, the current-induced torque amplitudes (due to the spin Hall effect, the Rashba-Edelstein effect, or the Oersted field) have a $\cos\phi$ dependence [96, 104]. The AMR in Permalloy has an angular dependence that scales as $\cos^2\phi$, which enters V_{mix} as $dR/d\phi \propto \sin 2\phi$. The product of these two contributions then yields the same angular dependence for the symmetric and antisymmetric ST-FMR components: $V_{\mathrm{S}} = S\cos\phi\sin 2\phi$ and $V_{\mathrm{A}} = A\cos\phi\sin 2\phi$. Our Pt/Py control samples are well described by this behavior (Fig. 4.3a; the parameter ϕ_0 accounts for any misalignment between the sample and the electro-magnet, and is typically $< 5^\circ$).

For our WTe_2/Permalloy samples with current along the *a*-axis, the symmetric component of the ST-FMR signal also has this form (Fig. 4.3b top panel). The non-zero symmetric component indicates that S-O torques are present in the WTe_2/Permalloy bilayer, since the symmetric component corresponds to an in-plane torque and cannot be generated by an Oersted field. However, the

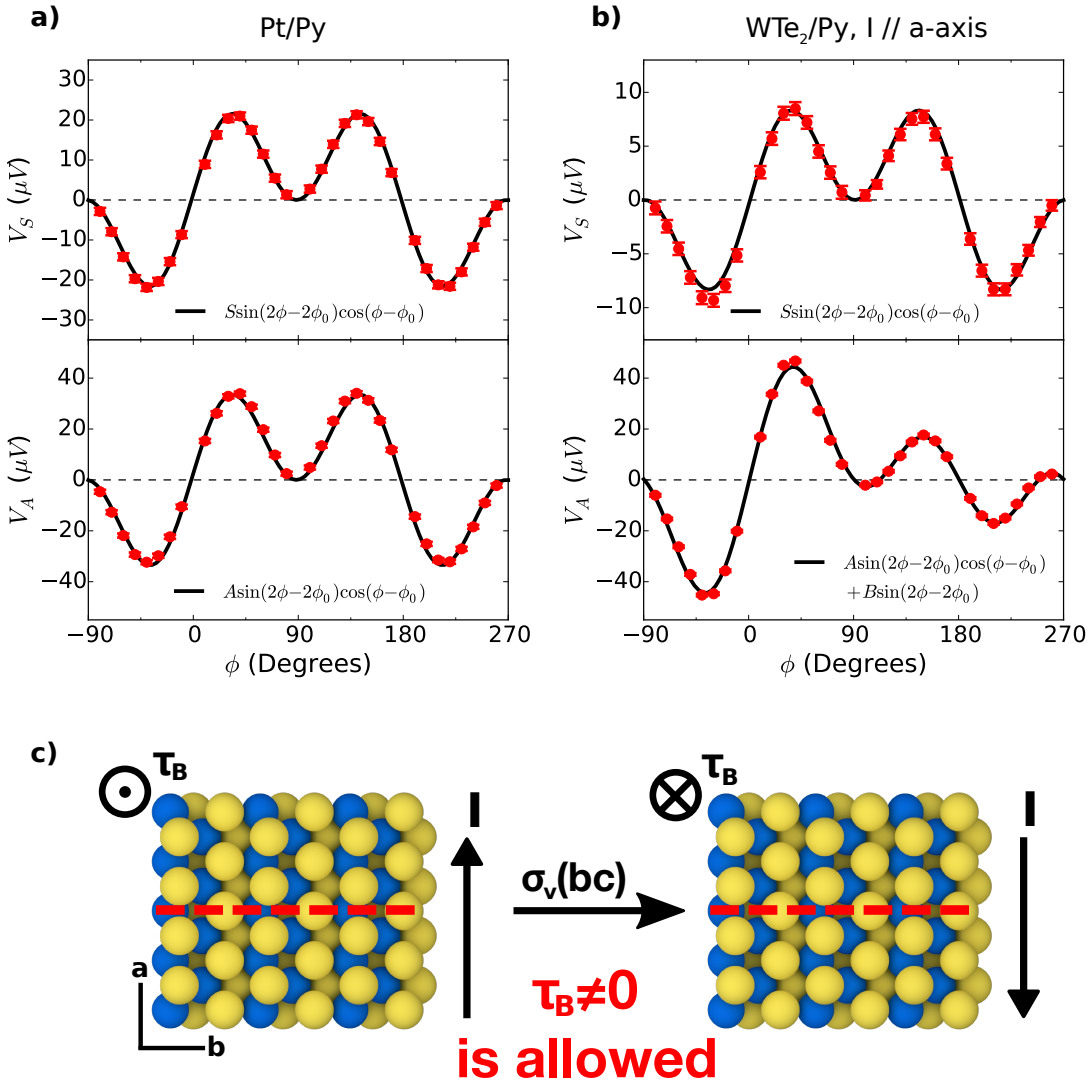

Figure 4.3: **a)** Symmetric and antisymmetric ST-FMR resonance components for a Pt(6 nm)/Py (6 nm) control sample as a function of in-plane magnetic-field angle. The microwave frequency is 9 GHz and the applied microwave power is 0 dBm. The parameter ϕ_0 accounts for any misalignment between the sample and the magnet. **b)** Symmetric and antisymmetric ST-FMR resonance components for a WTe_2(5.5 nm)/Py (6 nm) device (device 1) as a function of in-plane magnetic-field angle, with current applied parallel to the a-axis. The microwave frequency is 9 GHz and the applied microwave power is 5 dBm. The error bars in **a** and **b** represent the estimated standard deviations from the least-squares fitting procedure used to determine V_A and V_S. **c)** Illustration that a magnetization-independent, linear-in-current out-of-plane S-O torque is allowed by symmetry for current applied along the *a*-axis of a WTe_2/Py bilayer.

more striking result is that the angular dependence of the antisymmetric component is very different from $\cos\phi \sin 2\phi$ (Fig. 4.3b bottom panel). The variations in the absolute values of signal amplitudes reflect the broken symmetries of the WTe_2 surface: the absence of mirror symmetry in the *ac* plane (corresponding to $\phi \rightarrow 180^\circ - \phi$, since $\hat{m}$ is a pseudovector) and the absence of twofold rotational symmetry about the *c*-axis ($\phi \rightarrow 180^\circ + \phi$). This result indicates the existence of a source of out-of-plane torque not previously observed in any S-O torque experiment.

The unusual angular dependence we measure for the antisymmetric ST-FMR signal with current applied along the *a*-axis can be well fit by the simple addition of a term proportional to $\sin 2\phi$:

$$V_A = A \cos\phi \sin 2\phi + B \sin 2\phi \tag{4.3}$$

where A and B are constants independent of the field angle (see the solid line in Fig. 4.3 bottom panel). To quantitatively translate the measured angular dependence of V_S and V_A to torques, we can use Eqs. 4.1 and 4.2 to remove the contribution from the angular dependence of the AMR. The fits in Fig. 4.3b then correspond to angular dependences for the in-plane and perpendicular torque amplitudes of the form

$$\tau_{\parallel}(\phi) = \tau_S \cos(\phi) \tag{4.4}$$

$$\tau_{\perp}(\phi) = \tau_A \cos(\phi) + \tau_B \tag{4.5}$$

where τ_S, τ_A, and τ_B are independent of ϕ. The terms proportional to $\cos\phi$ are the usual terms observed previously, and in the Pt/Py control samples. The new term (τ_B) corresponds to an out-of-plane torque that is independent of the in-plane magnetization orientation; i.e., it is even in $\hat{m}$ and therefore an antidamping-like torque. It is consistent with predictions [124] that bro-

ken lateral mirror symmetry can allow an out-of-plane torque of the form $\boldsymbol{\tau}_{\mathrm{AD}} \propto \hat{m}\times(\hat{m}\times\hat{c})$. That an out-of-plane antidamping-like torque with the form of τ_{B} could exist has also been discussed in an analysis of the allowed symmetries for S-O torques in GaMnAs/Fe samples [114], but this torque has not previously been identified in experiment.

In commonly studied bilayer systems without any broken in-plane symmetries, a linear-in-current out-of-plane torque that is independent of the in-plane magnetization angle cannot exist by symmetry. For example, the presence of a twofold rotation disallows τ_{B}. In samples with twofold rotational symmetry, rotating the sample by 180° is equivalent to changing the sign of an in-plane current without changing the sign of τ_{B}, which violates the linear-in-current requirement. However, WTe_2/Py bilayers do not have two-fold rotational symmetry. The only symmetry in our WTe_2/Py bilayers is the *bc* plane mirror, $\sigma_v(bc)$. The effect of $\sigma_v(bc)$ on a WTe_2/Py bilayer with current flowing along the *a*-axis is illustrated in Fig. 4.3c. Both the out-of-plane torque (a pseudovector) and the current change sign under $\sigma_v(bc)$, $\tau_{\mathrm{B}} \rightarrow -\tau_{\mathrm{B}}$ and $I \rightarrow -I$, which is the expected behavior for a current-generated S-O torque: the sign of torque must change with the sign of the current. A torque with the symmetry of τ_{B} is therefore allowed for WTe_2/Py bilayers with current along the *a*-axis.

4.5 Dependence of torques in WTe_2/Py bilayers on the current flow direction

We observe that τ_{B} goes to zero when the current is applied parallel to the *b*-axis of WTe_2. Figure 4.4a shows the antisymmetric ST-FMR component V_{A} (red

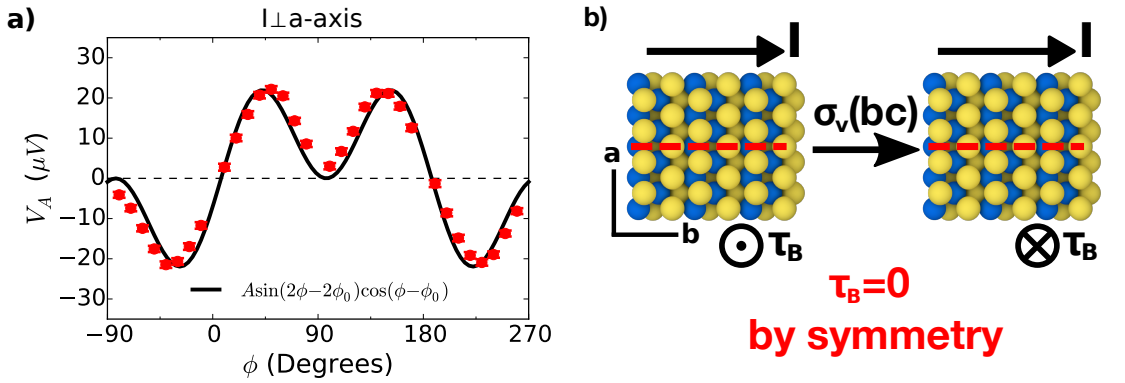

Figure 4.4: **a)** Antisymmetric ST-FMR resonance component for a WTe_2(15 nm)/Py (6 nm) device (device 2) as a function of in-plane magnetic-field angle, with current applied parallel to the *b*-axis. The microwave frequency is 9 GHz and the applied microwave power is 5 dBm. The error bars in **a)** represent the estimated standard deviations from the least-squares fitting procedure used to determine V_A. **b)** Illustration that a magnetization-independent, linear-in-current out-of-plane S-O torque is forbidden by symmetry for current applied along the *b*-axis.

circles) as a function of ϕ for device 2, in which the current is applied along the *b*-axis. The angular fit to Eq. 4.3 yields a value of B equal to 0 within experimental uncertainty. This result is again consistent with the symmetries of the WTe_2 surface layer. When the mirror symmetry operation $\sigma_v\,(bc)$ is applied in this case (Fig. 4.4b), the out-of-plane torque is inverted but the current is not, and therefore τ_B is forbidden by symmetry. Higher-order angular terms are symmetry-allowed for current along the *b*-axis, and can be included in fits of V_A versus ϕ to improve the quantitative agreement (Section 4.8.6). We also continue to observe a nonzero symmetric ST-FMR signal when the current is aligned with the *b*-axis, which has the same functional form as the symmetric ST-FMR signal in the devices with current along the *a*-axis (Section 4.8.4).

We further investigated the symmetry dependence of τ_B by studying devices with different angles, ϕ_{a-I}, between the *a*-axis of the WTe_2 and the ap-

plied current direction. We fabricated 26 devices with different ϕ_{a-I} and performed full angle-dependent ST-FMR measurements on each in order to extract A, B and S (see Table 4.1). Figure 4.5a shows the ratio of τ_B/τ_A at a given frequency (f = 9 GHz) as a function of ϕ_{a-I} for the first 15 of these devices (those for which the crystalline axes were identified via Raman spectroscopy). We consistently see that the ratio of τ_B/τ_A is large when current is aligned with the a-axis, and is gradually quenched as the projection of the current along the b-axis grows. This provides strong additional evidence that the observed magnetization-independent out-of-plane torque is correlated with the symmetries present in the WTe_2 crystal.

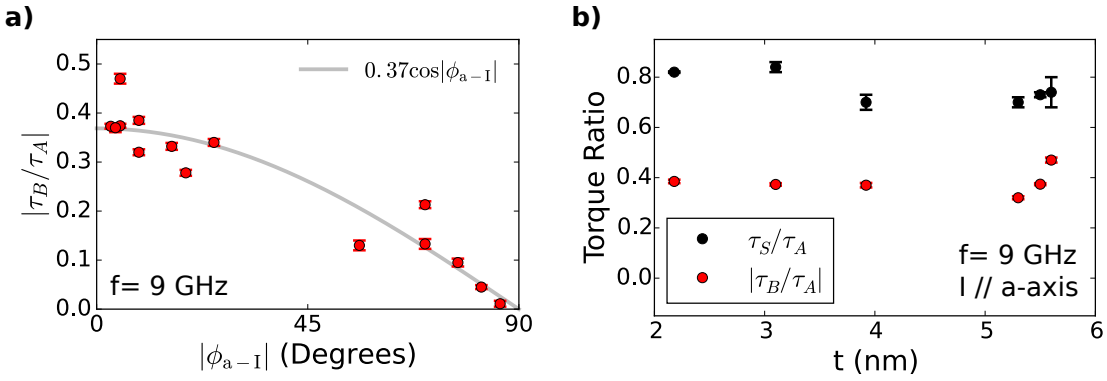

Figure 4.5: **a)** Ratio of the out-of-plane antidamping torque τ_B to the out-of-plane effective-field torque τ_A as a function of the angle between the a-axis and the applied current. The grey line in Fig. 4.5a shows a one-parameter fit to $\tau_B/\tau_A = \cos|\phi_{a-I}|$. **b)** Torque ratios as a function of the thickness of the WTe_2 layer for current applied along the a-axis. Here τ_S is the in-plane current-induced torque. The error bars in **a)** and **b)** represent estimated standard deviations calculated via error propagation from the least-squares fitting procedure used to determine τ_A, τ_B, and τ_S.

The grey line in Fig. 4.5a shows a one-parameter fit to $\tau_B/\tau_A \propto \cos|\phi_{a-I}|$. This is the expected behavior if τ_A (per unit electric field) does not have a strong dependence on ϕ_{a-I}, and the conductivity of the device is rather isotropic (since it is dominated by the permalloy). Assuming the torques are linear in the applied

electric field, τ_B should scale like the projection of the applied electric field onto the a-axis, and therefore $\tau_B/\tau_A \propto \cos\phi_{a-I}$. The large scatter in our data frustrates a more detailed comparison with different scenarios for the anisotropy.

The dependence of the measured torques on WTe_2 thickness provides insight into the mechanism of torque generation. If the torques arise through bulk mechanisms, clear thickness dependences should be expected; however, if the torques are generated by interface effects they should not depend on WTe_2 thickness. Figure 4.5a shows the dependence of the torque ratios τ_B/τ_A and τ_S/τ_A on WTe_2 thickness for devices that have current along the a-axis. (The individual dependences of τ_A, τ_B, and τ_S on WTe_2 thickness and on the angle of the current relative to the a-axis are plotted in Section 4.8.4.) Neither τ_B/τ_A nor τ_S/τ_A show any significant dependence on WTe_2 thickness. This requires τ_A, τ_B, and τ_S to either all have the same thickness dependence or have no definite thickness dependence. However, a bulk contribution to τ_B is forbidden by the screw symmetry of the WTe_2 crystal structure. The bulk WTe_2 structure is mapped onto itself if it is rotated by 180° about an axis normal to the layers (c-axis) and translated by half a unit cell along both the c and a-axis (in the c direction, half a unit cell is one layer spacing). A bulk contribution to τ_B would be left unaltered by this operation, while the direction of an in-plane charge current is reversed. This implies that there can be no net bulk contribution to that is linear in the applied in-plane current (see also Section 4.8.7). We have verified the surface origin of τ_B experimentally using a sample containing a single-layer step; the strength of is suppressed because contributions from two surfaces with opposite symmetry largely cancel (Section 4.8.7). The symmetry constraints on τ_B, together with the lack of dependence on WTe_2 thickness for τ_B/τ_A and τ_S/τ_A, suggest that all three torque components arise from interfacial effects in the WTe_2/Py bilayer.

The strength of the individual components of torque can be determined quantitatively from Eqs. 4.2 and 4.1, using independently-measured values of the resistance as a function of magnetization angle ($dR/d\phi$) and the transmitted and reflected microwave power (S_{21} and S_{11}) in order to determine I_{RF} (Section 4.8.2). We will express these strengths as torque conductivities (σ_{S}, σ_{A}, σ_{B}; torques per unit area per unit electric field) because the electric field applied across the device can be determined accurately, while the division of current density flowing in the different layers has larger uncertainties. We find for current along the a-axis that $\sigma_{\mathrm{S}} = (8 \pm 2) \times 10^3 (\hbar/2e)(\Omega\mathrm{m})^{-1}$, $\sigma_{\mathrm{A}} = (9 \pm 3) \times 10^3 (\hbar/2e)(\Omega\mathrm{m})^{-1}$, and $\sigma_{\mathrm{B}} = (3.6 \pm 0.8) \times 10^3 (\hbar/2e)(\Omega\mathrm{m})^{-1}$, where the uncertainties give the standard deviation across our devices.

We find it interesting that although a broken lateral mirror symmetry should also allow additional terms for the in-plane S-O torque when current is applied along the a-axis, for example an effective-field torque of the form $\hat{m}\times\hat{c}$, we detect no such contributions. A term $\propto \hat{m} \times \hat{c}$ would add a ϕ-independent contribution to Eq. 4.4, $\tau_{\parallel}(\phi) \rightarrow \tau_{\mathrm{S}} \cos\phi + \tau_{\mathrm{T}}$ that would cause the absolute values of the amplitudes for the symmetric part of the ST-FMR resonance (Fig. 4.3b, upper panel) to be asymmetric under the operations $\phi \rightarrow 180^\circ + \phi$ and $\phi \rightarrow 180^\circ - \phi$. We can set a limit for our devices that $|\tau_{\mathrm{T}}| < 0.05\tau_{\mathrm{S}}$. Our results are therefore opposite a report about S-O torques in "wedge," [124] samples, which claimed that the breaking of lateral mirror symmetry by the wedge structure generated an effective field torque, but no out-of-plane antidamping torque. We question whether the extremely small thickness gradient in Ref. [124] (a difference in average thickness of ≤ 0.5 picometers, or 0.002 of an atom, between the two sides of a 20-μm-wide sample) actually provides a meaningful breaking of structural mirror symmetry.

4.6 Magnetic anisotropy of WTe_2/Py bilayers

We note one additional consequence of strong S-O coupling at the WTe_2/Py interface – the magnetic anisotropy easy axis of the Py is determined by the crystal lattice of the WTe_2. The magnetic anisotropy can be determined from our ST-FMR data via the ϕ dependence of the magnetic resonance frequency and by direct AMR measurements (Section 4.8.2). Regardless of the orientation of the sample channel with respect to the WTe_2 crystal lattice, we find that the magnetic easy axis is always parallel to the b-axis of WTe_2. The effective anisotropy field in different devices ranges from 4.9 to 17.3 mT for 6 nm of Py (Table 4.1).

4.7 Conclusion

In summary, we have demonstrated that it is possible to generate an out-of-plane antidamping-like S-O torque in spin-source/ferromagnet bilayers by using a spin-source material whose surface crystal structure has a broken lateral mirror symmetry. This is important as it provides a strategy for achieving efficient manipulation of magnetic devices with perpendicular magnetic anisotropy. Compared to in-plane-magnetized devices, PMA devices are of interest because they can be scaled to smaller sizes and higher density while maintaining thermal stability. PMA devices can be switched much more efficiently using an out-of-plane antidamping torque, τ_{AD}, compared to an effective field torque, τ_{FL}, since the effective field torque required for switching in the macrospin limit is $\tau_{FL} \approx \gamma H_{an}$, where H_{an} is the anisotropy field, while the antidamping torque required is much smaller: $\tau_{AD} \approx \alpha_G \gamma H_{an}$, with $\alpha_G \approx 0.01$ (Ref. [108]). Previously, because S-O torques could generate an antidamping-

like component only in the sample plane, they have been incapable of switching PMA devices by this efficient antidamping process [125–130] – an in-plane antidamping torque switches PMA devices through a mechanism involving domain nucleation and domain-wall propagation that becomes inefficient at small size scales [92]. Our results therefore suggest a strategy, based on control of broken crystal symmetry in materials with strong S-O coupling, that has the potential to enable efficient antidamping switching of PMA memory and logic devices at the 10's of nm size scale.

4.8 Supplemental information

4.8.1 Comparison of mechanisms for current-induced switching of magnetic layers with perpendicular magnetic anisotropy (PMA)

In principle, spin-orbit torques with three different symmetries can drive switching of PMA magnetic layers, each associated with different reversal mechanisms and yielding different values for the critical torque required for switching. [Note that in this discussion we will consider all torques per unit magnetization, so that $\boldsymbol{\tau}$ has the same units as $d\hat{m}/dt$, where $\hat{m}$ is the magnetic orientation.] (i) If the current can produce an effective field in the vertical ($\hat{z}$) direction, yielding a torque of the form $\boldsymbol{\tau}_{\mathrm{FL}} = -\gamma H_{\mathrm{FL}}(\hat{m} \times \hat{z})$, then in a macrospin approximation switching will occur at a critical value $H_{\mathrm{FL}} = H_{\mathrm{an}}$, where H_{an} is the perpendicular anisotropy field. (ii) If the current produces an in-plane anti-

damping torque of the form $\boldsymbol{\tau}_{\mathrm{AD},\parallel} = \gamma\tau^0_{\mathrm{AD},\parallel}\hat{m}\times(\hat{m}\times\hat{y})$, then deterministic switching can be achieved if there is also a symmetry-breaking effective field with a component along the current direction [97,131], but the switching mechanism in this case is not actually based on a change in the magnetic layer's effective damping because the antidamping torque is perpendicular to the magnetization. The torque in this case must still overcome the anisotropy field, so that the critical value of the torque in the macrospin limit is $\tau^0_{\mathrm{AD},\parallel} \approx \gamma H_{\mathrm{an}}/2$ (Refs. [131, 132]). In samples larger than a few tens of nm diameter, an in-plane antidamping torque can, alternatively, drive a more efficient non-macrospin reversal process involving current-generated domain wall motion [126], but measurements indicate that this becomes ineffective for the highly-scaled PMA devices that are desired for applications [92]. (iii) If the current produces an out-of-plane antidamping torque of the form $\boldsymbol{\tau}_{\mathrm{AD},\perp} = \gamma\tau^0_{\mathrm{AD},\perp}\hat{m}\times(\hat{m}\times\hat{z})$, then in this case the direction of the torque is parallel to the magnetization so that it does have the ability to change the effective damping of the magnetic layer. Switching occurs when the effective damping is driven negative, resulting in a critical value of torque $\tau^0_{\mathrm{AD},\perp} = \gamma\alpha_{\mathrm{G}}H_{\mathrm{an}}$ [107, 108]. Because the Gilbert damping is typically on the order of 0.01, an out-of-plane antidamping component has the ability to drive switching of PMA magnetic devices at much lower values of torque than the other two mechanisms, for sample sizes smaller than a few 10's of nm.

4.8.2 Analysis of ST-FMR measurements

We model the ST-FMR measurements by using the Landau-Lifshitz-Gilbert-Slonczewski (LLGS) equation to calculate the precessional dynamics of the magnetization direction, $\hat{m}(t)$, in the macrospin approximation in response to the in-

plane and out-of-plane torque amplitudes, $\tau_\parallel$ and $\tau_\perp$ [96, 107]. This determines the ST-FMR mixing voltage as

$$V_{\mathrm{mix}} = \langle I(t)R[m(t)]\rangle_t = V_{\mathrm{S}}\frac{\Delta^2}{(B_{\mathrm{app}}-B_0)^2+\Delta^2} + V_{\mathrm{A}}\frac{\Delta(B_{\mathrm{app}}-B_0)}{(B_{\mathrm{app}}-B_0)^2+\Delta^2} \tag{4.6}$$

where B_{app} is the applied magnetic field and Δ is the linewidth. The $\hat{m}(t)$ dependence of the device resistance arises from the anisotropic magnetoresistance (AMR) of the ferromagnet Permalloy. We determine the symmetric and antisymmetric amplitudes, V_{S} and V_{A}, by fitting Eq. to measurements of the mixing voltage as a function of applied magnetic field. These amplitudes are related to the torque amplitudes $\tau_\parallel$ and $\tau_\perp$ by Eqs. 4.1 and 4.2. We note $\tau_\parallel$ and $\tau_\perp$ are normalized by the total angular momentum of the magnet, and so have dimensions of frequency. We determine torque ratios from the ratio of Eqs. 4.1 and 4.2 together with measured values for B_0 and M_{eff}. We obtain the value of B_0 via fits of the resonance lineshape, and we estimate M_{eff} from the frequency dependence of B_0 using the Kittel formula $2\pi f = \gamma\sqrt{B_0(B_0+\mu_0 M_{\mathrm{eff}})}$. As we discuss in Section 4.8.3, B_0 and M_{eff} depend on ϕ due to the in-plane magnetic anisotropy of our samples. For our analysis we use angle-averaged values for these quantities; the error in doing so is less than 5% due to the small degree of angular variation.

To obtain quantitative measurements of the individual torque components using Eq. 4.1 or Eq. 4.2 (i.e. not just their ratios), it is also necessary to determine α_{G}, $R(\phi)$, and I_{RF}. The Gilbert damping is estimated from the frequency dependence of the linewidth via $\Delta = 2\pi f\alpha_{\mathrm{G}}/\gamma + \Delta_0$, where Δ_0 is the inhomogeneous broadening. To obtain the AMR we measure the device resistance as a function of a rotating in-plane magnetic field (with magnitude 0.08 T) applied via a projected-field magnet. Fitting these data to $R_0 + \Delta R\cos^2(\phi-\phi_0)$ allows calculation of $dR/d\phi$ (Fig. 4.6). To measure the RF current, we use a vector network analyzer to estimate the reflection coefficients of our devices (S_{11}) and the trans-

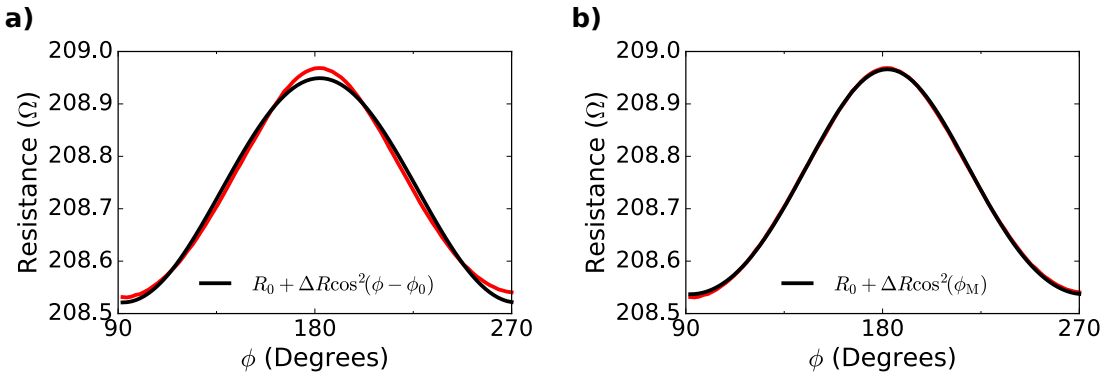

Figure 4.6: **a)** Resistance of Device 1 (red) as a function of the in-plane applied magnetic field angle. Measurements are made in a Wheatstone bridge configuration with a static magnetic field of 0.08 T. The fit (black) is used to extract $dR/d\phi$. **b)** Resistance of Device 1 (red) as a function of applied in-plane magnetic field angle. The fit here (black) takes into account the in-plane magnetic anisotropy via $\phi_M = \phi - \phi_0 + \frac{H_A}{2H}\sin 2(\phi - \phi_0)$ corresponding to an easy-axis perpendicular to the current flow direction (along the WTe_2 b-axis). The fit gives $H_A = 120 \pm 20$ Oe. We have not accounted for the non-saturated nature of $R(\phi)$ in our ST-FMR measurements.

mission coefficient of our RF circuit (S_{21}). These calibrations allow calculation of the RF current flowing in the device as a function of applied microwave power and frequency:

$$I_{RF} = 2\sqrt{1\text{mW}\cdot 10^{\frac{P_{source}(\text{dBm})+S_21(\text{dBm})}{10}}(1-|\Gamma|)^2/50\Omega} \tag{4.7}$$

where P_{source} is the power sourced by the microwave generator and $\Gamma = 10^{S_{11}(\text{dBm})/20}$.

The torque conductivity, defined as the angular momentum absorbed by the magnet per second per unit interface area per unit electric field, provides an absolute measure of the torques produced in a spin source/ferromagnet bilayer independent of geometric factors. For a torque τ_K (where $K = A$, B, S, or T) we calculate the corresponding torque conductivity via

$$\sigma_K = \frac{M_s l w t_{magnet}}{\gamma}\frac{\tau_K}{(lw)E} = \frac{M_s l t_{magnet}}{\gamma}\frac{\tau_K(1-\Gamma)}{(1+\Gamma)I_{RF}\cdot 50\Omega} \tag{4.8}$$

where M_s is the saturation magnetization, E is the electric field, l and w are the length and width of the WTe_2/Permalloy bilayer, and t_{magnet} is the thickness of the Permalloy. The factor $M_s l w t_{magnet}/\gamma$ is the total angular momentum of the magnet, which converts the normalized torque into units of angular momentum per second. Due to the unavailability of mm-scale WTe_2/Permalloy bilayers, we are unable to measure M_s directly via magnetometry, and instead approximate $M_s \approx M_{eff}$, which we have found to be accurate in other Permalloy bilayer systems [96].

4.8.3 Determination of the in-plane magnetic anisotropy

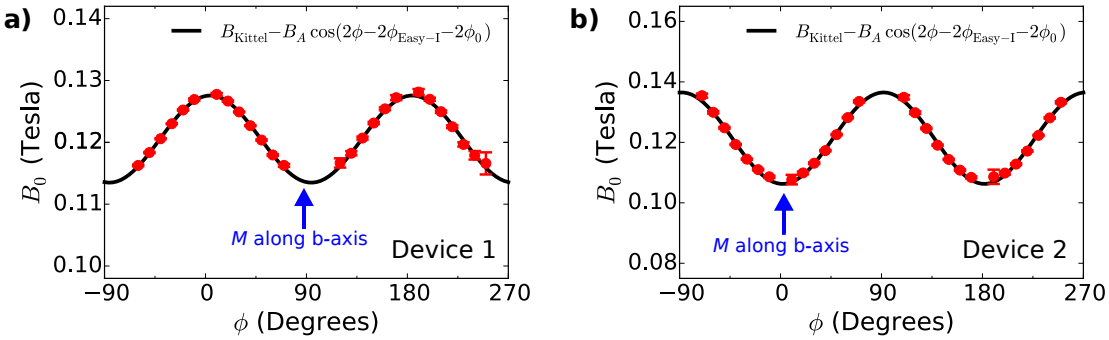

Figure 4.7: Ferromagnetic resonance field as a function of the in-plane magnetization angle for **a)** Device 1 and **b)** Device 2. The data are represented by red circles and the black lines are the indicated fits. In both cases the applied microwave frequency is 9 GHz and the power is 5 dBm. The blue arrows indicates the values of ϕ for which the magnetization lies along the b-axis. Error bars represent estimated standard deviations from the least-squares fitting procedure.

Figure 4.7 shows the magnetic field at ferromagnetic resonance as a function of the in-plane magnetization angle for Devices 1 and 2. For Device 1 the current flows nearly parallel to the a-axis ($\phi_{a-I} = -3°$), and for Device 2 it is nearly parallel to the b-axis ($\phi_{a-I} = 86°$). The data from both samples indicate the presence

of a uniaxial magnetic anisotropy within the sample plane, with an easy axis along the b-axis of the WTe_2. The angular dependence of the resonance field is described well by the form

$$B_0 = B_{\text{Kittel}} - B_{\text{A}} \cos(2\phi - 2\phi_{\text{Easy-I}} - 2\phi_0) \tag{4.9}$$

where B_{A} is the in-plane anisotropy field, related to the anisotropy energy K_{A} via $B_{\text{A}} = 2\mu_0 K_{\text{A}}/M_{\text{s}}$, B_{Kittel} is the resonance field without any in-plane anisotropy, $\phi_{\text{Easy-I}}$ is the angle from the current direction to the magnetic easy-axis and ϕ_0 is the angular misalignment extracted from the angular dependence of the mixing voltage. This equation also assumes $B_{\text{A}}, B_{\text{Kittel}} \ll \mu_0 M_{\text{eff}}$ which are valid approximations for our experiment. We find values for B_{A} of 7 mT and 15 mT for Device 1 and Device 2, respectively. We observe no unidirectional component to the magnetic anisotropy.

We performed similar fits for all of the devices listed in Table 4.1. In all cases the magnetic easy axis was along the b-axis within experimental uncertainty; i.e. $\phi_{\text{a-I}} = \phi_{\text{Easy-I}} + 90°$. Over all of our devices we find B_{A} to be in the range 2.4-17.3 mT. Some, but likely not all, of the device-to-device variation may be explained by differences in the sample shape.

To check that the Permalloy has a magnetic anisotropy that is entirely in the sample plane we fabricated a WTe_2/Py bilayer Hall bar using the same sample fabrication techniques and Py thickness as our ST-FMR devices. The Hall bar is oriented with the current along the WTe_2 a-axis ($\phi_{\text{a-I}} = -1°$), with a length and width of 26 μm and 4 μm respectively. Hall measurements with the magnetic field applied perpendicular to the sample plane are shown in and in Fig. 4.8a and Hall measurements with the field parallel to the WTe_2 b-axis (the in-plane magnetic easy axis) are shown in Fig. 4.8b. In Fig. 4.8a, the contribution of the

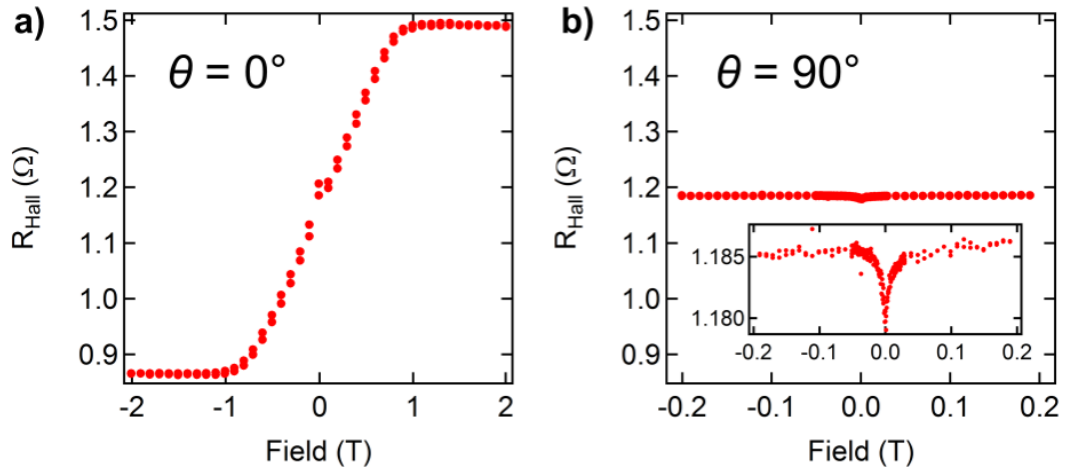

Figure 4.8: Measurements of transverse resistance, R_{Hall}, for a WTe_2/Py(6 nm) Hall bar with the magnetic field oriented perpendicular to the sample plane (**a**) and parallel to the WTe_2 *b*-axis in the sample plane (**b**) with current directed along the WTe_2 *a*-axis. The contribution of the ordinary Hall effect in **a** has been subtracted. The peak-to-peak anomalous Hall effect contribution to R_{Hall}, R_{AHE}, is 0.62 Ω, as extracted from **a**. The inset to **b** shows R_{Hall} versus the applied field along the *b*-axis with an expanded vertical scale. The small variation (0.007 Ω) in **b** is consistent with a planar Hall effect.

ordinary Hall effect has been removed by subtraction of the linear portion of the curve at large fields. Saturation of the Py moment is achieved in out-of-plane fields above 0.9 T and the extracted peak-to-peak value of the anomalous Hall contribution, R_{AHE}, is 0.62 Ω. If there were any tilting of the anisotropy axis out-of-plane, this should give an antisymmetric signal in the *b*-axis scan about zero field. Instead, we observe only a very small, approximately-symmetric Hall signal in Fig. 4.8b ($\approx$ 1% of the saturated anomalous Hall signal). The small signal that we see has an angular dependence (not shown) consistent with a planar Hall effect, and not an out-of-plane tilt. These results show that the overall magnetic anisotropy is in-plane, without any significant out-of-plane tilt of the equilibrium magnetization direction.

4.8.4 Data from additional devices

Device Name	Device Number	t (nm) ± 0.3 nm	$L \times W$ (μm) ± 0.2 μm	τ_B/τ_A	τ_S/τ_A	B_A (0.1 mT)	$\phi_{Easy-I} + 90°$	ϕ_{a-I} ±2°
B11D5	1	5.5	4.8×4	0.373(4)	0.72(1)	70.1(7)	3.4(3)	-5
B13D2	2	15.0	6×4	0.011(7)	0.77(3)	151(2)	84.9(6)	86
B11D3	3	3.1	3.5×4	-0.372(6)	0.84(2)	62(4)	4.2(9)	-3
B12D1	4	5.6	4×4	-0.47(1)	0.74(6)	49(12)	2(3)	-5
B13D1	5	8.2	6×4	0.133(8)	0.99(3)	150(1)	74.7(5)	70
B13D3	6	3.9	6×4	0.372(9)	0.70(3)	98(2)	2.7(7)	-4
B14D3	7	3.4	4×3	0.207(8)	1.20(3)	153(1)	75.1(4)	70
B14D4	8	2.2	4×3	0.385(7)	0.83(3)	74(1)	-0.3(5)	-9
B16D6	9	6.7	5×4	0.278(6)	0.70(2)	173(1)	24.7(5)	19
B14D2	10	2.8	4×3	0.095(8)	1.42(3)	116(2)	80.2(4)	77
B16D7	11	14.0	5×4	-0.13(1)	0.72(4)	138(2)	-58(1)	-56
B16D8	12	5.3	5×4	-0.320(6)	0.70(2)	156(3)	-6.0(3)	-9
B16D10	13	1.8	5×4	-0.045(4)	0.79(2)	172(2)	83.4(4)	82
B16D4	14	5.3	5×4	0.340(7)	0.78(3)	140(1)	-20.9(5)	-25
B16D5	15	5.5	5×4	0.332(7)	0.74(2)	155(1)	-14.8(5)	-16
B16D12	16	3.4	5×4	0.236(8)	1.35(3)	132(1)	29.3(4)	–
B17D8	17	2.6	5×4	0.020(8)	1.50(4)	20(2)	88(2)	–
B17D5	18	5.0	5×4	-0.451(7)	0.83(2)	20(3)	-16(3)	–
B18D1	19	15.0 (S)	5×4	-0.080(6)	0.35(2)	40(2)	6(1)	-1.6
B18D3	20	2.0	5×4	0.74(2)	1.27(5)	31(2)	2.7(9)	–
B18D6	21	5.4 (S)	4×3	0.033(5)	0.64(2)	38(1)	-1.8(6)	3.7
B18D7	22	6.9	5×4	-0.331(6)	0.59(2)	33(2)	-2(1)	–
B18D11	23	9.0	5×4	-0.287(7)	0.49(3)	32(3)	5(1)	–
B18D13	24	0.6	5×4	-0.60(2)	1.46(6)	24(6)	5(4)	–
B19D6	25	6.9 (S)	4×3	-0.240(6)	0.44(3)	44(2)	2.2(0.7)	–
B19D7	26	6.8 (S)	5×4	-0.008(7)	0.51(3)	40(2)	2(1)	–
Pt/Py	Pt/Py	6	10×5	0.000(4)	1.79(2)	42(2)	85.5(8)	–

Table 4.1: Comparison of device parameters, torque ratios, and magnetic anisotropy parameters for WTe_2/Py bilayers discussed in the main text and a Pt/Py control device. Here ϕ_{Easy-I} is the angle of the magnetic easy-axis with respect to the current flow direction, and B_A is the anisotropy field. A label "S" in the thickness column indicates a device with a monolayer step dividing the active region. Devices 17-26 were cleaved under vacuum.

In Table 4.1, we provide device parameters, torque ratios, and magnetic anisotropy parameters for 26 WTe_2/Permalloy bilayers, and a Pt/Permalloy control device. Only the first 15 devices were used for Figs. 4.5a and 4.5b. Devices 1-16 were cleaved in the sputter system load lock while dry nitrogen was flowing, whereas 17-26 were cleaved in the load lock under vacuum (below 10^{-5} Torr). In Fig. 4.9, we plot V_S and V_A as a function of ϕ for four devices, along with fits to $S \sin(2\phi - 2\phi_0)\cos(\phi - \phi_0)$ and $\sin(2\phi - 2\phi_0)[B + A\cos(\phi - \phi_0)]$ for the symmetric and antisymmetric data respectively. The sign of the param-

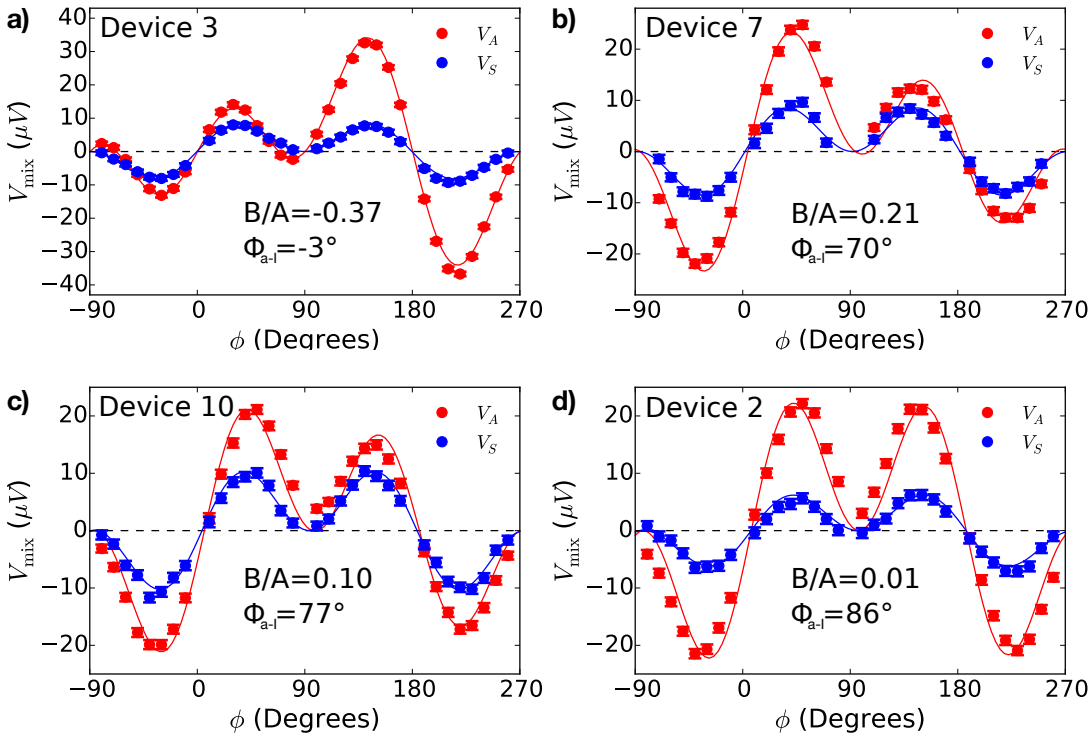

Figure 4.9: Plots of the symmetric (blue circles) and antisymmetric (red circles) components of the ST-FMR mixing voltage for **a)** Device 3, **b)** Device 7, **c)** Device 10, and **d)** Device 2. The current in Device 3 is applied approximately along the *a*-axis of the WTe_2, with the angle turning increasingly toward the b-axis for Devices 7, 10, and 2. The microwave frequency is 9 GHz and the microwave power is 5 dBm. The solid blue lines are fits of $S\sin(2\phi - 2\phi_0)\cos(\phi - \phi_0)$ to $V_S(\phi)$ and the solid red lines are fits of $\sin(2\phi - 2\phi_0)[B + A\cos(\phi - \phi_0)]$ to $V_A(\phi)$. Error bars represent estimated standard deviations from the least-squares fitting procedure.

eter B varies apparently randomly between devices. This is to be expected because Raman scattering does not allow us to distinguish between the $\hat{b}$ and $-\hat{b}$ directions, which are physically distinct for the WTe_2 surface crystal structure (a consequence of broken two-fold rotational symmetry). Essentially, the sign of B depends on whether the positive $\hat{b}$ direction lies along $0^\circ < \phi < 180^\circ$ or $180^\circ < \phi < 360^\circ$. Since interchanging the ground and signal leads rotates the definition of ϕ by 180°, the sign of B is determined by the decision of which end

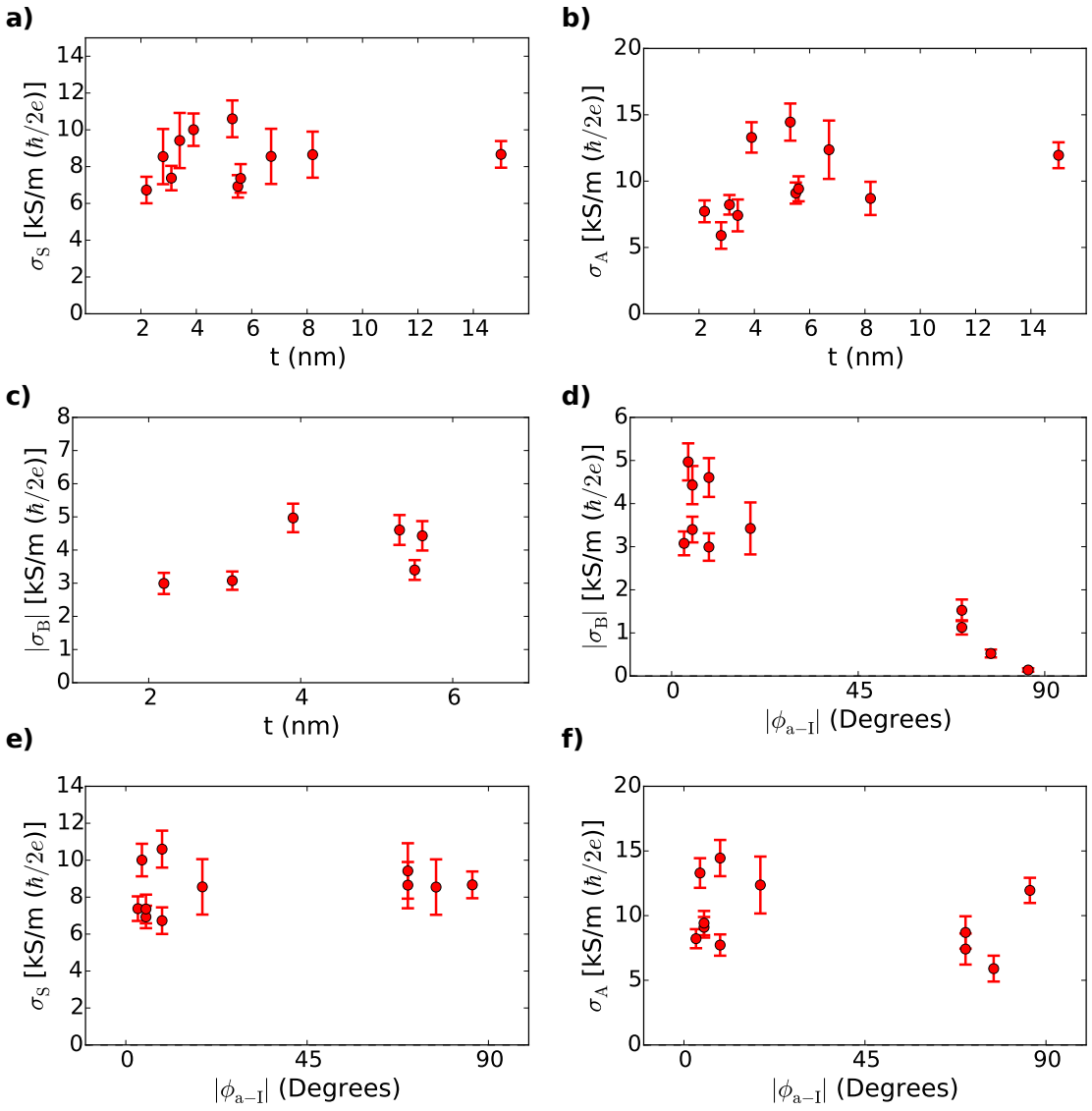

Figure 4.10: **a)** Torque conductivity σ_S as a function of WTe_2 thickness for the 11 devices on which we used a vector network analyzer to perform fully-calibrated measurements. The current is applied at various angles to the WTe_2 a-axis. **b)** Torque conductivity σ_A as a function of WTe_2 thickness for these 11 devices. **c)** Torque conductivity $|\sigma_B|$ as a function of WTe_2 thickness for 6 fully-calibrated devices with $|\phi_{a-I}| < 10°$. **d)** $|\sigma_B|$ as a function of $|\phi_{a-I}|$ for the 11 devices used in panels **a)** and **b)**. **e)** σ_S as a function of $|\phi_{a-I}|$ for the 11 devices used in panels **a)** and **b)**. **f)** σ_A as a function of $|\phi_{a-I}|$ for the 11 devices used in panels **a)** and **b)**. For the data shown in panels **a)-f)**, the applied microwave power is 5 dBm, and the torque conductivities are averaged over the frequency range 8-11 GHz. Error bars represent estimated standard deviations based on error propagation including uncertainties in calibrating the microwave voltage applied across each device and uncertainties derived from least-squares fits to ST-FMR data.

of the bilayer is connected to the signal lead.

We carried out calibrated torque conductivity measurements (using a vector network analyzer to determine I_{RF}) for 11 of our devices. The device-averaged torque conductivities for devices with current applied along the a-axis are reported in the main text. The torque conductivity data from all 11 devices is summarized in Fig. 4.10. In Fig. 4.10a and Fig. 4.10b we plot σ_{S} and σ_{A} respectively as a function of thickness. In Fig. 4.10c we plot $|\sigma_{\mathrm{B}}|$ as a function of thickness for the subset of the 11 devices where current is applied along the a-axis, and in Fig. 4.10d we plot $|\sigma_{\mathrm{B}}|$ as a function of $|\phi_{\mathrm{a-I}}|$ for all 11 devices.

4.8.5 Symmetry analysis for current generated torques

The torques acting on an in-plane magnetization can be written as $\boldsymbol{\tau}_{\parallel}(\hat{m}, E) = \tau_{\parallel}(\phi, E)\hat{m} \times \hat{c}$ and $\boldsymbol{\tau}_{\perp}(\hat{m}, E) = \tau_{\perp}(\phi, E)\hat{c}$, where we have explicitly included the dependence of the torques on the electric field, E, in the bilayer. These expressions are generic, since $\hat{m} \times \hat{c}$ and $\hat{c}$ are unit vectors forming a basis for the vectors perpendicular to $\hat{m}$. The pre-factors, $\tau_{\parallel}(\phi, E)$ and $\tau_{\perp}(\phi, E)$, can be Fourier expanded:

$$\begin{aligned}\tau_{\parallel}(\phi, E) &= E\left(S_0 + S_1 \cos\phi + S_2 \sin\phi + S_3 \cos 2\phi + S_4 \sin 2\phi + S_5 \cos 3\phi + \ldots\right) \\ \tau_{\perp}(\phi, E) &= E\left(A_0 + A_1 \cos\phi + A_2 \sin\phi + A_3 \cos 2\phi + A_4 \sin 2\phi + A_5 \cos 3\phi + \ldots\right)\end{aligned} \tag{4.10}$$

First, we consider the case of an electric field applied along the WTe_2 crystal a-axis. In this case, applying the $\sigma_v\,(bc)$ symmetry operation to the device flips the direction of the electric field (since $\boldsymbol{E}$ is a vector perpendicular to the bc plane) and reverses the component of the magnetization perpendicular to the a-axis (since $\hat{m}$ is a pseudovector). This is equivalent to the transformations $\phi \to -\phi$ and $E \to -E$.

The torques must also transform as pseudovectors under $\sigma_v\,(bc)$, which constrains the dependence of $\tau_\parallel(\phi, E)$ and $\tau_\perp(\phi, E)$ on ϕ and E. The nature of these constraints can be understood by re-writing $\tau_\perp\,(\phi, E) = \hat{c} \cdot \boldsymbol{\tau}_\perp$ and $\tau_\parallel\,(\phi, E) = (\hat{m}\times\hat{c})\cdot\boldsymbol{\tau}_\perp$. Since $\hat{c}$ is a vector and $\boldsymbol{\tau}_\perp$ is a pseudovector, $\hat{c}\cdot\boldsymbol{\tau}_\perp$ transforms as a pseudoscalar (i.e. changes sign under inversion and mirror operations but is invariant under rotations) as the dot product of a vector and a pseudovector is a pseudoscalar. Consistency of the transformations $\phi \to -\phi$, $E \to -E$, and $\hat{c} \cdot \boldsymbol{\tau}_\perp \to -\hat{c} \cdot \boldsymbol{\tau}_\perp$ under $\sigma_v\,(bc)$ then requires that $\tau_\perp\,(-\phi, -E) = -\hat{c} \cdot \boldsymbol{\tau}_\perp = -\tau_\perp\,(\phi, E)$. One can also show that the cross product of a vector and a pseudovector transforms as a vector, and so $\hat{m}\times\hat{c}$ is a vector. This implies that $(\hat{m}\times\hat{c})\cdot\boldsymbol{\tau}_\perp$ transforms as a pseudoscalar so that $(\hat{m} \times \hat{c}) \cdot \boldsymbol{\tau}_\perp \to -(\hat{m} \times \hat{c}) \cdot \boldsymbol{\tau}_\perp$ under $\sigma_v\,(bc)$, and therefore $\tau_\parallel\,(-\phi, -E) = -\tau_\parallel\,(\phi, E)$. We have considered only torques linear in E so that the symmetry requirement becomes $\tau_{\parallel(\perp)}\,(-\phi, E) = \tau_{\parallel(\perp)}\,(\phi, E)$. Keeping only the terms in Eq. 4.10 that comply with this symmetry requirement leaves

$$\begin{aligned}\tau^a_\parallel\,(\phi, E) &= E\,(S_0 + S_1\cos\phi + S_3\cos 2\phi + S_5\cos 3\phi + \ldots)\\ \tau^a_\perp\,(\phi, E) &= E\,(A_0 + A_1\cos\phi + A_3\cos 2\phi + A_5\cos 3\phi + \ldots)\,.\end{aligned} \tag{4.11}$$

The measured angular dependence discussed in the main text for $\boldsymbol{E}$ along the a-axis can be fit accurately with just the low-order terms S_1, A_0, and A_1. Notably, we do not experimentally observe the term S_0, although it is allowed by symmetry.

For an electric field applied along the b-axis, applying $\sigma_v\,(bc)$ to the device flips the projection of the magnetization along the b-axis direction, and leaves the electric field unchanged i.e. $\phi \to \pi - \phi$ and $E \to E$. From this, one can derive the symmetry constraints $\tau_{\parallel(\perp)}\,(\pi - \phi, E) = -\tau_{\parallel(\perp)}\,(\phi, E)$. Therefore the allowed

angular dependencies of the torques for an electric field along the *b*-axis are

$$\begin{aligned}\tau_{\parallel}^{b}(\phi, E) &= E\left(S_1 \cos\phi + S_4 \sin 2\phi + S_5 \cos 3\phi + \ldots\right) \\ \tau_{\perp}^{b}(\phi, E) &= E\left(A_1 \cos\phi + A_4 \sin 2\phi + A_5 \cos 3\phi + \ldots\right).\end{aligned} \tag{4.12}$$

In this case, with $\boldsymbol{E}$ along the b-axis, the lowest order terms (S_1 and A_1) dominate our measurements for both the symmetric and antisymmetric amplitudes, although better agreement is obtained when we include the coefficient A_5 as shown in Fig. 4.11. The expansion for $\boldsymbol{E}$ applied at an arbitrary angle $\phi_{\text{a–E}}$ from the *a*-axis can be determined from the linearity of the torques:

$$\tau_{\parallel(\perp)}(\phi, \boldsymbol{E}) = \tau_{\parallel(\perp)}^{a}(\phi - \phi_{\text{a–E}}, |\boldsymbol{E}|\cos\phi_{\text{a–E}}) + \tau_{\parallel(\perp)}^{b}(\phi - \phi_{\text{a–E}} - \pi/2, -|\boldsymbol{E}|\sin\phi_{\text{a–E}}) \tag{4.13}$$

where $\tau_{\parallel(\perp)}^{a}$ and $\tau_{\parallel(\perp)}^{b}$ are the expansions for electric field along the *a* and *b* axes respectively.

4.8.6 Higher harmonics in the ST-FMR angular dependence

Based on the symmetry analysis in Section 4.8.5, we may expect that the angular dependence of the in- and out-of-plane torques can be more general than $\tau_{\parallel} = S\cos\phi$ and $\tau_{\perp} = A\cos\phi + B$. We examined fits of our data to the most general symmetry-allowed Fourier expansion, up to the third harmonic. We find significant values for A_5 (i.e., the term proportional to $\cos 3\phi$) with the largest magnitudes occurring for current flowing close to the *b*-axis direction. Figure 4.11 shows V_{A} as a function of ϕ for two devices, along with fits to $\sin(2\phi - 2\phi_0)\left[B + A\cos(\phi - \phi_0)\right]$ and $\sin(2\phi - 2\phi_0)\left[B + A\cos(\phi - \phi_0) + C\cos(3\phi - 3\phi_0)\right]$; the $\cos 3\phi$ term significantly improves the fit, corresponding to a non-zero value of A_5. We also find significant values for S_5 of a similar magnitude. For our Pt/Py control device

$S_5/A_1 = -0.10 \pm 0.02$ and $A_5/A_1 = -0.077 \pm 0.008$. All other coefficients up to the third harmonic – except for A_0, A_1, and S_1 – are zero within our experimental uncertainty.

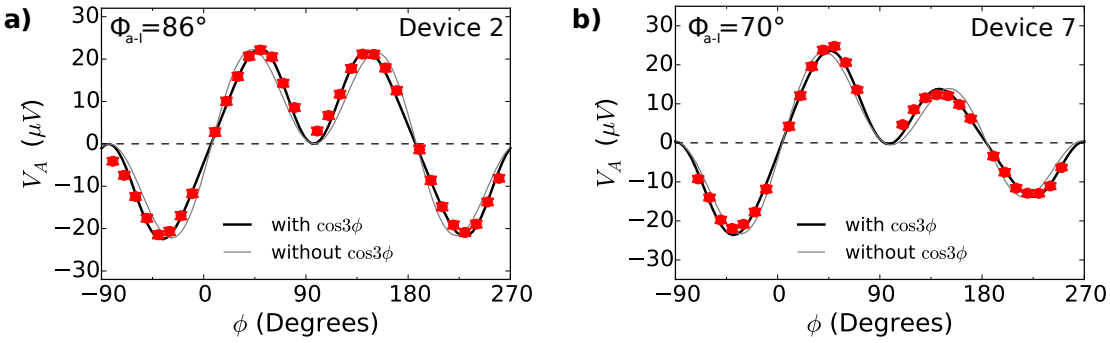

Figure 4.11: Plots of the antisymmetric part of the mixing voltage (red circles) versus the in-plane magnetization angle for **a)** Device 2 and **b)** Device 7. The microwave frequency is 9 GHz and the microwave power is 5 dBm. The black lines show fits to $\sin(2\phi - 2\phi_0)\,[B + A\cos(\phi - \phi_0) + C\cos(3\phi - 3\phi_0)]$ giving $C/A = 0.24 \pm 0.01$ for Device 2 and $C/A = 0.20 \pm 0.01$ for Device 7. The light grey lines show fits to $\sin(2\phi - 2\phi_0)\,[B + A\cos(\phi - \phi_0)]$. Error bars represent estimated standard deviations from the least-squares fitting procedure.

The $\cos 3\phi$ term might arise either from a true angular dependence of the torque or from a lack of full saturation for the in-plane anisotropic magnetoresistance $R(\phi)$ due to in-plane magnetic anisotropy. Our initial analyses suggest that this in-plane anisotropy can account at least partially, but perhaps not completely, for our measured $\cos 3\phi$ term. This mechanism cannot affect our determination of the τ_B torque.

4.8.7 On why there can be no contribution to the out-of-plane antidamping torque from the bulk of a WTe_2 layer

Bulk crystals of WTe_2 have a screw symmetry: the crystal structure is mapped onto itself if it is rotated by 180° about an axis normal to the layers (c-axis) and translated by half a unit cell along both the c and a-axis (in the c direction, half a unit cell is one layer spacing). If there is any net bulk spin polarization or spin current with a component perpendicular to the plane, that spin component will be left unaltered by this operation, while the direction of an in-plane charge current will be reversed. This implies that there can be no bulk contribution to the current-induced antidamping spin torque that is linear in the applied in-plane current. This screw symmetry is broken at the WTe_2/Py interface, so a surface-generated out-of-plane antidamping torque is allowed by symmetry. This surface contribution might come entirely from a single WTe_2 layer at the interface or from imperfect cancellations between more than one WTe_2 layer near the interface (e.g., if there is surface-induced band banding).

We have checked that adjacent layers generate τ_B of opposite sign by studying a sample (Device S1) in which the sample region contains a single-layer step, so that the Permalloy is exposed to two WTe_2 surfaces with opposite symmetry (Fig. 4.12). Device S1 was fabricated with the bar aligned at 3.7° from the a-axis and with a monolayer step dividing the channel into two regions of approximately equal area, as shown by the atomic force microscopy data in Figs. 4.12a and 4.12b. The angular dependences of V_S and V_A are shown in Fig. 4.12c. The non-zero value of V_S implies the existence of spin-orbit torque and a clean WTe_2/Py interface. However, we measure $B/A = 0.033$ for this device, in contrast to our finding that $|B/A| > 0.32$ for all devices measured with $|\phi_{a-I}| < 10°$

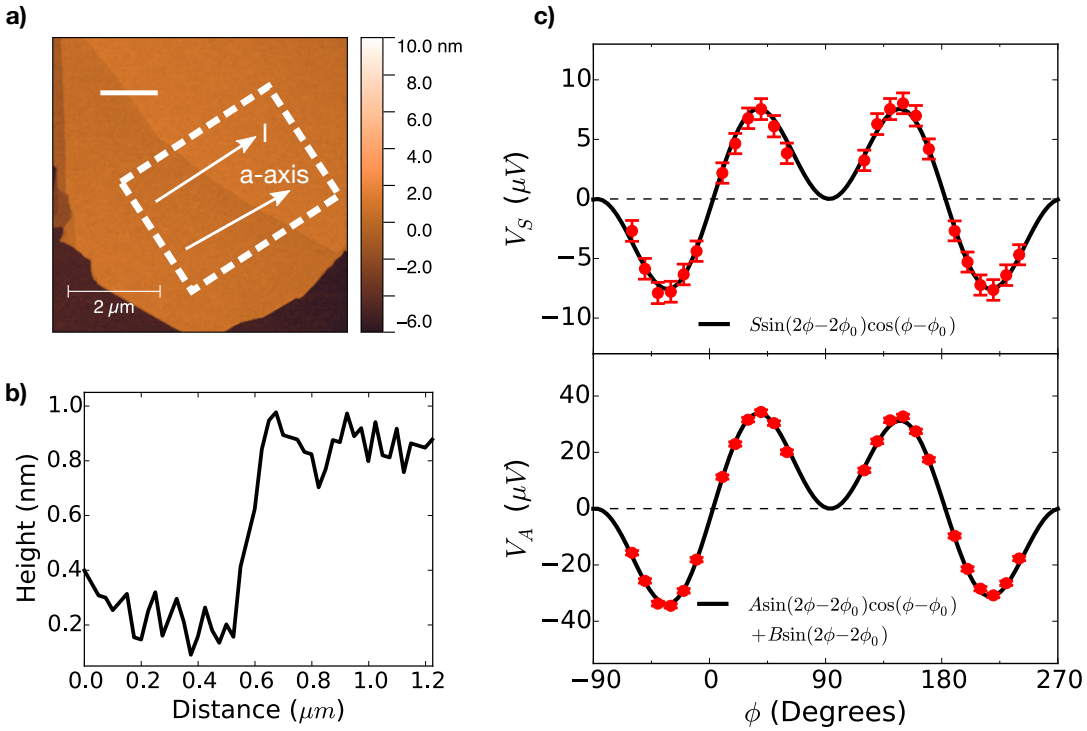

Figure 4.12: **a)** An atomic force microscopy image of the WTe_2 flake used for fabrication of Device S1 after deposition of the Permalloy layer and aluminum oxide cap. The dashed white rectangle shows the approximate placement of the device active region (the uncertainty in the lateral location is about 500 nm due to the alignment procedure for the lithography steps). **b)** A linecut [white solid line in **a**] showing a step height of about 0.7 nm corresponding to a monolayer step in the WTe_2 crystal. **c)** Plot of the symmetric (top, red circles) and antisymmetric parts (bottom, red circles) of the mixing voltage versus the versus the in-plane magnetization angle. The magnitude of the symmetric part indicates a spin-orbit torque comparable to other *a*-axis aligned WTe_2 devices, but the antisymmetric part shows B/A=0.033 indicating that τ_B is much smaller here than in devices without a monolayer step. Error bars represent estimated standard deviations from the least-squares fitting procedure.

and an atomically flat channel. We interpret this low value of B/A in device S1 as arising from cancellation of the torques from the two WTe_2/Py interface regions of opposite surface symmetry, providing strong evidence that τ_B arises from an interface effect. Similar results were obtained on two additional devices con-

taining a monolayer step and with the bar direction aligned to the WTe_2 *a*-axis.

4.8.8 Some comments on the microscopic origin of an out-of-plane antidamping torque in WTe_2/Py bilayers

In this section, we discuss a few possible microscopic mechanisms for generation of out-of-plane antidamping torques, with the understanding that these possibilities are not exhaustive. We focus on mechanisms that can generate transport and accumulation of spins polarized in the *c*-direction, since absorption of *c*-axis polarized spins is expected to lead to a $\hat{m} \times (\hat{m} \times \hat{c})$ torque. To start, we show that symmetry constraints forbid a nonzero contribution from two well-known effects generating spin-orbit torques: a bulk spin-Hall conductivity, and a bulk-averaged inverse spin galvanic effect. We then consider possible mechanisms for which non-zero contributions are allowed.

To generate a $\hat{m} \times (\hat{m} \times \hat{c})$ torque via the bulk spin-Hall effect, we must have *c*-axis polarized spins flowing towards the WTe_2/Py interface in response to an in-plane electric field. The total current of *c*-axis polarized spins, $\boldsymbol{j}_s^c$, can be written as $\boldsymbol{j}_s^c = \sigma^c \cdot \boldsymbol{E}$, where σ^c is the *c*-axis polarized part of the spin-Hall conductivity tensor. The form of this tensor is constrained by the point group of the crystal [133]. For the *mm*2 point group operations of WTe_2, the most general form is:

$$\sigma^c = \begin{pmatrix} 0 & \sigma_{ab}^c & 0 \\ \sigma_{ba}^c & 0 & 0 \\ 0 & 0 & 0 \end{pmatrix}. \tag{4.14}$$

Notably, the terms σ_{ca}^c and σ_{cb}^c, corresponding to *c*-axis polarized spins flowing

in the c-direction (towards the WTe_2/Py interface) in response to in-plane electric fields, are zero. Therefore, there can be no contribution to a $\hat{m}\times(\hat{m}\times\hat{c})$ torque from the bulk spin Hall effect in WTe_2.

When an electric field is applied to a non-centrosymmetric crystal we expect a non-equilibrium spin-density to be generated in the crystal due to the inverse spin galvanic effect. This spin polarization can also be written in terms of a linear response tensor: $\boldsymbol{s} = \chi \cdot \boldsymbol{E}$. The tensor χ must satisfy the relation $\chi = \det(S)S^{-1}\chi S$ for any symmetry operation S in the point group of the crystal [134]. The point group rather than the space group is relevant here because we assume the spin density to have a nonzero component that is spatially uniform. For WTe_2, the most general form is:

$$\chi = \begin{pmatrix} 0 & \chi_{ab} & 0 \\ \chi_{ba} & 0 & 0 \\ 0 & 0 & 0 \end{pmatrix}. \tag{4.15}$$

Since χ_{cb} and χ_{ca} are zero, the bulk inverse spin galvanic effect of WTe_2 cannot generate a $\hat{m}\times(\hat{m}\times\hat{c})$ torque.

The symmetry of WTe_2 does, however, allow for local accumulations of c-axis polarized spins in response to an in-plane electric field, provided these accumulations switch sign between atomic sites related by the screw-axis and glide-plane symmetries. This is similar to recent work on CuMnAs, where the absence of local inversion symmetry allows for current-induced exchange fields that change sign between atomic sites related by the global inversion symmetry [113]. The WTe_2 crystal can be partitioned into adjacent A and B type layers, where B layers are rotated by 180° with respect to A layers. The symmorphic bc mirror plane maps every layer back onto itself, while the non-symmorphic

symmetries (screw-axis and glide-plane) map each layer onto an adjacent one of the opposite type. If we define layer specific spin accumulations $\boldsymbol{s}^A = \chi^A \boldsymbol{E}$ and $\boldsymbol{s}^B = \chi^B \boldsymbol{E}$, the respective tensors obey:

$$\chi^A = \begin{pmatrix} 0 & \chi^A{}_{ab} & \chi^A{}_{ac} \\ \chi^A{}_{ba} & 0 & 0 \\ \chi^A{}_{ca} & 0 & 0 \end{pmatrix}, \chi^B = \begin{pmatrix} 0 & \chi^A{}_{ab} & -\chi^A{}_{ac} \\ \chi^A{}_{ba} & 0 & 0 \\ -\chi^A{}_{ca} & 0 & 0 \end{pmatrix}. \tag{4.16}$$

Therefore, it is possible to generate local c-axis spin polarizations in the bulk WTe_2 crystal via an in-plane current, but the local c-axis spin polarizations change sign between layers. In a real crystal the surface will terminate on either an A or B type layer, leading to a c-axis spin polarization on the surface when current is applied along the a-axis. This mechanism is expected to lead to a $\hat{m} \times (\hat{m} \times \hat{c})$ torque, along with a $\hat{m} \times \hat{c}$ torque due to exchange coupling of the ferromagnet to the WTe_2 surface spins.

Another approach is to consider the torques generated in an interface layer formed by hybridization between electronic states of the WTe_2 and Py i.e. in a region at the WTe_2/Py interface with electronic properties differing from the bulk of either layer. These interface states could generate c-axis polarized spin accumulations via the inverse spin galvanic effect. For example, the spin-orbit coupling Hamiltonian $H_{\mathrm{SOC}} \propto \hat{n} \cdot (\boldsymbol{k} \times \boldsymbol{\sigma})$, where $\hat{n}$ lies in the bc plane, is consistent with the symmetry of the WTe_2/Py interface, and leads to a non-zero $\langle \sigma_c \rangle$ in response to electric fields applied along the a-axis. This is a generalization of the usual Rashba-Edelstein effect discussed in the context heavy metal/ferromagnet bilayers, which corresponds to $\hat{n} = \hat{z}$. Such a $\langle \sigma_c \rangle$ can generate both $\hat{m} \times (\hat{m} \times \hat{c})$ and $\hat{m} \times \hat{c}$ torques, with their relative magnitude depending on microscopic details. Magnetic anisotropy associated with this mechanism has been predicted to arise at the interface between ferromagnets and low-

symmetry materials with strong spin-orbit coupling [135].

Recent theoretical work suggests that it may also be possible that the spin-polarized electrons flowing within a metallic ferromagnet layer may generate spin-transfer torque when they scatter from an interface with a material possessing strong spin-orbit coupling, without necessarily requiring charge current flow within the spin-orbit material [136, 137]. This mechanism is attractive because it might provide a natural explanation for the apparent lack of dependence on the WTe_2 thickness for any of the torque components τ_B, τ_A, and τ_S.

4.8.9 Second-harmonic Hall measurements

Second-harmonic measurements of Hall voltage as a function of the angle of an in-plane applied magnetic field, B, provide an alternative method to measure an out-of-plane antidamping torque independent of ST-FMR measurements. We performed this measurement using a Hall bar device discussed in Section 4.8.3, for which the Permalloy thickness is 6 nm and the WTe_2 thickness is 16 nm. The Hall bar has a length and width of 26 μm and 4 μm, respectively, and is oriented so that the current is along the WTe_2 a-axis ($\phi_{a-I} = -1$); the voltage probes used for the Hall measurements are 2 μm wide. The active region of the Hall bar has a uniform WTe_2 thickness, with no monolayer steps, over better than 90% of its area. We apply a current $I(t) = I_0 \sin(2\pi f t)$ at a frequency $f = 340$ Hz with $I_0 = 0.66$ mA, and measure the Hall voltage at the second harmonic frequency. The angle of the in-plane magnetic field, ϕ, is defined relative to the direction of current flow. Generalizing the argument in Ref. [138] to include the effects of an in-plane uniaxial anisotropy B_A with the easy axis parallel to the

b-axis of the WTe_2 (in addition to the shape anisotropy of the thin film $\mu_0 M_{\text{eff}}$), and allowing for in-plane and out-of-plane current-induced torques with the angular dependence $\tau_{\parallel} = \tau_S \cos\phi_M$ and $\tau_{\perp} = \tau_A \cos\phi_M + \tau_B$, the second harmonic signal has the form:

$$R_{xy}^{2\omega} = \frac{R_{\text{PHE}} \cos 2\phi_M \left(\tau_A \cos\phi_M + \tau_B\right)}{\gamma \left(B - B_A \cos 2\phi_M\right)} + \frac{R_{\text{AHE}} \tau_S \cos\phi_M}{2\gamma \left(B + \mu_0 M_{\text{eff}} + B_A \sin^2\phi_M\right)} + \frac{V_{\text{ANE}}}{I_0} \cos\phi_M, \tag{4.17}$$

where R_{PHE} and R_{AHE} are the planar and anomalous Hall resistances of the device, and V_{ANE} is the anomalous Nernst voltage arising from an out-of-plane thermal gradient proportional to the Joule power I^2R. This expression neglects terms above first order in B_A/B, which is an accurate approximation over the range of fields studied for our second harmonic measurements. Here ϕ_M is the angle of the magnetization relative to the direction of current flow, which differs from ϕ for low-fields due to the in-plane magnetic anisotropy. To first order in B_A/B, the equilibrium magnetization angle is $\phi_M = \phi + B_A \sin 2\phi / 2B$. Equation 4.8.9 shows that the second harmonic signal associated with τ_B has an angular dependence distinct from τ_A, τ_S and the magneto-thermopower voltage (V_{ANE}).

Fig. 4.13 shows measurements of the second-harmonic Hall voltage in the WTe_2/Py Hall bar as a function of ϕ for selected magnitudes of applied magnetic field B; the red lines indicate the data, while the black lines are fits to Eq. 4.8.9. Even without any fitting, it is clear that the out-of-plane antidamping torque τ_B is indeed non-zero, as the magnitude of the second-harmonic signal is significantly different for $\phi = 180°$ and $360°$ [when $\tau_B = 0$, Eq. 4.8.9 predicts simply that $R_{xy}^{2\omega}(\phi = 180°) = -R_{xy}^{2\omega}(\phi = 360°)$]. To fit the data, we use a simplified version of Eq. 4.8.9, valid when $B \ll \mu_0 M_{\text{eff}}$:

$$R_{xy}^{2\omega} = \frac{\cos 2\phi_M}{\left(B - B_A \cos 2\phi_M\right)} \left(A_1 \cos\phi_M + A_0\right) + R_{\phi} \cos\phi_M, \tag{4.18}$$

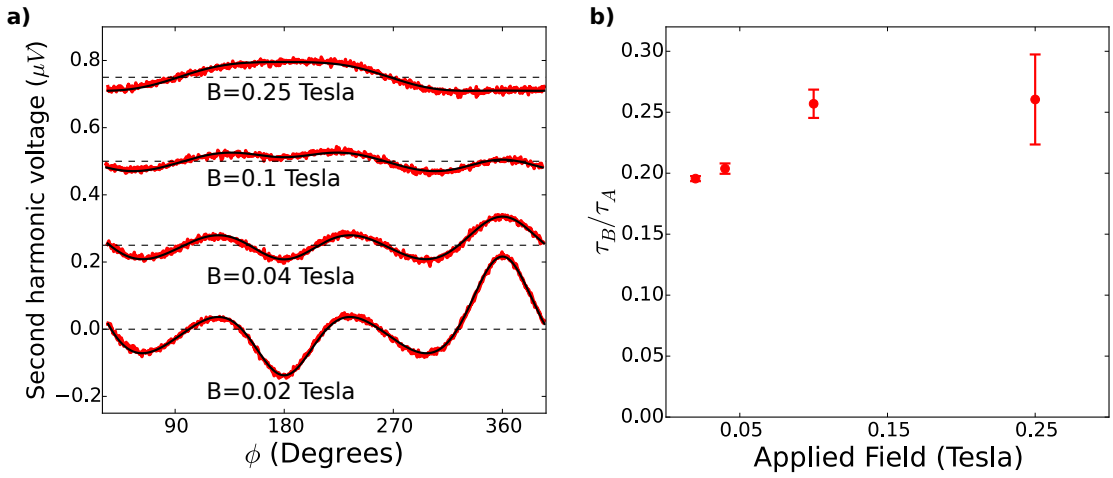

Figure 4.13: **a)** Second harmonic Hall voltage for a WTe_2/Py bilayer (with current along the a-axis) as a function of the angle between the in-plane applied magnetic field and the current flow direction. The data (red) are plotted for different magnitudes of the applied magnetic field (B=0.25 T, 0.1 T, 0.04 T, and 0.02 T, from top to bottom). Data for different values of the applied field have been vertically offset for clarity. The black lines show fits to Eq. 4.8.9. **b)** The torque ratio τ_B/τ_A extracted from the angular dependence of the second harmonic Hall voltage, as a function of the magnitude of the applied magnetic field used for the angular sweep. Error bars represent estimated standard deviations from the least-squares fitting procedure.

where $A_0 = R_{\mathrm{PHE}}\tau_B/\gamma$, $A_1 = R_{\mathrm{PHE}}\tau_A/\gamma$, and R_ϕ is a constant combining the contributions of the in-plane antidamping torque and the anomalous Nernst voltage. For each value of B we fit the data using the parameters A_0, A_1, R_ϕ, and B_A, along with an additional overall ϕ-independent offset. For the fits, we used the first-order expression for $\phi_M(\phi)$ discussed above. We find that Eq. 4.8.9 fits the data well with $B_A \approx 3mT$. The torque ratio τ_B/τ_A can then be determined independent of any other sample parameters at each value of the field magnitude, $A_0/A_1 = \tau_B/\tau_A$. In figure 4.13b we plot τ_B/τ_A as a function of B, showing that $\tau_B/\tau_A \approx 0.2-0.25$. These values are similar to, albeit slightly lower than, the values of $|\tau_B|/\tau_A$ determined by ST-FMR for different devices ($|\tau_B|/\tau_A = 0.32-0.385$; see Fig. 4.9 or Table 4.1).

We determine the individual torque conductivities σ_A and σ_B from the second harmonic Hall measurements according to (here the subscript $K = A$ or B):

$$\sigma_K = \frac{M_s l w t_{magnet}}{\hbar\gamma/2e} \frac{\tau_K}{(lw)\,E} \left(\frac{\hbar}{2e}\right) = \frac{e M_s l t_{magnet}}{\mu_B} \frac{\tau_K}{V} \left(\frac{\hbar}{2e}\right). \tag{4.19}$$

Using $R_{PHE} = 0.14\ \Omega$, for the harmonic Hall measurement with $B = 1000$ Oe we find $\tau_A = 8.3 \pm 0.2$ MHz and $\tau_B = 2.12 \pm 0.09$ MHz. To estimate the applied electric field we divide the applied voltage (566 mV peak-to-peak) by the length of the Hall device, and to estimate the saturation magnetization $M_s \approx M_{eff}$ we fit to the anomalous Hall effect data of Fig. 4.8 finding $\mu_0 M_{eff} = 0.81$ T $\pm$ 0.01 T. From Eq. 4.19 we then find $\sigma_B = (6\pm1)\times10^3(\hbar/2e)(\Omega m)^{-1}$ and $\sigma_A = (25 \pm 4) \times 10^3(\hbar/2e)(\Omega m)^{-1}$, where the errors are primarily due to the uncertainty in the thickness of the Permalloy. These values can be compared with the calibrated ST-FMR measurements presented in Fig. 4.10. The calibrated ST-FMR measurements for devices with $|\phi_{a\text{-}I}| \leqslant 10^\circ$ give a range of $\sigma_B = (3-5)\times10^3(\hbar/2e)(\Omega m)^{-1}$ and $\sigma_A = (8-14)\times10^3(\hbar/2e)(\Omega m)^{-1}$. The second-harmonic value for σ_B agrees with the ST-FMR measurements within the range of reasonable experimental uncertainty. The value of σ_A as determined from the second-harmonic measurements is approximately twice as large as the typical ST-FMR value. This discrepancy in σ_A is not presently understood but there may be differences in the WTe_2 crystal quality or the cleanliness of the WTe_2/Py interface, as the Py film used for the Hall bar device was grown in a different round of sputtering depositions than those used for the ST-FMR devices. We conclude that the second-harmonic Hall measurements confirm the existence of a nonzero out-of-plane antidamping torque τ_B and give a value for its strength in agreement with the ST-FMR measurements.

CHAPTER 5

SAMPLE FABRICATION

In this chapter I will describe the fabrication of micron scale electrical devices involving TMD thin films. In the first section, I will discuss general techniques for preparing such films. In the second I will give a detailed recipe for fabricating WTe_2/Py devices for spin-torque ferromagnetic resonance experiments.

5.1 Basic preparation techniques

Throughout my doctorate, I have had many occasions to create devices containing crystalline transition-metal dichalcogenide thin films. Here, I will collect some observations for preparation of such films using the technique of mechanical exfoliation. Mechanical exfoliation involves cleaving a layered crystal repeatedly with tape, and then sticking the resulting thin layers onto a substrate of choice. The first step of mechanical exfoliation is to prepare a high-quality crystal of the desired material. I have never done this before, instead opting to buy the crystals – typically from HQ graphene.

At the end of the day, there are two basic parameters that can be varied during mechanical exfoliation: the type of tape, and the preparation of the substrate. Thin flakes will be most visible if you use a silicon substrate coated with 90 nm or 300 nm of silicon oxide. For other oxides or substrates, the visibility can be estimated via the method of Refs. [139]. However, it should be possible to find monolayer TMDs on any substrate. I always prepare the substrate by a chemical clean (sonication in acetone and then isopropanol) followed by baking at 300° C on a hot plate. The choice is whether to clean the surface with an

oxygen plasma or not. If this is done, it should probably be a gentle exposure in a clean system, such as the Harrick plasma sterilizer in the Ralph or McEuen labs. Exposure with oxygen plasma immediately prior to exfoliation increases the flake size and number. Flakes deposited in this way are more heavily doped, making it harder to tune the Fermi level electrostatic gating. However, if you plan to remove the flake from the substrate later with a pick-up technique, the doping will not be present in the final device (see [140] for a detailed study).

Now we move to the choice of tape. I have tried two types: regular 3M Scotch tape, and "Pantech UV Dicing Tape," which is a blue tape available near the CNF dicing saw. In either case, the exfoliation technique is the same (see Ref. [4]). Place a piece, or pieces, of crystal onto the tape, and then fold the tape or use other small tapes to cleave and copy it densely onto an approximately 1 cm^2 area. Then, using another tape, copy this dense spot to cover an area the size of your substrate on both tapes. Once these tapes look good, take two clean tapes and stick them onto the crystal covered tapes: mark the new side with a "T" so you can use it in your exfoliation. When the substrates are ready, peel off the newer side and place it onto the substrate. After waiting 30 seconds, you can gently remove the tapes to reveal fresh TMD films on the substrate. As for the difference between blue tape and Scotch tape, blue tape leaves much less reside on the substrate (almost no visible residue) whereas Scotch tape will leave large blobs of residue. On the other hand, Scotch tape seems to produce more and larger TMD flakes, to the extent that I would not recommend using blue tape, except for graphene exfoliation. With proper flake selection, tape residue is not an issue.

To choose flakes, the first step is to find ones that look completely clean in

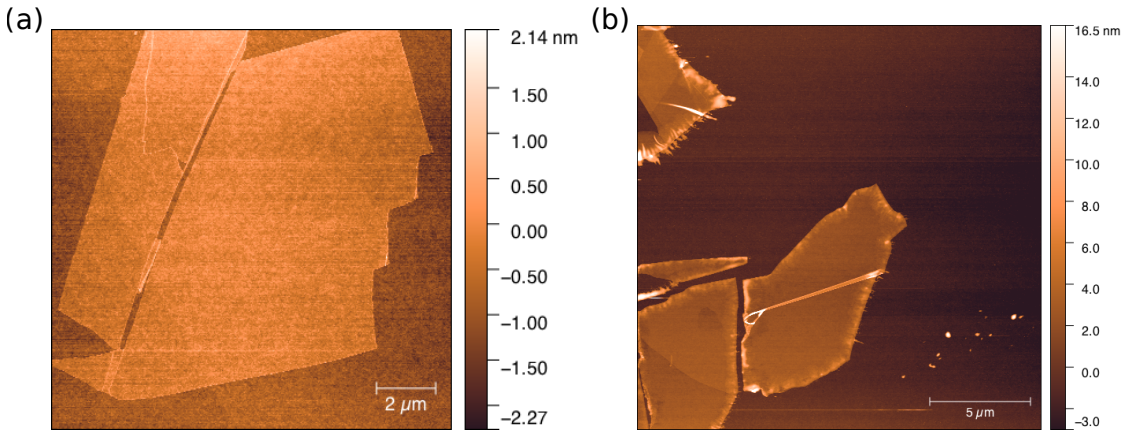

Figure 5.1: **(a)** AFM image of a clean WSe_2 monolayer, prepared via mechanical exfoliation with Scotch tape. **(b)** AFM image of a WSe_2 film, prepared via mechanical exfoliation with Scotch tape. Anomalous features are apparent on the edges of the flake (there is also a folded region visible).

the microscope. A good hint is if they are in a clean patch of bare substrate surrounded by residue; this means they were cleaved off a large crystal that touched down there. I usually mark flakes with a small dot of sharpie ink on the edge of the substrate; the mark indicates one of the in-plane coordinates of the flake, while the other must be scanned again to re-locate the flake. Next, every flake should be examined in the atomic force microscope (AFM). It's probably best to only use ones which are completely clean and atomically flat over a useable region. In Fig. 5.1, I compare AFM data from a clean TMD crystallite with one covered in an unknown (it's tape glue) residue.

In addition to the basic exfoliation techniques described above, there are also techniques for moving flakes between substrates, and for stacking flakes together to create heterostructures. The methods I use rely on using polydimethylsiloxane (PDMS) as a stamp. Thin films of PDMS can be prepared at the CNF PDMS casting station. For one thing, it is possible to exfoliate onto a PDMS block instead of a substrate. This allows one to transfer flakes on that PDMS to

a specific location on any desired substrate. This process is described extremely well in Ref. [141].

I prefer a class of transfer methods called pick-up transfers. The process is described in detail in Refs. [140, 142]. I will only make some comments on preparation of the transfer slide, and specific polymer recipes we have used here which are not described in the references. For the polymer we use Poly(Bisphenol A carbonate), available from Sigma Aldrich. We dissolve this in choloroform at 6 % concentration by weight. Thin films of BPA can be prepared by pipetting a drop of the solution onto a glass slide, then pressing another glass slide on top and sliding it off. Then, make a piece of tape with a hole in it, and use it to peel of a section of the BPA film (leaving a suspended BPA film covering the hole). To finish the stamp, mount the suspended BPA film onto a PDMS block attached to a glass slide. The glass transition and melting temperatures of these BPA films are roughly 70 °C and 140 °C respectively. For pick-up, the polymer should be heated to around the glass transition, and for final release, it should be heated above it's melting temperature. Also, as described in Ref. [140], heating the substrate above 100 ° before finishing an encapsulated stack seems to reduce the amount of bubbles (as does using flakes that look perfectly clean in AFM). After finishing a transfer, I usually leave the stack in a sealed container of chloroform overnight, to remove the melted BPA.

5.2 Fabrication of WTe_2/Py bilayers for spin-torque experiments

WTe_2 is a semi-metallic TMD crystallizing in a distorted version of the octahedral phase. The strong spin-orbit coupling and low-symmetry crystal structure of WTe_2 make it interesting as a spin source, capable of generating spin currents when an electric field is applied. These topics are covered in chapter 4. In this section, I will provide an explicit recipe to prepare WTe_2/Py bilayer devices for ST-FMR experiments. Keep in mind that this recipe was evolved over time, and adheres to the philosophy of, "if it ain't broke, don't fix it." Many aspects can likely be improved.

5.2.1 Exfoliation

The substrates and WTe_2 tapes are prepared as in Section 5.1. We use silicon wafers with resistivity over 10000 Ω·cm, to avoid microwave absorption in the substrate. Unlike $MoSe_2$, WTe_2 reacts with oxygen under ambient conditions. Therefore, we want to deposit the Permalloy onto the WTe_2 without significant air exposure of the WTe_2 surface. There are two ways I do this. I both cases, I start by attaching pieces of the substrate to the platen of the sputter system, using Kapton tape. Then, I separate the two sides of the WTe_2 tape, and place the "T" side (the fresher tape, see Section 5.1) onto the substrate. The difference between methods lies in how and when the tape is removed from the substrate.

In one method, I load the platen onto the transfer arm in the loadlock, while flushing the loadlock with nitrogen from the vent line. Then, I quickly remove

the tapes from the substrate and close the loadlock door. Clearly there will be some air exposure in this procedure, but the hope is that it is sufficiently low to prevent total oxidation of the WTe_2 surface.

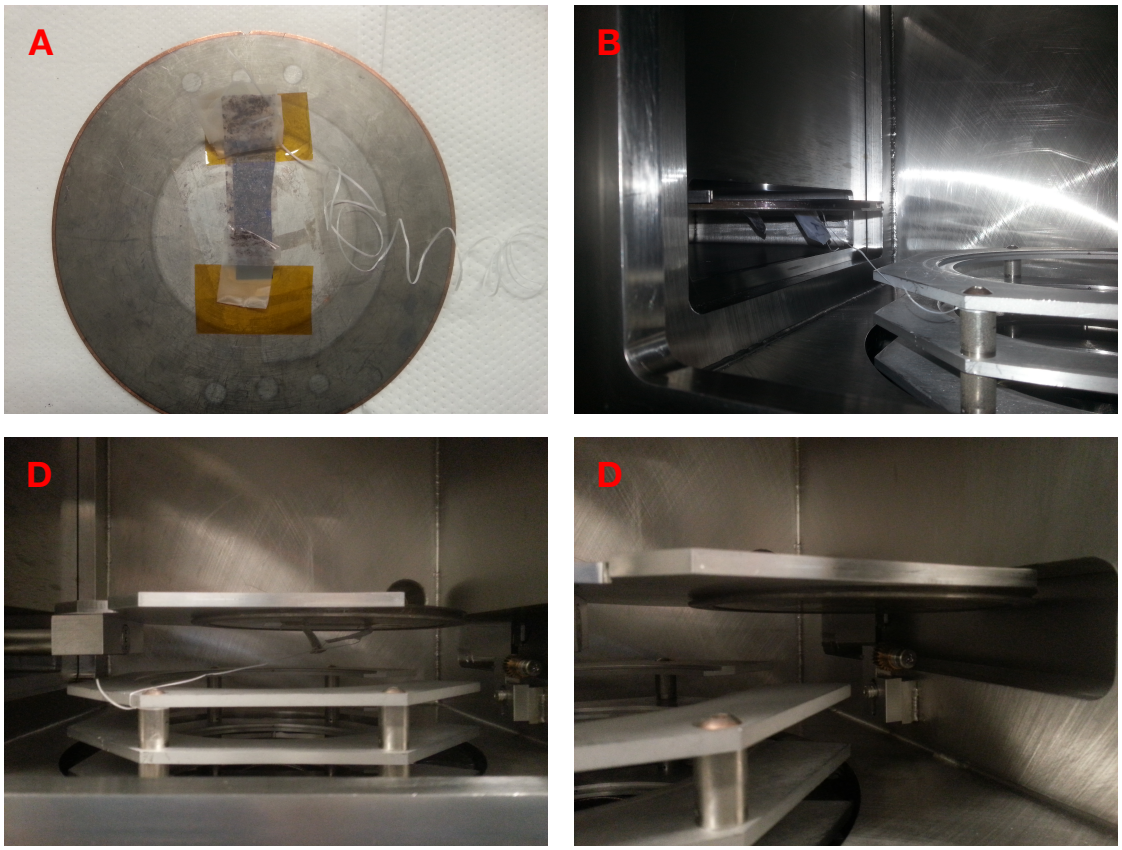

Figure 5.2: **A** Geometry for attaching the substrate to the platen and floss to the tape. The floss is threaded through a hole in the tape, and then another piece of tape is wrapped around it to prevent tearing. **B** Geometry for tying the floss to the cassette. **C** Moving the arm forward begins to peel off the tape. **D** Position when the tape is fully peeled off. Note that the platen has not yet reached the isolation valve.

The second method nominally provides much less air exposure. In this method, I attach dental floss to the end of the tape after it is attached to the substrate on the platen, as shown in Fig. 5.2b. Make sure to wrap the part that is pierced by the floss with another piece of tape, for structural support. Then load the platen into the transfer arm in the loadlock, and tie the floss to the cas-

sette holder (see Fig. 5.2 for the geometry). Make sure it is taut! Then, close the door and pump down the loadlock to the desired pressure. I always wait until it is well below 10^{-5} Torr. Once you are ready to sputter, open the process chamber isolation valve, and gently push the transfer arm towards the chamber, as is normally done when transferring samples into the process chamber. If the floss was short enough, it should pull the tapes of the substrates just before the end of the platen is entering the isolation valve. If the tapes have not come off before the platen reaches the isolation valve, you may want to stop and redo the setup with shorter floss. If any tape, floss, or piece of substrate, ends up on the isolation valve, the chamber will need to be vented via a special procedure that involves defeating the isolation valve interlock (ask the tool manager, but try to avoid this situation).

5.2.2 Permalloy deposition

We deposit the permalloy using a 2″ TORUS magnetron sputtering gun from Kurt J. Lesker. This gun is not normally installed in the chamber, since it prevents use of the 3″ gun with extra strength magnets and also raises the chamber base-pressure significantly (from about 10^{-9} Torr to 10^{-8} Torr). To install it, the 8″ viewport is removed and replaced with the mating flange for the gun. This results in the gun lying at less than 15° from the substrate holder plane, allowing grazing angle sputtering. Grazing angle sputtering is desirable, since prior studies have shown that it results in less damage to the sample surface than normal incidence sputtering [143]. The permalloy deposition rates are kept below 0.2 Å/s and are performed in an ambient Ar background pressure of 4 mTorr while the substrate rotates at 3 rotations per minute. We also deposit a protec-

tive aluminum oxide cap in situ onto the WTe_2/Py bilayer by sputter deposition of 1 nm aluminum, which is subsequently oxidized in a dry N_2/O_2 mixture.

5.2.3 Flake selection

Flakes should be identified using an optical microscope after the permalloy deposition. For thinner flakes (below about 10-15 nm) it should be possible to ascertain the presence of even monolayer steps using the difference in optical contrast across a step. In all cases, AFM should be carried out to determine the roughness, homogeneity, and cleanliness of the flakes. Typically, the RMS surface roughness of a clean WTe_2/Py bilayer should be less than 300 pm. The presence of monolayer steps will significantly affect device performance (see Section 4.8.7), and precision measurements of the sample topography must be made before any fabrication. You will *not* be able to extract this information from the finished devices. Furthermore, the sample will appear much rougher, and the AFM data noisier, if the sample has *even once* been coated in PMMA.

5.2.4 Defining and depositing alignment marks

The alignment marks are defined via e-beam lithography. I use the NPGS system hooked up to the Supra SEM at CNF. The procedures for operating a system can be found in the NPGS manual. Here I will provide some details of operation specific to our system and this process. First, the resist recipe:

1. Spin PMMA 50K A8 at 3000 RPM

2. Bake for 2 minutes on a hotplate at 170°
3. Spin PMMA 950K A4 at 3000 RPM
4. Bake for 2 minutes on a hotplate at 170°

I am using very thick PMMA here to help lift-off thick sputtered films. I don't recommend this recipe for small (sub 500 nm) features, although I have been able to pattern 300 nm wires using it. After spinning the resist, you need to find the flakes again, and scratch the PMMA near the flake with tweezers. Don't put the mark *too* close. The ultimate limit is that it shouldn't overlap with the device-to-be-fabricated. I recommend being able to see the flake and the end of the scratch in a 5 or 10X objective, but not in the 20X. Once the scratch is made, save an image at the highest resolution where you can see both the flake and part of the scratch. Please note the image settings e.g. if there is any binning in the CCD; you will need to know the number of pixels per micron.

Next, I use the NPGS system to write alignment marks around the flake. The shape of the marks isn't too important, they just need to be consistent between fabrication steps. To find the flake, I first find the scratch. Then, using the optical microscope image, I calculate the stage displacement required to center the flake in the field of view. Then I blank the beam, and move the stage so that the field of view is centered on the correct point. The marks can then be exposed using the normal method for an unaligned e-beam exposure. After exposure, the resist is developed in 3:1 mixture of isopropanol and methyl isobutyl ketone for 60 seconds, followed by a rinse in pure isopropanol. I then deposit 5 nm of Titanium and 75 nm of Platinum using the CNF AJA sputter system. If much thinner marks are deposited, they will not survive subsequent etch steps. After metal deposition, I place the samples in acetone for lift-off.

One the alignment marks are done, take an image of the marks and flakes in an optical microscope. This image can be loaded into a CAD program to assist in designing the shape of the ST-FMR bar and contacts. If better resolution is required, the optical image can be merged with an AFM image before loading into the CAD software.

5.2.5 Defining the ST-FMR bars

After designing the device, the next step is to etch away the unwanted permalloy and WTe_2 that covers the substrate. During this etching, the device region must be covered by a mask. We have experimented with many mask materials, and eventually settled on a silicon oxide hard mask as the best choice. While other hard masks can probably be used, we encountered many problems when trying to use resist masks e.g. a HSQ/PMMA bilayer recipe. The problems seem to occur during during the removal of the resist mask: we found that after this step many devices would become folded up (Fig. 5.3a), or show signs of chemical reaction (Fig. 5.3b). The use of hard masks solves this problem by obviating the mask removal step (part of the mask remains on the completed device).

The procedure for defining the bars using a silicon oxide hard mask is as follows:

1. Spin a PMMA 50K/PMMA 950K bilayer as described above.
2. Use e-beam lithography to open a window in the resist in the shape of the bar.
3. Evaporate 60 nm of silicon oxide onto the sample. Lift-off to finish the etch

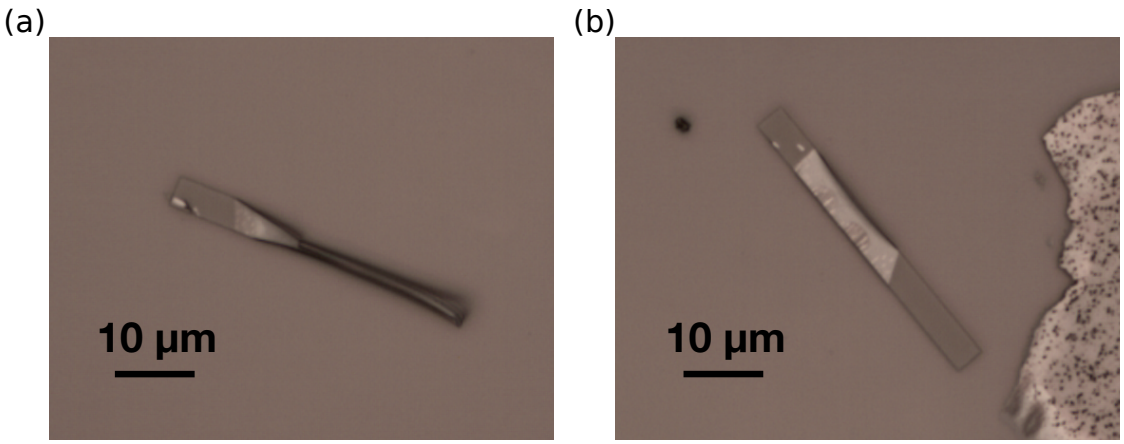

Figure 5.3: **(a)** Optical micrograph of a WTe_2/Py bilayer that has delaminated and folded after etch-mask-removal. **(b)** Optical micrograph of a WTe_2/Py bilayer that has appears to have chemically degraded (white spots) after etch mask removal.

mask.

4. Etch the samples in the Buhrman group Ion mill. The total exposure time is 9 minutes. This is done in 36 cycles comprising 15 s of etching and 30 s with the beam blanked. The etch rate is roughly 4.5 nm/min.

Once the bars are done, it is important to cap them by sputtering 20 nm of silicon oxide in the CNF AJA. While WTe_2 seems to adhere well to silicon oxide, for every other TMD we have see delamination during resist spins. The solution is to sputter 5 nm of silicon oxide before doing any fab (i.e. before putting down the alignment marks), and then to add one minute to the total ion mill etch time.

5.2.6 Defining and depositing contacts

To start, spin the PMMA 50K/PMMA 950K bilayer described in Sections 5.2.4 and 5.2.5, with one important modification: spin the 950K layer at 2000 RPM.

Then, use e-beam lithography to open the contact regions. The disadvantage of using a hard-mask is it must be removed from the contact region before metal deposition. The recipe is as follows:

1. Check that the CNF AJA is available immediately after your etch is done (so you can quickly load the samples after etching).
2. Load the sample in the Oxford 81 Reactive Ion Etcher.
3. Run the oxygen plasma for 5 s, using the standard recipe. This is to clean resist residue.
4. Run the CHF_3/Ar oxide etch recipe for 2 m and 15 s. This etches the silicon oxide. The calibrated rate is 29.4 nm/min, so this is an over-etch.
5. Run the oxygen plasma for 9 s. This is to remove etch byproducts.
6. Remove the sample from the etcher.
7. Dip the sample in AZ 726 MIF for 15 s. This is a photoresist developer that contains 2.38 % TMAH in water with some additives. It etches aluminum oxide at a rate of approximately 6-10 nm/min, and the purpose here is to remove the aluminum oxide cap of the permalloy.
8. Use a squirt bottle to thoroughly clean the samples with isopropanol.

Following the etch mask removal, quickly move the samples to the AJA sputter system. I then use the *in situ* argon backsputtering to sputter the sample for 5 min. I have some preliminary results showing that the TMAH dip step is not necessary provided that the backsputtering time is increased to 10-15 min. I definitely recommend experimenting with this, since the TMAH step will sometimes leave a unknown black residue on the contact regions. For the contact pads, I use 5 nm Ti followed by 75 nm Pt.

Once the metal is deposited, I lift-off the samples overnight in acetone. The lift-off often has trouble, so I always sonicate the samples for 20 s before rinsing them with isopropanol and drying.

BIBLIOGRAPHY

[1] Boehm, H. P., Clauss, A., Fischer, G. & Hofmann, U. Surface properties of extremely thin graphite lamellae. In *Proceedings of the Fifth Conference on Carbon*, vol. 1, 73–80 (Pergamon Press New York, 1962).

[2] Frindt, R. F. Single crystals of MoS_2 several molecular layers thick. *Journal of Applied Physics* **37**, 1928 (1966).

[3] Helveg, S. *et al.* Atomic-scale structure of single-layer MoS_2 nanoclusters. *Phys. Rev. Lett.* **84**, 951 (2000).

[4] Novoselov, K. S. *et al.* Electric field effect in atomically thin carbon films. *Science* **306**, 666 (2004).

[5] Novoselov, K. S. *et al.* Two-dimensional atomic crystals. *Proceedings of the National Academy of Sciences of the United States of America* **102**, 10451 (2005).

[6] Ashton, M., Paul, J., Sinnott, S. B. & Hennig, R. G. Topology-scaling identification of layered solids and stable exfoliated 2D materials. Preprint at arXiv:1610.07673 [cond–mat.mtrl–sci] (2016).

[7] Mounet, N. *et al.* Novel two-dimensional materials from high-throughput computational exfoliation of experimentally known compounds. Preprint at arXiv:1611.05234 [cond–mat.mtrl–sci] (2016).

[8] Wilson, J. A. & Yoffe, A. D. The transition metal dichalcogenides discussion and interpretation of the observed optical, electrical and structural properties. *Advances in Physics* **18**, 193 (1969).

[9] Chhowalla, M. *et al.* The chemistry of two-dimensional layered transition metal dichalcogenide nanosheets. *Nat. Chem.* **5**, 263 (2013).

[10] Deng, K. *et al.* Experimental observation of topological Fermi arcs in type-II Weyl semimetal $MoTe_2$. *Nat. Phys.* **12**, 1105 (2016).

[11] Huang, L. *et al.* Spectroscopic evidence for a type II Weyl semimetallic state in $MoTe_2$. *Nat. Mater.* **15**, 1155 (2016).

[12] Wu, Y. *et al.* Observation of Fermi arcs in the type-II Weyl semimetal candidate WTe_2. *Phys. Rev. B* **94**, 121113 (2016).

[13] Soluyanov, A. A. *et al.* Type-II Weyl semimetals. *Nature* **527**, 495 (2015).

[14] Mak, K. F., Lee, C., Hone, J., Shan, J. & Heinz, T. F. Atomically thin MoS_2 a new direct-gap semiconductor. *Phys. Rev. Lett.* **105**, 136805 (2010).

[15] Splendiani, A. *et al.* Emerging photoluminescence in monolayer MoS_2. *Nano Letters* **10**, 1271 (2010).

[16] Ishioka, J. *et al.* Chiral charge-density waves. *Phys. Rev. Lett.* **105**, 176401 (2010).

[17] Rasch, J. C. E., Stemmler, T., Müller, B., Dudy, L. & Manzke, R. 1*T*-$TiSe_2$: Semimetal or semiconductor? *Phys. Rev. Lett.* **101**, 237602 (2008).

[18] Aminalragia-Giamini, S. *et al.* Molecular beam epitaxy of thin $HfTe_2$ semimetal films. *2D Materials* **4**, 015001 (2016).

[19] Thompson, A. H. & Silbernagel, B. G. Correlated magnetic and transport properties in the charge-density-wave states of VSe_2. *Phys. Rev. B* **19**, 3420 (1979).

[20] Wilson, J. A., Di Salvo, F. J. & Mahajan, S. Charge-density waves in metallic, layered, transition-metal dichalcogenides. *Phys. Rev. Lett.* **32**, 882 (1974).

[21] Sipos, B. *et al.* From Mott state to superconductivity in 1T-TaS_2. *Nat. Mater.* **7**, 960 (2008).

[22] Rossnagel, K. On the origin of charge-density waves in select layered transition-metal dichalcogenides. *Journal of Physics: Condensed Matter* **23**, 213001 (2011).

[23] Hughes, H. P. & Friend, R. H. Electrical resistivity anomaly in β-$MoTe_2$ (metallic behaviour). *Journal of Physics C: Solid State Physics* **11**, L103 (1978).

[24] Toriyama, T. *et al.* Switching of conducting planes by partial dimer formation in $IrTe_2$. *Journal of the Physical Society of Japan* **83**, 033701 (2014).

[25] Pascut, G. L. *et al.* Dimerization-induced cross-layer quasi-two-dimensionality in metallic $IrTe_2$. *Phys. Rev. Lett.* **112**, 086402 (2014).

[26] Springer Materials. http:/materials.springer.com/. Accessed: 2016-10-06.

[27] Xiao, D., Liu, G.-B., Feng, W., Xu, X. & Yao, W. Coupled spin and valley physics in monolayers of MoS_2 and other Group-VI dichalcogenides. *Phys. Rev. Lett.* **108**, 196802 (2012).

[28] Hunt, B. *et al.* Massive Dirac fermions and Hofstadter butterfly in a van der Waals heterostructure. *Science* **340**, 1427 (2013).

[29] Ugeda, M. M. *et al.* Giant bandgap renormalization and excitonic effects in a monolayer transition metal dichalcogenide semiconductor. *Nat. Mater.* **13**, 1091 (2014).

[30] Kormányos, A., Zólyomi, V., Drummond, N. D. & Burkard, G. Spin-orbit coupling, quantum dots, and qubits in monolayer transition metal dichalcogenides. *Phys. Rev. X* **4**, 011034 (2014).

[31] Liu, G.-B., Shan, W.-Y., Yao, Y., Yao, W. & Xiao, D. Three-band tight-binding model for monolayers of group-VIB transition metal dichalcogenides. *Phys. Rev. B* **88**, 085433 (2013).

[32] Kośmider, K., González, J. W. & Fernández-Rossier, J. Large spin splitting in the conduction band of transition metal dichalcogenide monolayers. *Phys. Rev. B* **88**, 245436 (2013).

[33] Zhu, Z. Y., Cheng, Y. C. & Schwingenschlögl, U. Giant spin-orbit-induced spin splitting in two-dimensional transition-metal dichalcogenide semiconductors. *Phys. Rev. B* **84**, 153402 (2011).

[34] Yao, W., Xiao, D. & Niu, Q. Valley-dependent optoelectronics from inversion symmetry breaking. *Phys. Rev. B* **77**, 235406 (2008).

[35] Cao, T. *et al.* Valley-selective circular dichroism of monolayer molybdenum disulphide. *Nat. Commun.* **3**, 887 (2012).

[36] Knox, R. S. *Theory of Excitons* (Academic Press, New York, 1963).

[37] Ross, J. S. *et al.* Electrical control of neutral and charged excitons in a monolayer semiconductor. *Nat. Commun.* **4**, 1474 (2013).

[38] Wannier, G. H. The structure of electronic excitation levels in insulating crystals. *Phys. Rev.* **52**, 191 (1937).

[39] Elliott, R. J. Intensity of optical absorption by excitons. *Phys. Rev.* **108**, 1384 (1957).

[40] Berkelbach, T. C., Hybertsen, M. S. & Reichman, D. R. Theory of neutral and charged excitons in monolayer transition metal dichalcogenides. *Phys. Rev. B* **88**, 045318 (2013).

[41] Cudazzo, P., Tokatly, I. V. & Rubio, A. Dielectric screening in two-dimensional insulators: Implications for excitonic and impurity states in graphane. *Phys. Rev. B* **84**, 085406 (2011).

[42] Chernikov, A. *et al.* Exciton binding energy and nonhydrogenic rydberg series in monolayer WS_2. *Phys. Rev. Lett.* **113**, 076802 (2014).

[43] Scharf, B. *et al.* Probing many-body interactions in monolayer transition-metal dichalcogenides. Preprint at arXiv:1606.07101 [cond–mat.mtrl–sci] (2016).

[44] Efimkin, D. K. & MacDonald, A. H. Many-body theory of trion absorption features in two-dimensional semiconductors. Preprint at arXiv:1609.06329 [cond–mat.mes–hall] (2016).

[45] Kimura, S. & Wilson, T. Confocal scanning optical microscope using single-mode fiber for signal detection. *Applied Optics* **30**, 2143 (1991).

[46] Högele, A. *et al.* Fiber-based confocal microscope for cryogenic spectroscopy. *Rev. Sci. Instrum.* **79**, 023709 (2008).

[47] Sladkov, M. *et al.* Polarization-preserving confocal microscope for optical experiments in a dilution refrigerator with high magnetic field. *Rev. Sci. Instrum.* **82**, 043105 (2011).

[48] Meyer, C., Sqalli, O., Lorenz, H. & Karrai, K. Slip-stick step-scanner for scanning probe microscopy. *Rev. Sci. Instrum.* **76**, 63706 (2005).

[49] Malyavkin, A. V. Bound multiple exciton complex in CdTe. *Solid State Commun.* **39**, 1315 (1981).

[50] Molva, E. & Dang, L. S. Magneto-optical studies of excitons bound to Ag and Cu acceptors in *p*-type CdTe. *Phys. Rev. B* **27**, 6222 (1983).

[51] MacNeill, D. *et al.* Breaking of valley degeneracy by magnetic field in monolayer $MoSe_2$. *Phys. Rev. Lett.* **114**, 037401 (2015).

[52] Mak, K. F., He, K., Shan, J. & Heinz, T. F. Control of valley polarization in monolayer MoS_2 by optical helicity. *Nat. Nano.* **7**, 494 (2012).

[53] Jones, A. M. *et al.* Optical generation of excitonic valley coherence in monolayer WSe_2. *Nat. Nano.* **8**, 634–638 (2013).

[54] Kioseoglou, G. *et al.* Valley polarization and intervalley scattering in monolayer MoS_2. *Appl. Phys. Lett.* **101**, 221907 (2012).

[55] Zeng, H., Dai, J., Yao, W., Xiao, D. & Cui, X. Valley polarization in MoS_2 monolayers by optical pumping. *Nat. Nano.* **7**, 490 (2012).

[56] Sallen, G. *et al.* Robust optical emission polarization in MoS_2 monolayers through selective valley excitation. *Phys. Rev. B* **86**, 081301 (2012).

[57] Mak, K. F., McGill, K. L., Park, J. & McEuen, P. L. The valley Hall effect in MoS_2 transistors. *Science* **344**, 1489 (2014).

[58] Zhang, Y. *et al.* Direct observation of the transition from indirect to direct bandgap in atomically thin epitaxial $MoSe_2$. *Nat. Nano.* **9**, 111 (2013).

[59] Xiao, D., Yao, W. & Niu, Q. Valley-contrasting physics in graphene: Magnetic moment and topological transport. *Phys. Rev. Lett.* **99**, 236809 (2007).

[60] Li, X., Zhang, F. & Niu, Q. Unconventional quantum Hall effect and tunable spin Hall effect in Dirac materials: Application to an isolated MoS_2 trilayer. *Phys. Rev. Lett.* **110**, 066803 (2013).

[61] Chu, R.-L. *et al.* Valley-splitting and valley-dependent inter-landau-level optical transitions in monolayer MoS_2 quantum Hall systems. *Phys. Rev. B* **90**, 045427 (2014).

[62] Rostami, H., Moghaddam, A. G. & Asgari, R. Effective lattice hamiltonian for monolayer MoS_2: Tailoring electronic structure with perpendicular electric and magnetic fields. *Phys. Rev. B* **88**, 085440 (2013).

[63] Ho, Y.-H., Wang, Y.-H. & Chen, H.-Y. Magnetoelectronic and optical properties of a MoS_2 monolayer. *Phys. Rev. B* **89**, 155316 (2014).

[64] Cai, T. *et al.* Magnetic control of the valley degree of freedom of massive Dirac fermions with application to transition metal dichalcogenides. *Phys. Rev. B* **88**, 115140 (2013).

[65] Chang, M.-C. & Niu, Q. Berry curvature, orbital moment, and effective quantum theory of electrons in electromagnetic fields. *J. Phys.: Condens. Matter* **20**, 193202 (2008).

[66] Srivastava, A. *et al.* Valley Zeeman effect in elementary optical excitations of monolayer wse_2. *Nat. Phys.* **11**, 141 (2015).

[67] Aivazian, G. *et al.* Magnetic control of valley pseudospin in monolayer WSe_2. *Nat Phys* **11**, 148 (2015).

[68] Yafet, Y. *g* factors and spin-lattice relaxation of conduction electrons. *Solid State Physics* **14**, 1 (1963).

[69] Mitioglu, A. A. *et al.* Optical manipulation of the exciton charge state in single-layer tungsten disulfide. *Phys. Rev. B* **88**, 245403 (2013).

[70] Zhang, C., Wang, H., Chan, W., Manolatou, C. & Rana, F. Absorption of light by excitons and trions in monolayers of metal dichalcogenide MoS_2: Experiments and theory. *Phys. Rev. B* **89**, 205436 (2014).

[71] Wang, G. *et al.* Valley dynamics probed through charged and neutral exciton emission in monolayer WSe_2. *Phys. Rev. B* **90**, 075413 (2014).

[72] Bir, G. L., Aronov, A. G. & Pikus, G. E. Spin relaxation of electrons due to scattering by holes. *Zh. Eksp. Teor. Fiz.* **69**, 1382 (1975).

[73] Ma, J. & Li, Y.-S. Fiber raman background study and its application in setting up optical fiber raman probes. *Appl. Opt.* **35**, 2527 (1996).

[74] Yu, H., Liu, G.-B., Gong, P., Xu, X. & Yao, W. Dirac cones and Dirac saddle points of bright excitons in monolayer transition metal dichalcogenides. *Nat. Commun.* **5**, 3876 (2014).

[75] Jeukens, C. R. L. P. N. *et al.* Dynamical equilibrium between excitons and

trions in CdTe quantum wells in high magnetic fields. *Phys. Rev. B* **66**, 235318 (2002).

[76] Molva, E. & Dang, L. S. Magneto-optical study of Li and Na acceptor bound excitons in CdTe: Fine structure and cubic crystal-field effect. *Phys. Rev. B* **32**, 1156 (1985).

[77] Luttinger, J. M. Quantum theory of cyclotron resonance in semiconductors: General theory. *Phys. Rev.* **102**, 1030 (1956).

[78] Roth, L. M. *g* factor and donor spin-lattice relaxation for electrons in germanium and silicon. *Phys. Rev.* **118**, 1534 (1960).

[79] Wu, S. *et al.* Electrical tuning of valley magnetic moment through symmetry control in bilayer MoS_2. *Nat. Phys.* **9**, 149 (2013).

[80] Wang, G. *et al.* Magneto-optics in transition metal diselenide monolayers. *2D Materials* **2**, 034002 (2015).

[81] Kormányos, A. *et al.* $\mathbf{k} \cdot \mathbf{p}$ theory for two-dimensional transition metal dichalcogenide semiconductors. *2D Materials* **2**, 022001 (2015).

[82] Wang, Z., Shan, J. & Mak, K. F. Valley- and spin-polarized Landau levels in monolayer WSe_2. *Nat. Nano.* **AOP** (2016).

[83] Stier, A. V., McCreary, K. M., Jonker, B. T., Kono, J. & Crooker, S. A. Exciton diamagnetic shifts and valley Zeeman effects in monolayer WS_2 and MoS_2 to 65 tesla. *Nat. Commun.* **7**, 10643 (2016).

[84] Rybkovskiy, D. V., Gerber, I. C. & Durnev, M. V. Atomically inspired $k \cdot p$ approach and valley Zeeman effect in transition metal dichalcogenide monolayers. Preprint at arXiv:1610.02695 [cond–mat.mes–hall] (2016).

[85] Gippius, N. A. *et al.* Excitons in near-surface quantum wells in magnetic fields: Experiment and theory. *J. Appl. Phys.* **83**, 5410 (1998).

[86] Berghäuser, G. & Malic, E. Analytical approach to excitonic properties of MoS_2. *Phys. Rev. B* **89**, 125309 (2014).

[87] Sugawara, M., Okazaki, N., Fujii, T. & Yamazaki, S. Diamagnetic shift and oscillator strength of two-dimensional excitons under a magnetic field in $In_{0.53}Ga_{0.47}As/InP$ quantum wells. *Phys. Rev. B* **48**, 8848 (1993).

[88] Hou, H. Q. *et al.* Diamagnetic shift in $In_xGa_{1-x}As/GaAs$ strained quantum wells. *Phys. Rev. B* **43**, 4152 (1991).

[89] Rogers, D. C., Singleton, J., Nicholas, R. J., Foxon, C. T. & Woodbridge, K. Magneto-optics in GaAs-$Ga_{1-x}Al_xAs$ quantum wells. *Phys. Rev. B* **34**, 4002 (1986).

[90] MacNeill, D. *et al.* Control of spin-orbit torques through crystal symmetry in WTe_2/ferromagnet bilayers. *Nat. Phys.* **AOP** (2016).

[91] Brataas, A., Kent, A. D. & Ohno, H. Current-induced torques in magnetic materials. *Nat. Mater.* **11**, 372 (2012).

[92] Zhang, C., Fukami, S., Sato, H., Matsukura, F. & Ohno, H. Spin-orbit torque induced magnetization switching in nano-scale Ta/CoFeB/MgO. *Applied Physics Letters* **107**, 012401 (2015).

[93] Ando, K. *et al.* Electric manipulation of spin relaxation using the spin Hall effect. *Phys. Rev. Lett.* **101**, 036601 (2008).

[94] Pi, U. H. *et al.* Tilting of the spin orientation induced by Rashba effect in ferromagnetic metal layer. *Applied Physics Letters* **97**, 162507 (2010).

[95] Mihai Miron, I. *et al.* Current-driven spin torque induced by the Rashba effect in a ferromagnetic metal layer. *Nat. Mater.* **9**, 230 (2010).

[96] Liu, L., Moriyama, T., Ralph, D. C. & Buhrman, R. A. Spin-torque ferromagnetic resonance induced by the spin Hall effect. *Phys. Rev. Lett.* **106**, 036601 (2011).

[97] Miron, I. M. *et al.* Perpendicular switching of a single ferromagnetic layer induced by in-plane current injection. *Nature* **476**, 189 (2011).

[98] Liu, L. *et al.* Spin-torque switching with the giant spin Hall effect of tantalum. *Science* **336**, 555 (2012).

[99] Pai, C.-F. *et al.* Spin transfer torque devices utilizing the giant spin Hall effect of tungsten. *Applied Physics Letters* **101**, 122404 (2012).

[100] Kim, J. *et al.* Layer thickness dependence of the current-induced effective field vector in Ta|CoFeB|MgO. *Nat. Mater.* **12**, 240 (2013).

[101] Haazen, P. P. J. *et al.* Domain wall depinning governed by the spin Hall effect. *Nat. Mater.* **12**, 299–303 (2013).

[102] Emori, S., Bauer, U., Ahn, S.-M., Martinez, E. & Beach, G. S. D. Current-driven dynamics of chiral ferromagnetic domain walls. *Nat. Mater.* **12**, 611 (2013).

[103] Ryu, K.-S., Thomas, L., Yang, S.-H. & Parkin, S. Chiral spin torque at magnetic domain walls. *Nat. Nano.* **8**, 527 (2013).

[104] Mellnik, A. R. *et al.* Spin-transfer torque generated by a topological insulator. *Nature* **511**, 449–451 (2014).

[105] Fan, Y. *et al.* Magnetization switching through giant spin–orbit torque in a magnetically doped topological insulator heterostructure. *Nat. Mater.* **13**, 699 (2014).

[106] Garello, K. *et al.* Symmetry and magnitude of spin-orbit torques in ferromagnetic heterostructures. *Nat. Nano.* **8**, 587 (2013).

[107] Slonczewski, J. C. Current-driven excitation of magnetic multilayers. *Journal of Magnetism and Magnetic Materials* **159**, L1 (1996).

[108] Sun, J. Z. Spin-current interaction with a monodomain magnetic body: A model study. *Phys. Rev. B* **62**, 570 (2000).

[109] Chernyshov, A. *et al.* Evidence for reversible control of magnetization in a ferromagnetic material by means of spin-orbit magnetic field. *Nat. Phys.* **5**, 656 (2009).

[110] Endo, M., Matsukura, F. & Ohno, H. Current induced effective magnetic field and magnetization reversal in uniaxial anisotropy (Ga,Mn)As. *Applied Physics Letters* **97**, 222501 (2010).

[111] D., F. *et al.* Spin-orbit-driven ferromagnetic resonance. *Nat. Nano.* **6**, 413 (2011).

[112] Kurebayashi, H. *et al.* An antidamping spin-orbit torque originating from the Berry curvature. *Nat. Nano.* **9**, 211 (2014).

[113] Wadley, P. *et al.* Electrical switching of an antiferromagnet. *Science* **351**, 587 (2016).

[114] Skinner, T. D. *et al.* Complementary spin-Hall and inverse spin-galvanic effect torques in a ferromagnet/semiconductor bilayer. *Nat. Commun.* **6**, 6730 (2015).

[115] Ali, M. N. *et al.* Large, non-saturating magnetoresistance in WTe_2. *Nature* **514**, 205 (2014).

[116] Jiang, J. *et al.* Signature of strong spin-orbital coupling in the large non-saturating magnetoresistance material WTe_2. *Phys. Rev. Lett.* **115**, 166601 (2015).

[117] Zhu, Z. *et al.* Quantum oscillations, thermoelectric coefficients, and the Fermi surface of semimetallic WTe_2. *Phys. Rev. Lett.* **114**, 176601 (2015).

[118] Wang, L. *et al.* Tuning magnetotransport in a compensated semimetal at the atomic scale. *Nat. Commun.* **6**, 8892 (2015).

[119] Wang, Q. H., Kalantar-Zadeh, K., Kis, A., Coleman, J. N. & Strano, M. S. Electronics and optoelectronics of two-dimensional transition metal dichalcogenides. *Nat. Nano.* **7**, 699 (2012).

[120] Zhang, W. *et al.* Research update: Spin transfer torques in permalloy on monolayer MoS_2. *APL Mater.* **4**, 032302 (2016).

[121] Cheng, C. *et al.* Spin to charge conversion in MoS_2 monolayers with spin pumping. Preprint at arXiv:1510.03451 [cond–mat.mes–hall] (2015).

[122] Brown, B. E. The crystal structures of WTe_2 and high-temperature $MoTe_2$. *Acta Crystallographica* **20**, 268 (1966).

[123] Kong, W.-D. *et al.* Raman scattering investigation of large positive magnetoresistance material WTe_2. *Applied Physics Letters* **106**, 081906 (2015).

[124] Yu, G. *et al.* Switching of perpendicular magnetization by spin-orbit torques in the absence of external magnetic fields. *Nat. Nano.* **9**, 548 (2014).

[125] Taniguchi, T., Grollier, J. & Stiles, M. D. Spin-transfer torques generated by the anomalous Hall effect and anisotropic magnetoresistance. *Phys. Rev. Applied* **3**, 044001 (2015).

[126] Lee, O. J. *et al.* Central role of domain wall depinning for perpendicular

magnetization switching driven by spin torque from the spin Hall effect. *Phys. Rev. B* **89**, 024418 (2014).

[127] Yu, G. *et al.* Magnetization switching through spin-Hall-effect-induced chiral domain wall propagation. *Phys. Rev. B* **89**, 104421 (2014).

[128] Garello, K. *et al.* Ultrafast magnetization switching by spin-orbit torques. *Applied Physics Letters* **105**, 212402 (2014).

[129] Mikuszeit, N. *et al.* Spin-orbit torque driven chiral magnetization reversal in ultrathin nanostructures. *Phys. Rev. B* **92**, 144424 (2015).

[130] Rojas-Sánchez, J.-C. *et al.* Perpendicular magnetization reversal in $Pt/[Co/Ni]_3/Al$ multilayers via the spin Hall effect of Pt. *Applied Physics Letters* **108**, 082406 (2016).

[131] Liu, L., Lee, O. J., Gudmundsen, T. J., Ralph, D. C. & Buhrman, R. A. Current-induced switching of perpendicularly magnetized magnetic layers using spin torque from the spin Hall effect. *Phys. Rev. Lett.* **109**, 096602 (2012).

[132] Lee, K.-S., Lee, S.-W., Min, B.-C. & Lee, K.-J. Threshold current for switching of a perpendicular magnetic layer induced by spin Hall effect. *Applied Physics Letters* **102**, 112410 (2013).

[133] Seemann, M., Ködderitzsch, D., Wimmer, S. & Ebert, H. Symmetry-imposed shape of linear response tensors. *Phys. Rev. B* **92**, 155138 (2015).

[134] Ciccarelli, C. *et al.* Room-temperature spin-orbit torque in NiMnSb. *Nat. Phys.* **12**, 855 (2016).

[135] Li, J. & Haney, P. M. Interfacial magnetic anisotropy from a 3-dimensional Rashba substrate. *Applied Physics Letters* **109**, 032405 (2016).

[136] Amin, V. P. & Stiles, M. D. Spin transport at interfaces with spin-orbit coupling: Formalism. *Phys. Rev. B* **94**, 104419 (2016).

[137] Amin, V. P. & Stiles, M. D. Spin transport at interfaces with spin-orbit coupling: Phenomenology. *Phys. Rev. B* **94**, 104420 (2016).

[138] Avci, C. O. *et al.* Interplay of spin-orbit torque and thermoelectric effects in ferromagnet/normal-metal bilayers. *Phys. Rev. B* **90**, 224427 (2014).

[139] Blake, P. *et al.* Making graphene visible. *Applied Physics Letters* **91**, 063124 (2007).

[140] Pizzocchero, F. *et al.* The hot pick-up technique for batch assembly of van der Waals heterostructures. *Nat. Commun.* **7**, 11894 (2016).

[141] Castellanos-Gomez, A. *et al.* Deterministic transfer of two-dimensional materials by all-dry viscoelastic stamping. *2D Materials* **1**, 011002 (2014).

[142] Zomer, P. J., Guimarães, M. H. D., Brant, J. C., Tombros, N. & van Wees, B. J. Fast pick up technique for high quality heterostructures of bilayer graphene and hexagonal boron nitride. *Applied Physics Letters* **105**, 013101 (2014).

[143] Chen, C.-T., Casu, E. A., Gajek, M. & Raoux, S. Low-damage high-throughput grazing-angle sputter deposition on graphene. *Applied Physics Letters* **103**, 033109 (2013).